UNIVERSITY OF TECHNOLOGY SYDNEY
Faculty of Engineering and Information Technology

Control of Motor Drives And Gearshift for a Dual Motor-based Multi-speed Transmission

by

Haitao Yang

A Thesis Submitted
in Partial Fulfillment of the
Requirements for the Degree

Doctor of Philosophy

Sydney, Australia

2019

Certificate of Authorship/Originality

I, Haitao Yang declare that this thesis, is submitted in fulfilment of the requirements for the award of the degree of Doctor of Philosophy, in the Faculty of Engineering and Information Technology at the University of Technology Sydney. This thesis is wholly my own work unless otherwise reference or acknowledged. In addition, I certify that all information sources and literature used are indicated in the thesis.

This document has not been submitted for qualifications at any other academic institution. This research is supported by the Australian Government Research Training Program.

Production Note:

Signature: Signature removed prior to publication.

Date: 18/02/2019

Acknowledgements

I'd like to take this opportunity to express my thanks and appreciation:

to my supervisor Nong Zhang, co-supervisor Paul Walker, and external supervisor Yongchang Zhang for their help, support, sensible suggestions, and all the invaluable knowledge and experience I learned from them,

to my colleagues: Wenwei Mo, Jiejunyi Liang, Jiageng Ruan, Jinglai Wu, Yang Tian, and all other friends at the *School of Mechanical and Mechatronic Engineering* in UTS, for their valuable help, nice cooperation, stimulating conversations and funny time outside work,

to my wife, who is always by my side, for the assistance and providing a stress-free atmosphere during my doctoral studies, to my parents, for the encouragement and financial support, to my brother for the effort in taking care of the family.

At last, financial support from the University of Technology Sydney and the project ARC DP 150102751 is gratefully appreciated.

Haitao Yang

Sydney, Australia, 2019.

List of Publications

This section shows publications during the research project where Haitao Yang (*H. Yang*) is either the first author or a contributing author. The 1st-8th journal papers and the 1st-2nd conference papers listed here are strongly related to the contents of this thesis, about the control of motor drives and transmissions for the electric vehicle. These papers present the control schemes of motor drives without using the measured rotor speed or position, which can improve the reliability and safety of the drive system due to the fault-tolerant capacity brought by sensorless control strategy. The issue of performance deterioration with low pulse ratio under high-speed operation is also addressed. To improve the efficiency of the drive system, the synchronized PWM schemes are incorporated into the closed-loop current control. Moreover, shift control of the studied transmission and the active damping of torsional vibration are carefully designed to improve the driving comfort. The other papers are about the control of PWM rectifier. The PWM rectifier is used as the active front end to replace the conventional diode bridge rectifier, which guarantees lower stressing of the line supply, i.e. lower harmonics and higher power factor when converting the AC power to DC [1, 2]. However, the battery can directly supply DC voltage to the inverter in a pure electric vehicle. Hence, the work on PWM rectifier is outside the scope of this thesis and will not be included in the main chapters.

Journal Papers

1. ***H. Yang***, Y. Zhang, G. Yuan, P. D. Walker, and N. Zhang, "Hybrid synchronized PWM schemes for closed-loop current control of high-power motor drives," *IEEE Trans. Ind. Electron.*, vol. 64, no. 9, pp. 6920--6929, Sept 2017.

   H. Yang proposes the main ideal and implements the control algorithm in simulation and hardware tests. *H. Yang* writes the paper as the main author with the support of other authors who help to develop test rig and improve the quality of the paper.

2. ***H. Yang***, Y. Zhang, P. D. Walker, N. Zhang, and B. Xia, "A method to start rotating induction motor based on speed sensorless model-predictive control," *IEEE Trans. Energy Convers.*, vol. 32, no. 1, pp. 359--368, March 2017.

   H. Yang does the main part of the work. *H. Yang* carries out theoretical analysis and proposes a new feedback gain matrix for the adaptive full-order observer aiming at starting a free-running induction motor without a speed sensor. *H. Yang* writes the paper as the main author, and the other authors help to develop test rig, perform the experimental test, and improve the writing quality of the paper.

3. ***H. Yang***, Y. Zhang, P. D. Walker, J. Liang, N. Zhang, and B. Xia, "Speed sensorless model predictive current control with ability to start a free running induction motor," *IET Electr. Power Appl.*, vol. 11, no. 5, pp. 893--901, 2017.

   H. Yang comes up with the key part of this work and writes the paper as the main author. Theoretical analysis and algorithm implementation are done by *H. Yang*. The other authors help to carry out experimental tests and proofread the manuscript.

4. ***H. Yang***, Y. Zhang, J. Liang, B. Xia, P. D. Walker, and N. Zhang, "Deadbeat control based on a multipurpose disturbance observer for permanent magnet synchronous motors," *IET Electr. Power Appl.*, vol. 12, no. 5, pp. 708--716, 2018.

   H. Yang completes the main work of this research. *H. Yang* proposes a multipurpose sliding-mode disturbance observer which can either used for rotor position estimation or for improving the robustness of deadbeat predictive control based on the support and discussions with the other authors. B. Xia helps to make the experimental test and Y. Zhang is responsible for the submission and correspondence.

5. ***H. Yang***, J. Liang, P. D. Walker, J. Ruan and N. Zhang, "Gearshift Control and Active Damping of Torsional Vibrations for a Dual Motor-Based Multi-Speed Transmission," *Mechatronics*, MECH-D-18-00517, under review.

   H. Yang completes the main part of the work. *H. Yang* proposes a discrete-time sliding-mode torque observer, based on which, the smooth and fast gearshift is achieved. Additionally, a simple but very effective active damping scheme is developed to suppress torsional vibrations during and after shifting process. P. D. Walker proofreads the manuscript and holds responsible for the correspondence of this paper. J. Liang helps to develop the simulation model and check the correctness of the equations. The other authors offer the suggestions on the control system design.

6. Y. Zhang, Y. Bai, and ***H. Yang****, "A universal multiple-vector-based model predictive control of induction motor drives," *IEEE Trans. Power Electron.*, vol. 33, no. 8, pp. 6957--6969, Aug 2018.

   H. Yang is responsible for revision, submission and correspondence of this paper. *H. Yang* contributes with the theoretical proof to justify the effectiveness of the main ideal presented in this paper. Y. Zhang comes up with the key ideal, develops the test rig and proofreads the manuscript. Y. Bai carries out experimental tests and write the first draft.

7. Y. Zhang, Y. Bai, ***H. Yang****, and B. Zhang, "Low switching frequency model predictive control of three-level inverter-fed IM drives with speed sensorless and field-weakening operation," *IEEE Transactions on Industrial Electronics*, pp. 1--1, 2018.

   H. Yang is responsible for revision, submission and correspondence of this paper, and *H. Yang* contributes with the field-weakening strategy. Y. Zhang and Y. Bai develop the test rig, carry out experimental tests and write the first draft. B. Zhang offers some help in the experimental test.

8. J. Liang, ***H. Yang***, J. Wu, N. Zhang, and P. D. Walker, "Power-on shifting in dual input clutchless power-shifting transmission for electric vehicles," *Mech. Mach. Theory*, vol. 121, pp. 487 -- 501, 2018.

   The main part of the work is done by J. Liang, and the other authors help him in different areas. *H. Yang* helps to develop the simulation model and provide some suggestions on the shifting algorithm.

9. J. Liang, ***H. Yang***, J. Wu, N. Zhang, and P. D. Walker, "Shifting and power sharing control of a novel dual input clutchless transmission for electric vehicles," *Mech. Syst. Sig. Process.*, vol. 104, pp. 725 -- 743, 2018.

   J. Liang does the main part of the work. J. Wu provides an example of the code for power-sharing scheme. *H. Yang* helps to set up the simulation model for the dual input clutchless transmission and proofread the whole manuscript.

10. ***H. Yang***, Y. Zhang, J. Liang, J. Gao, P. D. Walker, and N. Zhang, "Sliding-mode observer based voltage-sensorless model predictive power control of PWM rectifier under unbalanced grid conditions," *IEEE Trans. Ind. Electron.*, vol. 65, no. 7, pp. 5550--5560, July 2018.

    H. Yang proposes the main ideal of the work and writes the paper as the main author. *H. Yang* does theoretical analysis and implements the control algorithm in the simulation test. Y. Zhang is responsible for the correspondence of the paper and does experiments with the help from J. Gao.

11. ***H. Yang***, Y. Zhang, J. Liang, J. Liu, N. Zhang and P. D. Walker, "Robust Deadbeat Predictive Power Control With a Discrete-Time Disturbance Observer for PWM Rectifiers Under Unbalanced Grid Conditions," *IEEE Trans. Power Electron.*, vol. 34, no. 1, pp. 287--300, Jan 2019.

    H. Yang proposes a discrete-time disturbance observer for improving the robustness of deadbeat predictive power control. *H. Yang* performs theoretical analysis and algorithm implementation. Y. Zhang is responsible for the correspondence of the paper and carries out experiment tests with J. Liu.

Conference Papers

1. ***H. Yang***, Y. Zhang, J. Liang, N. Zhang, and P. Walker, "Robust digital current control based on adaptive disturbance estimation for PMSM drives with low pulse ratio" in *2018 21st International Conference on Electrical Machines and Systems (ICEMS)*, Oct 2018, pp. 1252–1257.

   H. Yang proposes a digital current controller based on sliding-mode disturbance observer with low pulse ratio. *H. Yang* performs theoretical analysis and algorithm implementation. *H. Yang* writes the paper and presents it at the conference in South Korean. The other authors offer some useful suggestions and help in making experimental tests.

2. ***H. Yang***, Y. Zhang, and N. Zhang, "Two high performance position estimation schemes based on sliding-mode observer for sensorless SPMSM drives," in *2016 IEEE 8th International Power Electronics and Motion Control Conference (IPEMC-ECCE Asia)*, May 2016, pp. 3663–3669.

   H. Yang introduces two position estimation schemes for SPMSM drives in this paper. *H. Yang* performs theoretical analysis, algorithm implementation and experimental tests. *H. Yang* writes the paper and Y. Zhang presents it at the conference in China.

3. ***H. Yang***, Y. Zhang, J. Liang, N. Zhang, and P. Walker, "A robust deadbeat predictive power control with sliding mode disturbance observer for PWM rectifiers" in *2017 IEEE Energy Conversion Congress and Exposition (ECCE)*, Oct 2017, pp. 4595–4600.

   H. Yang comes up with the key ideal and makes theoretical analysis, algorithm implementation and experimental tests. *H. Yang* writes the paper and presents it at the conference in the USA. The other authors help to develop the test rig and make the experiments.

Contents

List of Figures

List of Tables

Abbreviation

AFO	Adaptive full-order observer
AT	Automatic transmission
AMT	Automated manual transmission
BBCS	Basic bus clamping strategy
CHMPWM	Current harmonic minimum pulse width modulation
CVT	Continuous variable transmission
CCS-MPC	Continuous control set-model predictive control
DCT	Dual clutch transmission
DEKF	Dual extended Kalman filter
DSP	Digital signal processor
DTC	Direct torque control
DT-CVPI	Discrete-time complex-vector proportionality-integral
DMMT	Dual motor based multi-speed transmission
DSMTO	Discrete-time sliding mode torque observer
DPCC	Discrete-time predictive current controller
DO-PCC	Disturbance observer based-predictive current control
EKF	Extended Kalman filter
EMF	Electromotive force

EV	Electric vehicle
FCS-MPC	finite control set-model predictive control
FOC	Field oriented control
HEV	Hybrid electric vehicle
HPF	High pass filter
JEKF	Joint extended Kalman filter
KF	Kalman filter
LQG	Linear-quadratic-Gaussian
MPC	Model predictive control
MPFC	Model predictive flux control
MST	Multi-speed transmission
MTPA	Maximum torque per ampere
MT	Manual transmission
ICE	Internal combustion engine
IM	Induction motor
IPMSM	Interior permanent magnet synchronous motor
PI	Proportional-integral
PID	Proportional-integral-derivative
PMSM	Permanent magnet synchronous motor
PWM	Pulse width modulation
SHEPWM	Selective harmonic elimination pulse width modulation
SMO	Sliding-mode observer

SMTO	Sliding-mode torque observer
SPMSM	Surface-mounted permanent magnet synchronous motor
SPWM	Sinusoidal pulse width modulation
SRM	Switched reluctance motor
SVM	Space vector modulation
TCU	Transmission control unit
THD	Total harmonic distortion
WTHD	Weighted total harmonic distortion
ZOH	Zero-order hold

Nomenclature and Notation

Capital letters denote complex vectors or matrices.

The symbol ˆ is used to denote an estimated variable.

The superscript ref represents the reference.

The superscript k denotes a kth instant variable.

A	Vehicle frontal area
C_s	Viscous coefficient
C_v	Rolling resistance coefficient
d	Duty ratio
$\boldsymbol{d}_p$	Disturbance resulted from parameter mismatches
$\boldsymbol{e}_i$	Current estimation error
$\boldsymbol{e}_\psi$	Flux estimation error
f_s	Switching frequency
f_e	Fundamental frequency
f_{ratio}	Frequency ratio
J	Inertial
L_m	Mutual inductance
L_s	Stator inductance
L_r	Rotor inductance

$L_{d,q}$	dq-axis inductance
m_v	Vehicle mass
M^{ref}	Modulation index
n_p	Pole pairs
N	Pulse ratio
i_d	d-axis current
i_q	q-axis current
$\boldsymbol{i}_r$	Rotor current vector
$\boldsymbol{i}_s$	Stator current vector
k_h	Coefficient of the hysteresis loss
k_{ec}	Coefficient of the eddy current loss
k_{ex}	Coefficient of the excess loss
k_d	Controller gain
$\boldsymbol{k}_u$	Voltage compensation gain
$p_{1,2}$	Poles of the system
P_{iron}	Iron loss
$r_{1,2}$	Gear ratios
r_f	Gear ratio of the final drive
r_w	Tire radius
R_s	Staotr resistance
R_r	Rotor resistance
s	Laplace operator

T_e	Electromagnetic torque
T_L	Load torque
T_M	Motor torque
T_D	Dog clutch torque
T_{sc}	Control period
T_r	Rotor time constant
T_{pwm}	PWM period
U_{dc}	DC-link voltage
$\boldsymbol{u}_s$	Stator voltage vector
$\boldsymbol{u}_s$	Extended electromagnetic force
V_{lim}	Maximum voltage available from the inverter
ω_r	Rotor speed
ω_e	Electrical speed
z	Delay operator
$Z()$	Boundary switching function
ψ_{pm}	Permanent magnetic flux
ψ_{ext}	Extended flux
$\boldsymbol{\psi}_s$	Stator flux vector
$\boldsymbol{\psi}_r$	Rotor flux vector
$\alpha_{1,2,3}$	Reduced variables
ρ	Air density
γ	Percentage of the throttle opening

τ	Time constant
θ	Phase angle
Δ	Estimation Error
$\otimes$	Cross product of two complex variables
$\int$	Integral
sign()	Sign function

Abstact

Currently, most pure electric vehicles (EVs) in the commercial market are equipped with a single-speed transmission. However, this configuration presents some disadvantages such as compromised driveability performance and lower overall efficiency due to the limited freedom in determining optimal states for motor drives. Therefore, using multi-speed transmission (MST) in EVs is regarded as a viable scheme to improve the EV performance further. This thesis focuses on the control of a dual motor-based multi-speed transmission. More specifically, the thesis centres on the following three research topics: 1) powertrain modelling and model-based torque observer design; 2) high-performance motor control including position/speed sensorless operation, controller and observer design under low pulse ratio, and closed-loop control based on synchronized pulse width modulation; 3) gearshift control including coordinated torque and speed control of two motors, speed synchronization and active vibration damping control.

The first part of this thesis introduces the configuration of the studied MST, its advantages and the issues need to be addressed. Additionally, the detailed transmission and motor models are developed for theoretical analysis and controller design. The requirement of the motor drive in an EV involves more than the satisfactory steady-state performance but also fast dynamic response and high battery-to-motor efficiency. The control of motor drive is the fundamental based on which an EV can be driven efficiently, comfortably and safely. Therefore, the second part of this thesis work develops control schemes for the induction motor (IM) and permanent magnet synchronous motor (PMSM) which are currently the main choices for EVs. The

improved observers are designed to achieve position/speed sensorless control. The impact of discrete-time implementation is investigated to ensure stability and fast dynamic response under low pulse ratio. Simulation, experimental tests and comparative studies with the prior methods were carried out to validate the superiority of the proposed methods. Finally, a closed-loop torque control scheme along with active vibration damping is proposed to achieve high-quality gearshift. Considering the measurement of shaft torque is not feasible in practical application, a discrete-time sliding-mode torque observer is further designed to provide the feedback signal for the proposed controller.

Owing to the sophisticated structure design and advanced control schemes, not only the driving comfort but also the reliability and efficiency of the whole system can be greatly improved. The feasibility and effectiveness of the proposed methods are confirmed by simulation and/or experimental tests.

Chapter 1

Introduction

1.1 Background

The automobile brings convenient and fast transportation to the human on the one hand but causes high energy consumption of fossil fuel and air pollution on the other. Conventional internal combustion engine (ICE) vehicles have proven to be one of the major contributions to carbon emission and air pollution. For sustainable development, the shift to EVs picks up the rate during the past years. From the technological perspective, the market share of EVs gradually increases recently due to the rapid development of the battery, fast charger, powertrain, and so on. To meet the demanding market requirements, researchers and engineers have investigated various motor drives and transmission systems. Nowadays, it is generally acknowledged that EV is a feasible solution for urban mobility and have attracted much attention from both academic and industrial communities. Many vehicle manufacturers have produced pure electric vehicles and hybrid electric vehicles, e.g. Tesla Motors, BMW, Mercedes-Benz, Volvo, Audi, General Motors. It can be expected that electric vehicles would be more popular in the future. For a conventional vehicle, the powertrain is made up of engine, transmission, and drivetrain. The transmission system is used to adjust the engine's speed and torque to match the demands of different operating conditions. After the transmission, the

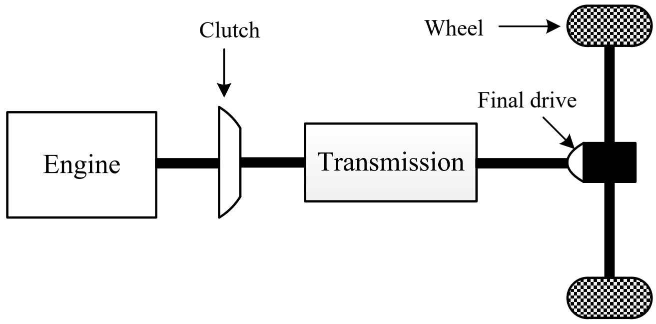

Fig. 1.1: A simple illustration of powertrain

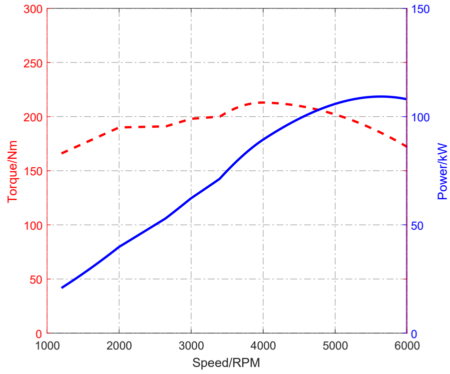

Fig. 1.2: Maximum torque and power for a typical engine over the operating range

torque and speed are transferred to wheels through the drivetrain which includes differential, driveshaft, etc.. The powertrain must be properly designed and optimized for satisfactory vehicle performance, such as less fuel consumption, driving comfort, minimal noises and cost reduction. The illustration of a typical powertrain is shown in Fig. 1.1. Nowadays, fossil fuel engines are still the main power sources for road vehicles. The typical engine characteristic is illustrated in Fig. 1.2 [7]. It is clear that the operating range of the engine is limited and thus the car cannot be driven over a wide speed range. As a result, transmission is still indispensable in the modern vehicle industry.

Unlike the engine, motor speed and torque are more controllable with satisfactory dynamic performance. By employing advanced control schemes, full torque can be provided from standstill to the rated speed. As an electric vehicle can not gain as much benefit from using multi-gear transmissions as that for a conventional vehicle, commercialized pure EVs are mainly equipped with single speed transmissions, based on the tradeoffs between total cost, complexity of the system, etc.. However, it is still suggested in the existing research to employ multi-speed transmission (MST) for better driveability and overall efficiency [8–12]. With the proper MST configuration and control schemes [9], the power interruption during gearshift can be avoided. Thereby, the long-term cost could be reduced without sacrificing driving performance [13]. In [13], battery electric vehicles equipped with three types of transmissions, namely single-speed transmission, dual clutch transmission (DCT) and continuously variable transmission are compared regarding cost and performance (efficiency, driving range and acceleration). The results show that the vehicle performance is improved and the customer's money is saved from a long-term sight when the multiple speed transmission is equipped. Conventionally, a friction clutch or torque converter is used in the MST to facilitate smooth gearshift. The main deficiency of those mechanisms is relatively low efficiency [14]. Hence, it is suggested in many studies to remove such components in an EV transmission by taking advantage of the controllability of an electric motor [12, 15, 16]. But on the other hand, the friction clutch or torque converter can isolate/attenuate torque oscillations in the driveline. If they are not implemented, system damping is significantly reduced, and thus sophisticated control schemes must be designed to avoid long-duration oscillations during and after transient processes. Aiming at obtaining better performance and solving torque interruption in the traditional configuration, a dual motor-based multi-speed transmission (DMMT) as shown in Fig. 1.3 is proposed at University of Technology Sydney. Two motors M1 and M2 are connected to primary shafts. By controlling the dog clutches D1, D2 and D3, two motors can work separately or

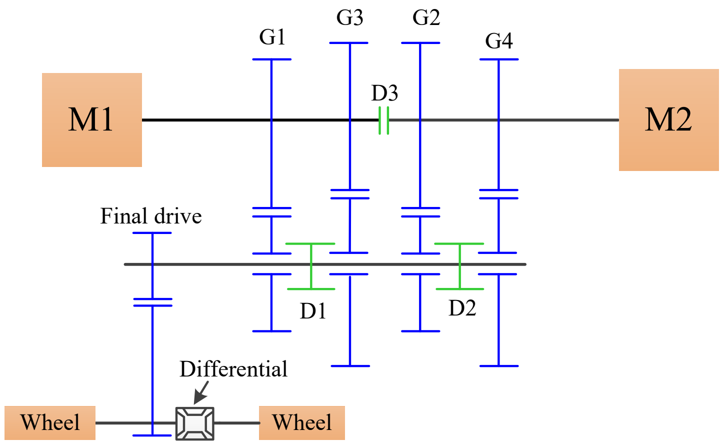

Fig. 1.3: Schematic configuration of the studied powertrain

simultaneously. Although there are only four gear pairs, 13 different working states are available, which are summarized in Table 1.1.

In the table, “0” indicates a dog clutch is disengaged while “1” means the dog clutch is engaged. The two columns “M1” and “M2” on the right side represent the gear pairs, through which the output torque of the motor M1 and M2 is transmitted to the final drive. “0” in the “M1” and “M2” means the corresponding motor is powered off without connection to the transmission. It is found from the table that the motor M1 can work in series or in parallel with the motor M2, or even work alone. In real-time operation, the state leading to the minimum power loss is selected by the power management controller to improve the overall efficiency of the powertrain. It should be mentioned that a by-product of two motors is the redundancy of the power source which can be utilized to improve the reliability. For example, the motor M1 is isolated if it breaks down and M2 can still deliver the power to the vehicle. In short, the operation mode is versatile for the DMMT, which can be utilized to optimize efficiency or drivability [17].

Table 1.1 : Possible working states of the DMMT

<table>
<tr><th>No.</th><th>D3</th><th>D2</th><th>D1</th><th>M1</th><th>M2</th></tr>
<tr><td>1</td><td rowspan="9">0</td><td rowspan="3">0</td><td>0</td><td>0</td><td>0</td></tr>
<tr><td>2</td><td>1</td><td>G1</td><td>0</td></tr>
<tr><td>3</td><td>1</td><td>G3</td><td>0</td></tr>
<tr><td>4</td><td rowspan="6">1</td><td rowspan="2">0</td><td>0</td><td>G2</td></tr>
<tr><td>5</td><td>0</td><td>G4</td></tr>
<tr><td>6</td><td rowspan="6">1</td><td>G1</td><td>G2</td></tr>
<tr><td>7</td><td>G1</td><td>G4</td></tr>
<tr><td>8</td><td>G3</td><td>G2</td></tr>
<tr><td>9</td><td>G3</td><td>G4</td></tr>
<tr><td>10</td><td rowspan="4">1</td><td rowspan="2">0</td><td>G1</td><td>G1</td></tr>
<tr><td>11</td><td>G3</td><td>G3</td></tr>
<tr><td>12</td><td rowspan="2">1</td><td rowspan="2">0</td><td>G2</td><td>G2</td></tr>
<tr><td>13</td><td>G4</td><td>G4</td></tr>
</table>

Similar architecture can be seen in [18]. However, there is no dog clutch D3, and M1 and M2 can only work in separate conditions. While in the presented DMMT, M1 and M2 can work separately with the connection to different gears or simultaneously by connection to the same gear. As dual motors need to be coordinately controlled in the DMMT, the complexity of the control system is relatively higher compared with the single motor-based transmission. Though it is expected that multi-speed transmission shown in Fig. 1.3 could bring many benefits, its design and control are much more complex. As part of the project, this thesis focus on the high-performance control of motor drives and gearshift for obtaining high efficiency, reliability and better driving comfort.

1.2 Research Objectives

The widespread use of EV technologies would contribute significantly to reducing the dependence of vehicles on fossil fuels and decreasing greenhouse gas emission. In an EV control system, the performance of the motor drive and gearshift control can be directly observed by the passenger and thus have a great impact on customer experience.

The thesis work includes two main parts: motor control and gearshift control. Motor control is fundamental in the system based on which the function of energy management, gearshift control, shaft oscillation damping control, etc. can be achieved. First, several high-performance current controllers for different motor drives are developed and verified by simulation and experimental tests. Then, the position/speed sensorless control methods are investigated for the operation under sensor fault condition, which is known as limp-home mode in EV applications to improve the safety and reliability of the whole system [19]. Finally, the gearshift control strategy along with the active vibration damping method is developed based on the validated motor control schemes. The detailed research objectives of this thesis can be summarized as follows:

- Literature review and discussion on EV transmission, shifting control strategies and motor control schemes
- Development of a detailed mathematical model for the studied DMMT and investigation of modelling induction motor (IM) and permanent magnet synchronous motor (PMSM)
- Design of observers for the IM and PMSM to estimate flux and achieve position/speed sensorless operation
- Design of discrete-time current controller for IM and PMSM under low pulse ratio to improve the dynamic response and robustness against parameter mismatches
- Development of the method to integrate synchronized pulse width modulation into the closed-loop current control
- Theoretical analysis of the shaft resonance induced by the motor torque variation and design of the active damping controller
- Design of torque observer to estimate the torque transmitted by the dog clutch with the purpose to provide the basis for the gearshift control

- Development of coordinated torque and speed control strategy for dual motors to achieve fast and smooth gearshift

1.3 Outline of Thesis

The remaining part of this thesis is organized as follows.

Chapter 2 presents a comprehensive literature survey of various vehicle transmissions, motor drives, high-performance motor control schemes and shifting strategies. The strengths and weaknesses of the existing research in the concerned areas are explained. After that, the issues that cannot be simply solved by the prior methods are briefly introduced.

Chapter 3 describes the basic principle and the dynamic model of the studied DMMT. The IM and PMSM models are also presented. This chapter provides fundamentals for theoretical analysis and development of observers and controllers in this thesis.

Chapter 4 introduces high-performance control schemes for IM drives, including the adaptive observer for speed-sensorless operation with the ability to start a free-running motor, design of a digital current controller, methods to integrate the synchronized PWM into closed-loop current control. Simulation and experimental results are illustrated to verify the effectiveness of the proposed methods.

Chapter 5 presents high-performance control schemes for PMSM drives. A sliding-mode observer is designed with inherent filtering capacity for position/speed-sensorless operation. Discrete-time current controllers are designed and compared with the existing ones. The synchronized PWM is also incorporated and tested in the closed-loop current control. Simulation, experimental tests and comparative studies were carried out to validate the superiority of the developed methods.

Chapter 6 describes the development of an extended sliding-mode torque observer (SMTO) for the estimation of the torque transmitted by the engaged dog clutch. The analytic relationship between the estimated torque and its actual value is derived to facilitate performance analysis of the developed SMTO. Comparison with the prior method and experimental tests were performed to show the advantages of the proposed SMTO.

Chapter 7 shows shifting control of DMMT. First, the shifting process and the corresponding control schemes are developed. Then, the torsional vibration is analyzed, and an active damping controller is subsequently proposed. Finally, the shifting control and active vibration damping are combined to achieve smooth and fast gearshift.

Chapter 8 reviews and summarize the work presented in the previous chapters. The potential research works that need further studies are also briefly introduced.

Chapter 2

Literature Survey

2.1 Transmission for EVs

In the design of a new EV powertrain, the performance of the transmission system is one of the major concern. Currently, most commercial EVs are equipped with a single-speed gearbox, which is a cost-effective solution while without significant performance limitation. However, much research has validated that employing multi-speed transmission could significantly improve the energy efficiency and drivability through a more flexible selection of motor operating conditions [13, 16, 18, 20]. Meanwhile, battery and motor sizes can be reduced [21].

Among different types of transmissions, the manual transmission (MT) has higher efficiency. The main drawback is that it requires driver's attention to operate clutch during each gear shift. In an automatic transmission, gearshifts are achieved automatically. The gear set is selected by a transmission control unit (TCU) to satisfy the requirement of energy efficiency and drivability. There are several automatic transmissions available in the market, such as planetary-gears-automatic transmission (AT), automated manual transmission (AMT), continuous variable transmissions(CVTs) and dual clutch transmission (DCT) [22]. AT consists of the planetary train, wet clutches and torque converter, which make it relatively expensive and less efficient [23]. AMT presents as high efficiency as MT, but there would be temporary torque interrupt during gear shifts which significantly degrades its performance [11]. Unlike the limited gear ratios that AT, MT and AMT offer, CVT is the infinitely variable transmission system, in which the gear ratio can be adjusted smoothly from zero to its highest ratio. CVT can offer a more comfortable feeling and higher fuel efficiency owing to the possibility of continuous and smooth gear ratio change. However, the major drawback of CVT is its lower torque capacity [24], and thus its application is limited. DCT can be regarded as a combination of two AMTs. Hence, DCT has two paths to deliver the power from the engine to wheels. As one of the clutches will pre-engage before the other one disengages during the gear shift, it is possible to eliminate or reduce power loss during gear shifting [13]. AT and DCT can offer better driving comfort by eliminating or reducing torque interruption. However, the hydraulic control system, friction clutches and clutch-to-clutch shift introduce additional parasitic losses [25], which can be the significant sources of inefficiencies [26].

More or less, conventional transmission system has shortcomings when directly applied to EVs. This encourages the development of some novel transmission systems to meet the demanding requirements of size, cost, efficiency, driveability, and drive comfort. For instances, some two-speed transmissions are presented in [9, 23, 27] with control schemes investigated to achieve seamless gearshift. Due to the limited gear ratios in a two-speed transmission, it is still hard to optimize the efficiency and drivability simultaneously.

With the state-of-the-art design techniques, the maximum power density of EV motors can be up to 18 kW/L [28]. Additionally, exhaust pipe and fuel supply unit, etc. are not required in a pure EV. Therefore, it is not a problem to install two electric motors in a powertrain system [16]. As shown in Fig. 1.3, a novel dual motor-based multi-speed transmission (DMMT) is investigated in the University of Technology Sydney. The DMMT combines the merits of AMT, DCT and AT without their significant negative aspects. In DMMT, two motors are employed, and one of them can increase output power temporarily when the other one is disengaged during shifting process. Hence, torque interruption can be eliminated with this novel transmission. As stated in Chapter 1, there are 13 possible states in this transmission. Hence, more freedom and flexibility are available to optimize transmission and motor operating conditions to obtain better overall performance. Additionally, as no friction components such as dry/wet clutches and synchroniser are adopted in the DMMT, high efficiency of the transmission can be expected.

2.2 Powertrain Modelling

The powertrain is a fundamental subsystem in a vehicle and modelling of vehicle powertrain is critical for evaluating the design and control performance of the whole system. The dynamic equations of powertrain can be derived in different ways depending on the research purpose. On the one hand, to capture the detailed transient behaviour in simulation, it is necessary to model the powertrain as accurately as possible. On the other hand, the model should be reasonably simplified to facilitate controller design and theoretical analysis.

In [29], four degrees of freedom and fifteen degrees of freedom models of a DCT equipped powertrain are investigated and compared for vibration analysis and shift transient simulations. It is shown that the fourth-order model can capture low order shuffle mode response, but the higher frequency of vibration responses in fifteenth-order model is not present. The similar conclusion can be found in [30], in which a simplified model is built to capture the low-frequency torsional vibration in a series-parallel hybrid propulsion system. To study the efficiency of the powertrain, the numerical models for evaluating drag torque are developed in [25]. The results show that viscous shear in the wet clutch and gear churning losses are main contributions to the whole drag torque.

For an in-depth study of the dynamics of a powertrain, a detailed model is certainly preferable, such as those in [29]. However, when coming to powertrain control, a simplified model contains information of concerned behaviour and control variables is usually enough for controller and observer design from the view of engineering application. For example, torque observer, and Kalman filter are designed based on reduced order model in [31] and [32] respectively. In [33], it is assumed that the engine, torque converter and gearbox are all rigid multibody system connected to each other by ideal rigid joints. The simulation and experimental results validate the effectiveness of the assumption in the studied example. In the shifting control of a clutchless automatic manual transmission [12], a lumped-inertia driveline model is adopted, and the results show that using a simplified model for analysis could lead to satisfactory performance. In this research, a detailed model will be developed for transient simulations, but some simplifications will be made for controller and observer design.

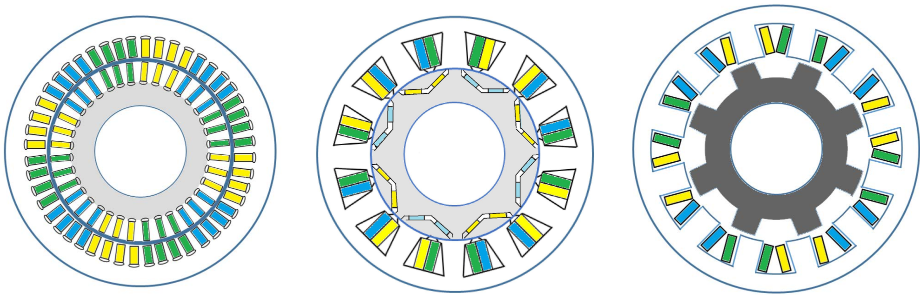

(a) (b) (c)

Fig. 2.1: Cross section views of (a) IM, (b) PMSM and (c) SRM. [3, 4]

2.3 Electric Motor for EVs

Electric motor drives play an important role in EVs, which form the core energy conversion system in the EV driveline. The requirements of an electric machine for traction applications include not only high power density and high efficiency over a wide speed and torque range but also high reliability, lower vibration, acceptable cost, etc. [3, 28, 34, 35]. To satisfy these requirements, few types of the motor have been adopted in the EV industry. More specifically, induction motor (IM), permanent-magnet synchronous motor (PMSM) and switched reluctance motor (SRM) are normally considered as potential candidates for the traction motor. The typical cross section views of IM, PMSM and SRM are illustrated in Fig. 2.1. Much research has been conducted trying to figure out which one is most appropriate for the electric-propulsion system [34, 36–39]. Generally speaking, PMSM presents higher efficiency and lower size under the condition of the same power and torque requirements, while IM is featured by lower cost and higher reliability. SRM

Table 2.1 : Traction motors applied in EVs and HEVs.

Manufacturer	Model	Traction Motor
Honda	Insight, Civic, Accord	PMSM
BMW	i3, i8	PMSM
Chevrolet	Volt & Energi	PMSM
Toyota	Camry, Prius C & V	PMSM
Ford	Fusion SE Hybrid	PMSM
Tesla	Roadster	IM
GM	EV1	IM
Ford	Focus Electric	IM
Honda	Fit EV	IM
Holden	Ecommodore	SRM

is currently emerging as an attractive alternative due to its simple and rugged motor construction, undemanding cooling, inherent fault tolerance and high efficiency [40]. However, high acoustic noise and torque ripple are the main drawbacks of such motors. Though various techniques have been proposed to address such problems [41, 42], the acoustic noise remains a challenging issue to be addressed [43]. Hence, IM and PMSM are currently the main choices for EVs in the commercial market. Table. 2.1 shows different traction motors applied in the EVs and hybrid electric vehicles (HEVs) [4]. As surface mounted PMSM has limited overload capacity [3], the PMSM discussed here refers to interior PMSM (IPMSM).

One of the major concerns of motor selection is its efficiency. It should be noted that the motor efficiency map does not only relates to the motor itself but also depends on control schemes. Equipped with a smarter inverter, both IM and PMSM can be driven in an efficient way [44, 45]. Though the peak efficiency of IM is lower than PMSM, the average efficiency during normal driving conditions could be comparable to the PMSM when the loss minimization scheme is applied [36, 46]. In IM and PMSM, the losses mainly include copper loss and iron loss. The iron loss can be expressed by Steinmetz equation [34]:

$$P_{\text{iron}} = k_h f B^2 + k_{ec} f^2 B^2 + k_{ex} f^{1.5} B^{1.5}. \tag{2.1}$$

where f and B are the operating frequency and magnitude of the magnetic flux density. k_h, k_{ec}, and k_{ex} are the coefficients of the hysteresis loss, eddy current loss, and excess loss, respectively. For IM, copper loss can be calculated as

$$P_{\text{IM}} = 3R_s i_s^2 + 3R_r i_r^2 \tag{2.2}$$

where, R_s and R_r represent stator resistance and rotor resistance. i_s and i_r are stator current and rotor current respectively. For PMSM, there is only copper loss in the stator windings, which can be expressed as

$$P_{\text{PMSM}} = 3R_s i_s^2. \tag{2.3}$$

In the rotor flux oriented synchronous reference frame, stator current can be decoupled into flux component i_d and torque component i_q [47]. By controlling i_d and i_q, flux magnitude and output torque can be indirectly controlled. For IM, the electromagnetic model can be expressed as (2.4) and (2.5).

$$\psi_r = L_m i_d \tag{2.4}$$

$$T_e = \frac{3}{2} n_p \frac{L_m}{L_r} \psi_r i_q \tag{2.5}$$

where, ψ_r is the magnitude of rotor flux and T_e is the torque. At high speed under steady-state condition, the required voltage from the inverter can be approximately expressed as [47]:

$$U_s = -\omega_e \sigma L_s i_q + j\omega_e L_s i_d \tag{2.6}$$

where ω_e is output frequency of the inverter, L_s is stator inductance, and l$\sigma = 1 - L_m^2/(L_s L_r)$ is the total leakage coefficient. As σ is designed to be small for obtaining a wider operating range [3], the required voltage at high speed is dominated by $\omega_e L_s i_d$. Due to the limited battery voltage, i_d must be gradually decreased with increasing ω_e in flux-weakening region. As a result, higher efficiency can be obtained during high speed operation with a light load. This is because both iron loss and copper loss would decrease in this case, due to reduced flux density and smaller current.

For a PMSM, the torque is given by

$$T_e = \frac{3}{2} n_p (\psi_{pm} i_q + (L_d - L_q) i_d i_q) \tag{2.7}$$

where, ψ_{pm} is permanent magnetic flux, L_d and L_q are d-axis and q-axis inductances. For better efficiency, maximum torque per ampere (MTPA) operation is usually adopted in practical application [48]. With MTPA strategy, d-axis current i_d can be expressed as (2.8) if the voltage drop in phase resistance is neglected [45].

$$i_d = \frac{\psi_{pm}}{2(L_q - L_d)} - \sqrt{\frac{\psi_{pm}^2}{4(L_q - L_d)^2} + i_q^2} \tag{2.8}$$

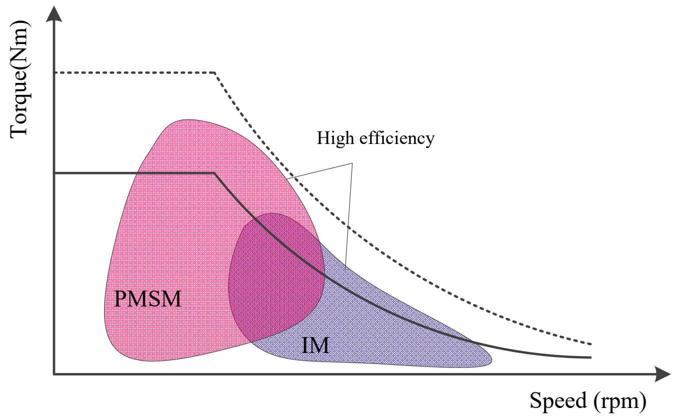

Fig. 2.2: Exemplary efficiency maps of IM and PMSM.

When entering flux weakening region, d-axis and q-axis current relationship can be expressed as [45, 49]

$$i_d = -\frac{\psi_{pm}}{L_d} + \frac{1}{L_d}\sqrt{\frac{V_{lim}^2}{\omega_e^2} - (L_q i_q)^2} \tag{2.9}$$

where V_{lim} is the maximum voltage available from the inverter. In flux weakening region with increasing speed, d-axis current for IM gradually decreases while it increases for PMSM. Hence, the efficiency of IM would be comparable with PMSM in high speed region [28]. However, IM needs d-axis current to excite flux and there is additional copper loss in the rotor. To generate the same torque, the required current for IM is generally higher than that needed for PMSM in low-speed region. As a result, the PMSM presents higher efficiency at low speed operation. An illustrative comparison of efficiency map of IM and PMSM is shown in Fig. 2.2 [50]. It can be seen that IM and PMSM present different distributions of efficiency. Hence, it is possible to use both motors in the investigated DMMT so as to take advantage of their merits at different operating points.

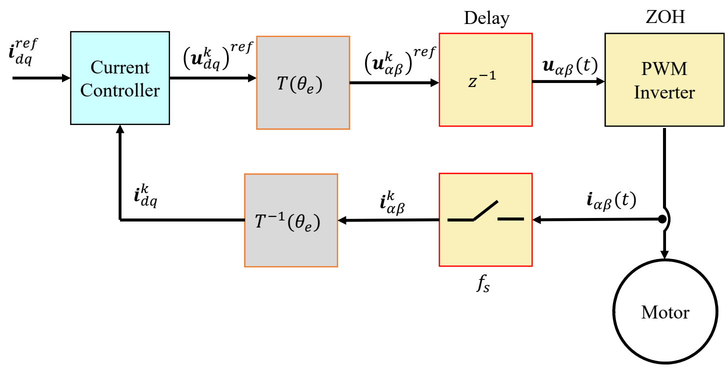

Fig. 2.3: Schematic diagram of FOC.

2.4 Control of IM and PMSM Drives

For high-performance control of IM and PMSM, two well-established control schemes are field oriented control (FOC) [47, 51], and direct torque control (DTC) [51–53]. Both methods have been commercialized. DTC can present very fast dynamic response while FOC exhibits better steady-state performance, especially during low speed operation. Recently, model predictive control (MPC) has attracted wide attention from both academic and industrial communities owing to its fast dynamic response, ability to operate at optimized points and flexibility of handling constraints [54–58]. It is shown that the performance of MPC is comparable to FOC [59, 60] and usually better than DTC [55, 61, 62] under the similar average switching frequency in medium and high speed ranges. The typical schematic diagrams of FOC, DTC and MPC are shown in Figs. 2.3, 2.4 and 2.5 respectively.

Control Methods for IM Drives

1. FOC

The basic principle of FOC is to decompose the stator current into the flux compo-

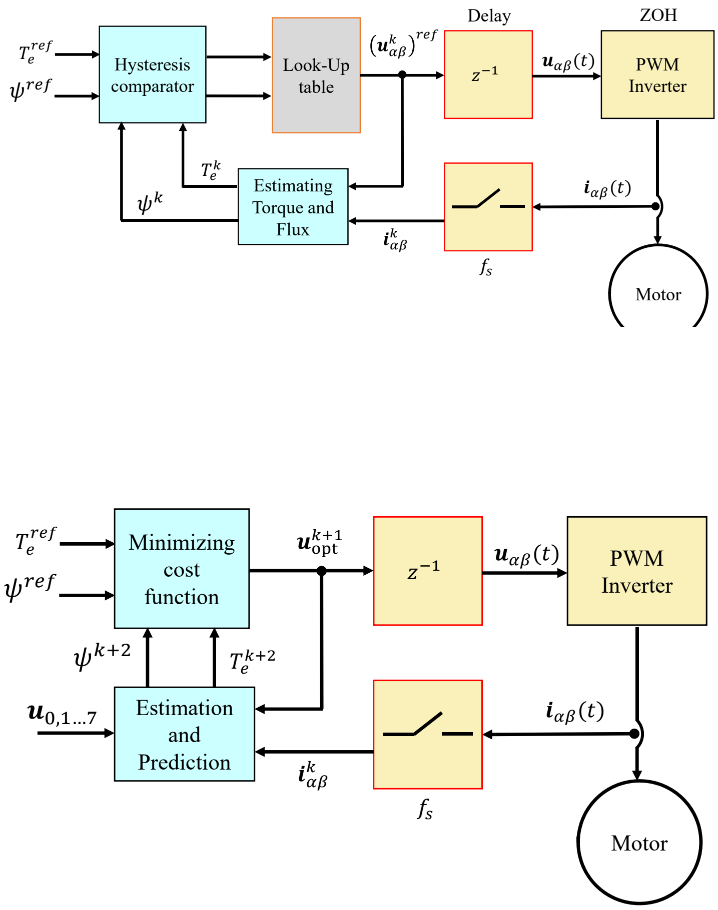

Fig. 2.5: Schematic diagram of MPC.

nent current i_d and torque component current i_q according to the position of rotor flux vector. It should be noted that the outer controllers such as speed/flux controller and field-weakening strategy are not presented here. In most applications, the proportional-integral (PI) controller is used to regulate stator current to track its reference. The reference of torque component current i_q^{ref} can be generated from the braking pedal, acceleration pedal or speed controller, with the braking pedal input overriding for the safety reason. FOC's performance heavily relies on the tuning of the current controller. For high speed and low switching frequency operation, the conventional FOC tends to be unstable and the controller must be carefully designed

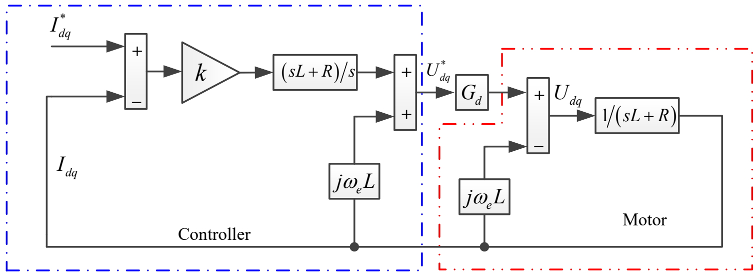

Fig. 2.6: Diagram of current control loop based on PI controller.

to achieve fast and robust current regulation [5, 63–65].

By decoupling back-electromotive force (EMF), the current control loop can be modeled as a resistor and inductor [5]. The transfer function is

$$\frac{i_s^e(s)}{u_s^e(s)} = \frac{1}{R + L \cdot s} \tag{2.10}$$

The subscript e represents the field-oriented reference frame. For a given power rating, the motor's volume is approximately inversely-proportional to its rated speed [66]. Hence, the motor used in an EV is usually designed with a high rotating speed in order to achieve higher power density. FOC is implemented in the field-oriented reference frame rotating at the speed of ω_e. Therefore, the phase error caused by frame rotation during delay period should be compensated especially at high speed. The delay effect in the field-oriented reference frame can be expressed as (2.11) [63].

$$G_d^e = \frac{e^{-1.5j\omega_e T_s}}{\frac{2}{\omega_e T_s}\sin(\frac{\omega_e T_s}{2})} e^{-1.5T_s s} \tag{2.11}$$

$$G_{PI} = \frac{k_p s + k_i}{s} \tag{2.12}$$

If the PI regulator (2.12) is employed, the closed-loop transfer function can be derived as (2.13) according to the diagram shown in Fig. 2.6.

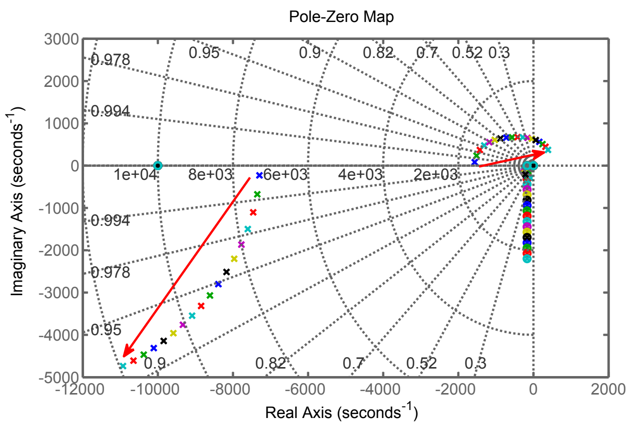

Fig. 2.7: Pole-Zero map of the closed-loop system (2.13) when the synchronous speed varies from 10-350 Hz.

$$G_{cl} = \frac{k(sL+R)G_d^e}{s(sL+R+j\omega_e(L-G_d^eL))+k(sL+R)G_d^e} \tag{2.13}$$

From the pole-zero map in Fig. 2.7, it is seen that the dominated pole will gradually shift to the right side of the complex plane when ω_e increases, indicating that the control system would become poor damped and even unstable during high-speed operation. Hence, for high-speed traction motor drives, the impact of the digital delay must be carefully considered when designing the controller. It is shown in [67] that the current controllers designed based on complex state variables present much better performance over the traditional PI controllers at high speed. However, these controllers are designed in continues-time domain, which may introduce error of discretization when they are implemented in the digital controller. In [5, 65], the complex current controller is directly designed in the discrete-time domain, showing good tracking bandwidth and stable margin, because the discrete nature of the control system is directly considered in the design stage. However, the desired performance depends on exact pole/zero cancellation. Though the parameter robustness is improved when compared with the conventional PI controller, the control performance still deteriorates if motor parameter deviates from its nominal value. In practical applications, the inductance and resistance may change due to the core saturation and temperature variation. Thus, it is essential to ensure the controller can handle parameter mismatches so that the desired performance can always be guaranteed.

Table 2.2 : Look-up table for DTC

$\triangle\psi$	$\triangle T_e$	S_1	S_2	S_3	S_4	S_5	S_6
1	1	$\boldsymbol{u}_2$	$\boldsymbol{u}_3$	$\boldsymbol{u}_4$	$\boldsymbol{u}_5$	$\boldsymbol{u}_6$	$\boldsymbol{u}_1$
	0	$\boldsymbol{u}_7$	$\boldsymbol{u}_0$	$\boldsymbol{u}_7$	$\boldsymbol{u}_0$	$\boldsymbol{u}_7$	$\boldsymbol{u}_0$
	-1	$\boldsymbol{u}_6$	$\boldsymbol{u}_1$	$\boldsymbol{u}_2$	$\boldsymbol{u}_3$	$\boldsymbol{u}_4$	$\boldsymbol{u}_5$
-1	1	$\boldsymbol{u}_3$	$\boldsymbol{u}_4$	$\boldsymbol{u}_5$	$\boldsymbol{u}_6$	$\boldsymbol{u}_1$	$\boldsymbol{u}_2$
	0	$\boldsymbol{u}_0$	$\boldsymbol{u}_7$	$\boldsymbol{u}_0$	$\boldsymbol{u}_7$	$\boldsymbol{u}_0$	$\boldsymbol{u}_7$
	-1	$\boldsymbol{u}_5$	$\boldsymbol{u}_6$	$\boldsymbol{u}_1$	$\boldsymbol{u}_2$	$\boldsymbol{u}_3$	$\boldsymbol{u}_4$

2. DTC

DTC can achieve fast dynamic response with a simpler structure when compared with FOC. The torque of IM can be expressed in terms of stator flux and rotor flux as

$$T_e = \frac{3}{2} n_p \lambda L_m \boldsymbol{\psi}_r \otimes \boldsymbol{\psi}_s = \frac{3}{2} n_p \lambda L_m \left\| \boldsymbol{\psi}_r \right\| \cdot \left\| \boldsymbol{\psi}_s \right\| \cdot \sin(\theta_{sr}), \tag{2.14}$$

where θ_{sr} is the difference between the phase angle of stator flux vector $\boldsymbol{\psi}_s$ and rotor

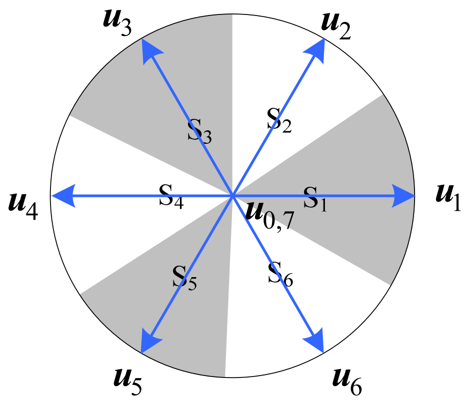

Fig. 2.8: Voltage vectors and sector division for a two-level inverter.

flux vector $\boldsymbol{\psi}_r$. In the stationary reference frame, the relationship between $\boldsymbol{\psi}_s$ and $\boldsymbol{\psi}_r$ can be expressed as

$$\frac{\boldsymbol{\psi}_r(s)}{\boldsymbol{\psi}_s(s)} = \frac{L_m/L_s}{\sigma T_r \cdot s + (1 - j\sigma T_r \omega_r)} \tag{2.15}$$

where $T_r = L_r/R_r$ is the rotor time constant. It is clear that $\boldsymbol{\psi}_r$ is the result of $\boldsymbol{\psi}_s$ passing through a complex coefficient filter. The variation of $\boldsymbol{\psi}_r$ will always lag behind $\boldsymbol{\psi}_s$. Therefore, by fast control of $\boldsymbol{\psi}_s$, the phase angle θ_{sr} could be quickly changed. In this way, torque can be regulated as can be seen from (2.14). For a two-level inverter, there are 8 different switching states and 7 different voltage vectors, dividing the complex plane into 6 sectors, as shown in Fig. 2.8. According to the stator flux position, the sign of flux error and torque error, a look-up table for controlling torque and flux can be designed as shown in Table 2.2. The error signal of $\triangle\psi$ and $\triangle T_e$ are determined by two hysteresis controllers, which are shown in Figs. 2.9 and 2.10. The traditional DTC selects only one voltage vector during each control period, which leads to relatively higher torque ripples and current harmonics. To ensure satisfactory steady-state performance, the sampling frequency has to be very

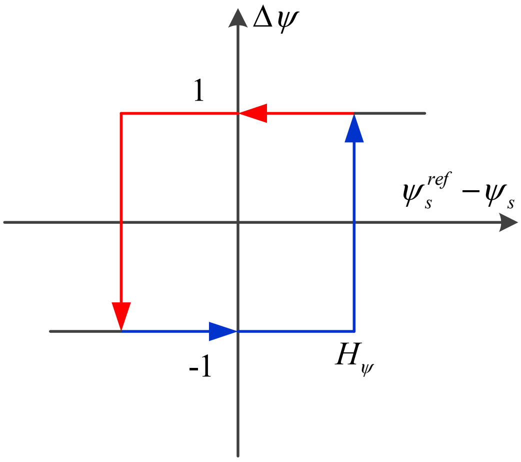

Fig. 2.9: Flux hysteresis comparator.

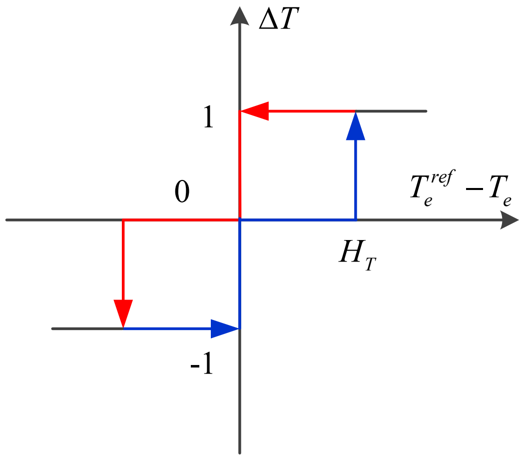

Fig. 2.10: Torque hysteresis comparator.

high, which imposes high computational burden on the digital processor. For better performance and to reduce the sampling frequency, multiple-vectors based methods have been proposed [68, 69]. In these methods, two or three vectors are selected during one control period. Since the torque can be regulated more accurately, the performance is significantly improved.

3. Model Predictive Control

Generally, MPC can be categorized into continuous control set-MPC (CCS-MPC) and finite control-set MPC (FCS-MPC) [70]. For CCS-MPC, it is computationally intensive to obtain the optimal solution online if system constraints are incorporated. To address such issue, solutions can be pre-calculated offline using current state as a parameter and then they are stored in a lookup table for online application [71]. Although CCS-MPC can achieve satisfactory performance, FCS-MPC still gains much more attention because of its simple concept, easy implementation and good performance.

Recently, FCS-MPC is emerging as an effective control method for power converters and motor drives [61, 72–75]. During the past decade, much research has been conducted to improve the performance of FCS-MPC for application to motor drives. For high-power medium-voltage drives, solving the optimization problem with long prediction horizons is a major challenge. Various methods, such as branch and bound [61] and sphere decoding [74] are proposed, showing improved performance when extending the prediction horizon. For low and medium power drives, as the switching loss is not the main concern, much research is carried out to reduce the complexity, improve the performance and extend the application range from different types of motors to different converter topologies. To avoid nontrivial weighting factor tuning effort for torque and flux control, model predictive flux control (MPFC) is proposed in [75]. In MPFC, two scalar references, torque and flux magnitude references, are equivalently converted into a single reference of stator flux vector. While in [76], the prediction errors of different control variables are converted into ranking values. The voltage vector which leads to minimal average ranking value is selected as the best one. To obtain better steady-state performance, duty cycle optimization is introduced in [77–80]. In such methods, two voltage vectors and their duty ratios are optimized to reduce ripples of the controlled variables. In [81], the switching instant of the new selected voltage vector is not fixed at the beginning of next control period but optimized for reducing torque ripple. Though there are good prospects for MPC, some aspects, such as parameter robustness [72], weighting factor design [76, 82] and sensorless operation [73, 83] should be further investigated to improve its practicability.

4. Sensorless Control

Speed sensorless operation is preferred in many applications because of lower cost and better environmental adaptability. Various methods, such as model reference system [84], Kalman filter [73, 85] and adaptive full-order observer (AFO) [86] have been investigated for IM drives. These sensorless schemes have been successfully implemented and tested with FOC [84, 87–89], DTC [85, 90, 91] and FCS-MPC [72, 73, 83], achieving satisfactory performance over a wide speed range. But few of them clearly address the problem of starting a free-running motor. Starting a rotating motor is required in many applications, such as resumption of normal operation after power interruption, and re-powering after coasting condition of the vehicle [92]. As the initial speed is unknown under speed-sensorless operation, a large inrush current may occur due to the difference between the injected frequency of the inverter and rotating frequency of the motor. Hence, a proper scheme should be designed to achieve a safe and quick start of a rotating motor.

Among different speed sensorless observers, AFO is widely studied because it presents good accuracy and parameter robustness over a wide speed range by introducing the feedback of stator current estimation error. The research of AFO is mainly focused on improving its stability, robustness and accuracy during low speed operation [93–96]. In [97], the feedback gain matrix is designed to stabilize the observer in regenerating mode during low-speed operation. The stability of simultaneous estimation of rotor speed and stator resistance is further analyzed in [95]. To obtain the desired performance under different operating conditions, a set of feedback gains is adopted in [98]. To address poor accuracy with low sampling frequency and the risk of instability at high speed operation in discrete-time implementation, different discretization methods are studied in [88, 99] to replace conventional forward Euler method. However, there is limited research investigating AFO's performance for starting a rotating motor with unknown initial speed. In most cases, it is assumed that the motor is started from standstill. However, when the motor is rotating at a high speed, the estimated speed with a zero initial value may not converge to the actual speed. In [100], a series of estimation method to detect rotational direction and speed for free-running motors are proposed based on the response of the stator current. However, the methods by detecting current responses with specifically injected voltage are not suitable for normal operation. Hence, a separate speed estimation scheme is required which increases the complexity of the whole system. In [101], when AFO is enabled during restarting procedure, the initial estimated speed is set as the rated speed. However, if the motor can rotate at both forward and backward direction, the rotational direction must be first estimated to decide whether positive or negative rated frequency is imposed, resulting in a complex starting process.

Control Methods for PMSM Drives

1. FOC and DTC

The basic principle of FOC and DTC for PMSM drives are similar to that of IM. The merits and demerits of two control methods described for IM are also validated for PMSM. The difference is that the rotor flux position of PMSM can be directly measured by a position sensor. On the contrary, the rotor flux position in an IM is usually estimated which is typically not the same with the rotor position due to the different speed between the rotor and rotor flux under load conditions. Used as a traction motor, the q-axis inductance L_q of the PMSM is usually larger than the d-axis inductance, leading to the possibility to exploitation of the reluctance torque while weakening the magnet flux. This enables the motor to operate above the rated speed with constant power [3, 102]. However, the difference between the d-axis inductance and q-axis inductance makes the current controller design more complicated and the digital controllers presented in [5, 65] suitable for IM cannot be directly applied to the control of PMSM [6, 103].

For higher efficiency, the so-called maximum torque per ampere (MTPA) operation of PMSM is widely used in the industrial application [48, 104, 105]. Due to the high level of magnetic saturation, the inductance tends to vary in a wide range under different operation points. Thus, it is usually inaccurate to calculate the MTPA curve based on the nominal motor parameters [48]. A simple solution to this issue is to establish a look-up table through offline commission [106]. Then, the real-time d-axis and q-axis current references can be generated from the look-up table according to the torque command. Online adaption methods based on virtual signal injection and actual signal injection have also been studied [48, 104]. In this thesis, the investigation of MTPA strategies or other efficiency optimization schemes are not detailed and the traditional look-up table based MTPA is employed in the simulation and experimental tests.

In synchronous rotating reference frame, if d-axis is aligned with the rotor flux vector, the dynamic model of PMSM can be described as follows:

$$\begin{bmatrix} \frac{di_d}{dt} \\ \frac{di_q}{dt} \end{bmatrix} = \begin{bmatrix} -\frac{R_s}{L_d} & \omega_e \frac{L_q}{L_d} \\ -\omega_e \frac{L_d}{L_q} & \frac{-R_s}{L_q} \end{bmatrix} \cdot \begin{bmatrix} i_d \\ i_q \end{bmatrix} + \begin{bmatrix} \frac{1}{L_d} & 0 \\ 0 & \frac{1}{L_q} \end{bmatrix} \cdot \begin{bmatrix} u_d \\ u_q \end{bmatrix} + \begin{bmatrix} 0 \\ -\frac{\psi_{pm}}{L_q}\omega_e \end{bmatrix} \tag{2.16}$$

According to (2.16), if there is a fault of inverter during high-speed operation, high voltage as shown in (2.17) would be induced in the stator windings due to the existence of ψ_{pm} in the rotor.

$$u_q = \omega_e \psi_{pm} \tag{2.17}$$

This is a disadvantage compared to IM. For the safety reason, the power circuit for driving PMSM should be designed to be able to isolate larger voltage in case of possible failure of the inverter.

2. FCS-MPC

In [107], the basic principle of FCS-MPC for PMSM is introduced. The cost function includes three components: reference tracking, attraction region and limitations, so that the whole system can operate with good efficiency while tracking the reference without violating system limits. To reduce the effect of parameter variation, some robust approaches are studied [108–110]. In practical applications, stator resistance has little impact on the control performance during medium and high speed regions, the main problem is the variation of inductance due to saturation [111, 112]. Different values of inductance can be stored in a look-up table according to the value of i_d and i_q. In this way, the control precision can be increased without complicated online adaption but at the cost of additional memory space. Apart from improving robustness against parameter variation, another problem of FCS-MPC for PMSM is its sensorless operation. Due to the lack of a modulator, only discrete voltage vectors are available in FCS-MPC, which consist of significant ripples. In real world, due to the imperfect measurement and inaccurate system parameters, ripples of input voltage to the observer can not be perfectly compensated by the measured responses

[113, 114]. Hence, the position estimator must be designed with good capacity to reject these disturbances.

3. Sensorless Control

To achieve high performance current control of PMSMs, an accurate information of rotor position is usually required. In practice, position-sensorless operation is preferred in hostile environments and low cost applications [115, 116]. Even equipped with a position sensor, a rotor position estimator is still required to achieve sensor fault-tolerant control for safety or reliability reasons in some cases, such as in automotive applications [117]. Generally, there are two kinds of sensorless control methods. The first one is signal-injection-based methods [118–122]. These schemes are very effective especially at standstill and low-speed region. However, additional signal injection may cause higher loss, acoustic noise and less voltage margin. The other one is model based methods, which is usually adopted over medium and high-speed range. However, the external disturbance and model uncertainties, such as inverter nonlinearities, flux spatial harmonics, would induce errors in the estimation of back-EMF [123]. These non-ideal factors deteriorate the accuracy of rotor position and speed estimation. To achieve high-performance position-sensorless operation in the full-speed range, signal-injection-based methods and model based methods are often combined with a transition algorithm [124].

In [125], some design principles are introduced to improve stability and dynamic performance of full order observer (FOO). To reduce the sensitivity of extended Kalman filter (EKF) to round-off errors, different square-root algorithms based EKFs are studied and compared in [126]. Apart from FOO and EKF, sliding-mode observer

(SMO) has also been widely used because of its simplicity and satisfactory performance [116, 127, 128]. The main issues of SMO in practical application include high frequency chattering and harmonic ripples in the estimated position caused by inverter nonlinearity and flux spatial harmonics, etc.

Among the model based methods, SMO is preferable because of its simplicity, robustness against external disturbance and good dynamic performance [129, 130]. To improve the performance of SMO, at least three different methods can be found in existing researches. The first one adopts some delicate design techniques, such as higher-order SMO [129] and improved reaching law [131]. The second one analyzes the non-ideal factors in the model and then compensate for their side impacts. In [132], an online adaption method is performed to compensate the inverter nonlinearity. The spatial harmonics can also be considered to further improve the performance. Although better performance can be achieved by these methods, they are somewhat complicated and some of them require offline/online commissioning, making the control system more complex. The third one is based on signal processing technique, which extracts the fundamental components from the polluted estimation of back-EMF. For this purpose, the neural network [123], adaptive notch filter [133], synchronous frequency-extract filter [134], second-order generalized integrator [135], etc. are utilized to filter out the harmonic component in the estimated back-EMF. Among these improved methods, the signal processing-based scheme is more robust against parameter variation while the steady-state performance is pretty good [136]. However, the incorporation of different filters inevitably introduce delay during the dynamic process.

Operation with synchronized PWM schemes

On the one hand, to achieve a higher power density and wider speed range, the traction motor is usually designed with a large maximum speed. On the other hand, the switching frequency f_s of a inverter is usually limited, especially under heavy load conditions in order to reduce power losses. As a consequence, the pulse ratio $N = f_s/f_e$ defined as the ratio of the switching frequency over the fundamental frequency may become very small at high speed range with a heavy load. If the popular space vector modulation (SVM) or carrier based sinusoidal PWM (SPWM) is adopted, the significant current distortion including large low-order harmonics and sub-harmonics can be seen in the spectrum analysis when the pulse ratio N decreases to a small value (i.e., N <9) [137]. This would lead to larger loss, higher torque ripples, poorer current regulation bandwidth, etc. To address these problems, various PWM schemes have been proposed. Generally, the pulse ratio is kept constant over a speed range to eliminate the sub-harmonics, namely that it is synchronized with the output frequency of the inverter. With the continuous efforts of many researchers, synchronized SPWM, synchronized SVPWM, selective harmonic elimination PWM (SHEPWM) and current harmonic minimum PWM (CHMPWM), have been applied in practical applications to maintain satisfactory performance with small pulse ratio. [137–141].

The space vector based PWM schemes can offer some flexibilities, such as division of zero state duration and clamping one phase within a PWM interval. Utilizing these flexibilities, some advanced PWM schemes can be developed to improve the harmonic performance [142], reduce the torque ripple [143], design the synchronized symmetric PWM strategies for higher power drivers [139, 144], and so on. In [145], different synchronized PWM schemes are studied, but only the results of V/f operation are presented. In [138], the carrier based synchronized PWM is incorporated with FOC, showing good dynamic and steady state performance. However, the extraction of current harmonics is based on a leakage model, of which the machine parameters tend to vary depending on the temperature and saturation [146]. Consequently, to ensure the estimated current harmonics is in accordance with actual value in practical application, online adaption algorithm may be required.

SHEPWM and CHMPWM have also been widely studied and applied owing to their superior harmonic performance [140, 141, 147, 148]. For those PWM techniques, complex mathematical skills and calculating programs are usually required to obtain the optimal switching angles [148, 149]. To meet the demands of accuracy and cover a wide speed range operation, numerous results should be optimized offline and stored for online implementation. As those PWM techniques may introduce discontinuities in the switching angles and the flux/current trajectory may not coincide with each other at the same sampling point for different pulse patterns, it is hard to achieve high dynamic closed-loop control with SHEPWM and CHMPWM. To address this problem, trajectory tracking based methods are proposed in [137, 146, 150]. Though good results with fast dynamic responses can be obtained, they are somewhat complicated for implementation. This is because either the observer for identifying instantaneous fundamental current or the solution of a constrained online optimization problem should be established in the control system. Additionally, to improve the robustness against parameter variation, the flux trajectory control is preferred in practical application [150]. Thus, the motor current is indirectly controlled in these methods. To reduce hardware cost in some applications, the maximum current leading to over-current protection is set to be close to the rated value. It would be easier and more direct to handle current constraints if the current is directly controlled via the closed control loop. Another benefit of current control is that the current can be directly measured and controlled without designing an observer. To achieve direct current control based on synchronized PWM schemes, FOC will be selected as basic frame in this thesis.

2.5 Gearshift Control

Usually, the motor speed is electrically synchronized with the target gear during gearshift for an EV transmission [17, 151]. However, there are always uncertainties and measurement noise in practical application, hindering the perfect speed synchronization. Due to the discontinuities of speed and torque variation in the transmission during gearshift, the undesired torsional vibration may be induced. To improve driving comfort, many active damping control methods were proposed to suppress driveline oscillations. Zhang et al. [152] investigates the influence of time-varying delays due to network communication on active damping control under regenerative braking conditions. To suppress gearshift related oscillations, Walker et al. [153] develops a proportional-integral-derivative (PID) controller for vibration attenuation by manipulating motor or ICE output torque. Both controllers proposed in [152] and [153] involve integration to generate the torque reference to suppress driveline vibrations. Unfortunately, integration has an infinity gain at zero frequency and thus the controller output may be saturated during long-term operation due to minor dc-offset in the input signal resulting from unknown disturbances, imperfect measurement, and so on. In this case, active damping would lose its function because a saturated controller cannot response to the powertrain oscillations. In order to suppress vibrations in the transmission output torque during an abrupt acceleration, a linear-quadratic-Gaussian (LQG) controller is designed by Zhang et al. [154]. For active suspension of the EV driven by in-wheel motor, Shao et al. [155] proposes a fault-tolerant fuzzy H_∞ control. Though good performance can be obtained by LQG and H_∞ controllers, complex mathematical skills and computation programs are required to solve non-linear optimization problems for designing these optimal controllers. From the perspective of engineering application, a simple yet effective control method would be preferable.

Accurate torque control is essential to achieve high-quality gearshift. However, direct measurement of the torque for a rotating shaft is usually not feasible in the real world because of complex mechanical coupling and unaffordable hardware cost [32]. Thus, different techniques based on the available signals in an EV (e.g. motor speed/torque and wheel speed) have been developed for the torque estimation. Zhu et al. [31] calculates driveshaft torque based on the estimated torsion angle. To reduce the impact of unknown disturbances, such as air drag and rolling torque, H_∞ performance was employed in tuning observer parameters. Eigenvalue placement was further adopted to improve the convergence rate. For separate estimation of the torque transmitted by each clutch, reference [156] proposed a composite observer including model-based shaft observer, unknown input observers and model reference PI observer for dual clutch transmission. Considering that measured signals are always contaminated by noise in a real vehicle, Kalman filter (KF)-based estimators have also attracted much attention due to their excellent noise immunity. Rhode et al. [157] developed the standard KF and their variants with improved robustness and windup stability for the prediction of vehicle tractive forces. Wu et al. [158] compared the performance of the conventional extended KF (EKF), the dual extended KF (DEKF), and the joint extended KF (JEKF) in the application of estimating the clutch torque under model uncertainties. It is shown in [157, 158] that conventional KF cannot give satisfactory results with mismatched model and unknown disturbances whilst the improved KF schemes present better accuracy and capability of correcting inaccurate model parameters. The main difficulties of KF schemes include calculating matrix inversion in the correction step and requiring knowledge of measurement noise prior to parameter tuning. Matrix inversion is computationally intensive especially for an embedded processor and the noise characteristic cannot be easily determined as it may vary in different working conditions. Considering the above mentioned issues, a simple yet effective torque observer should be designed without requiring the information of the wheel speed, unknown vehicle resistance torque, inertial of the vehicle body, etc.. Additionally, it is better to integrate the damping control into the motor controller without the necessity of network communication. In this way, the compensation for time delay due to network communication [152] and the exhaustive effort required on improving system robustness against unknown disturbances [31] can be avoided.

Chapter 3

System Model

3.1 Control Models for IM

Fig. 3.1 shows the equivalent circuit of an IM in the stationary reference frame, where L_{ls} and L_{lr} are stator and rotor inductances respectively.

Mathematical model in the $\alpha\beta$ stationary reference frame

When the rotor flux-linkage vector $\boldsymbol{\psi}_r$ and stator current $\boldsymbol{i}_s$ are selected as state variables in the stationary reference frame, the electrical model of IM can be expressed as [159]:

$$\begin{cases} \frac{d\boldsymbol{i}_s}{dt} & = -(\frac{R_s+(L_m/L_r)^2 R_r}{\sigma L_s})\boldsymbol{i}_s + \frac{L_m}{\sigma L_s L_r}(\frac{1}{T_r} - j\omega_r)\boldsymbol{\psi}_r + \frac{1}{\sigma L_s}\boldsymbol{u}_s \\ \frac{d\boldsymbol{\psi}_r}{dt} & = \frac{L_m}{T_r}\boldsymbol{i}_s - \left(\frac{1}{T_r} - j\omega_r\right)\boldsymbol{\psi}_r \end{cases} \tag{3.1}$$

where $\boldsymbol{u}_s$, $\boldsymbol{i}_s$, R_s, R_r, L_m, L_s, L_r, ω_r and $\boldsymbol{\psi}_r$ are stator voltage vector, stator current vector, stator resistance, rotor resistance, magnetizing inductance, stator

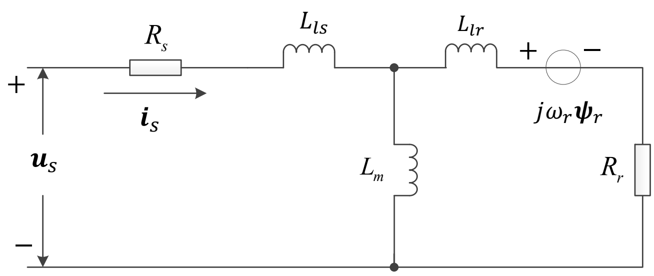

Fig. 3.1: Equivalent per phase circuit of an IM.

inductance, rotor inductance, electrical rotor speed and rotor flux-linkage vector respectively; $\sigma = 1 - L_m^2/(L_sL_r)$, $T_r = L_r/R_r$.

The stator flux can be written in terms of stator flux $\boldsymbol{\psi}_r$ and stator current $\boldsymbol{i}_s$ as

$$\boldsymbol{\psi}_s = \frac{\lambda L_m \boldsymbol{\psi}_r + \boldsymbol{i}_s}{\lambda L_r} \tag{3.2}$$

Based on (3.1) and (3.2), the dynamic model of IM can also be described by the state variables of stator current $\boldsymbol{i}_s$ and stator flux-linkage vector $\boldsymbol{\psi}_s$ as

$$\begin{cases} \frac{d\boldsymbol{i}_s}{dt} & = -[(\frac{1}{\sigma T_s} + \frac{1}{\sigma T_r}) - j\omega_r]\boldsymbol{i}_s + \frac{1}{\sigma L_s}(\frac{1}{T_r} - j\omega_r)\boldsymbol{\psi}_s + \frac{1}{\sigma L_s}\boldsymbol{u}_s \\ \frac{d\boldsymbol{\psi}_s}{dt} & = -R_s\boldsymbol{i}_s + \boldsymbol{u}_s \end{cases} \tag{3.3}$$

The electromagnetic torque can be expressed as

$$T_e = \frac{3}{2}n_p\boldsymbol{\psi}_s \otimes \boldsymbol{i}_s = \frac{3}{2}n_p\frac{L_m}{L_r}\boldsymbol{\psi}_r \otimes \boldsymbol{i}_s \tag{3.4}$$

where n_p is the number of pole pairs, $\otimes$ represents cross product.

According to (3.1), the equation in the first row can be further simplified as

$$L_\sigma \frac{d\boldsymbol{i}_s}{dt} = \boldsymbol{u}_s - R_s\boldsymbol{i}_s - \boldsymbol{u}_e \tag{3.5}$$

where $L_\sigma = \sigma L_s$ and $\boldsymbol{u}_e = L_m/L_r \cdot d\boldsymbol{\psi}_r/dt$ represents the back-electromotive force (EMF). Additionally, the derivative of $\boldsymbol{u}_e$ can be expressed as

$$\frac{d\boldsymbol{u}_e}{dt} = \frac{d\left(|\boldsymbol{u}_e|e^{j\theta_e}\right)}{dt} = \frac{d|\boldsymbol{u}_e|}{dt} + j\omega_e\boldsymbol{u}_e \tag{3.6}$$

where ω_e is the electrical speed of the rotor flux.

Mathematical model in the dq ***synchronous reference frame***

In the rotor flux oriented synchronous reference frame, the dynamic equations of IM can be described using complex state variables as follows

$$\begin{cases} L_\sigma \frac{d\boldsymbol{i}_s^e}{dt} & = -\left(R_s + j\omega_e L_\sigma\right)\boldsymbol{i}_s^e - \frac{L_m}{L_r} p\boldsymbol{\psi}_r^e - j\omega_e \frac{L_m}{L_r}\boldsymbol{\psi}_r^e + \boldsymbol{u}_s^e \\ T_r \frac{d\boldsymbol{\psi}_r^e}{dt} & = L_m \boldsymbol{i}_s^e - \left[1 + j\omega_{sl} T_r\right]\boldsymbol{\psi}_r^e \end{cases} \tag{3.7}$$

where the superscript e denotes the state variable in the dq synchronous reference frame and $\omega_{sl} = \omega_e - \omega_r$ is the slip frequency. In the rotor flux oriented synchronous reference frame, the q-axis rotor flux is zero, i.e., $\psi_q = 0$. Thus, the expression of electromagnetic torque can be simplified as

$$T_e = \frac{3}{2} n_p \frac{L_m}{L_r} \psi_d i_q \tag{3.8}$$

It is clear that if the magnitude of the rotor flux linkage ψ_d is controlled to be constant, the output torque would be proportional to the q-axis current i_q. Since the rotor flux magnitude is usually controlled to be constant, the equation (3.7) can be approximately expressed as

$$L_\sigma \frac{d\boldsymbol{i}_s^e}{dt} = -\left(R_s + j\omega_e L_\sigma\right)\boldsymbol{i}_s^e - j\omega_e \frac{L_m}{L_r}\boldsymbol{\psi}_r^e + \boldsymbol{u}_s^e \tag{3.9}$$

Apart from the electrical model, the mechanical equations can be expressed as

$$\frac{d\omega_r}{dt} = \frac{1}{J}\left(T_e - T_L - C_\omega \omega_r\right) \tag{3.10}$$

3.2 Control Models for PMSM

Mathematical model in the $\alpha\beta$ stationary reference frame

The dynamics of a PMSM can be modeled in the stationary reference frame as [160]

$$\begin{bmatrix} u_\alpha \\ u_\beta \end{bmatrix} = R_s \begin{bmatrix} i_\alpha \\ i_\beta \end{bmatrix} + \begin{bmatrix} L + \Delta L \cos(2\theta_r) & \Delta L \sin(2\theta_r) \\ \Delta L \sin(2\theta_r) & L - \Delta L \cos(2\theta_r) \end{bmatrix} \begin{bmatrix} \frac{di_\alpha}{dt} \\ \frac{di_\beta}{dt} \end{bmatrix} + \omega_e \psi_{pm} \begin{bmatrix} -\sin(\theta_r) \\ \cos(\theta_r) \end{bmatrix} \tag{3.11}$$

where R_s represents the stator resistance; $L = 0.5(L_d + L_q)$; $\Delta L = 0.5(L_d - L_q)$; L_d and L_q are d-axis and q-axis inductances respectively; ω_e denotes the electrical speed; ψ_{pm} is the permanent magnet flux; and θ_r is the rotor position.

As (3.11) involves both $2\theta_r$ and θ_r terms, it is difficult to design a rotor estimator based on the model (3.11). In practical application, the following extended EMF-based model is usually employed [106, 123, 161]

$$L_d \frac{d\boldsymbol{i}_s}{dt} = \boldsymbol{u}_s - R_s \boldsymbol{i}_s + j\omega_e (L_q - L_d)\boldsymbol{i}_s - \underbrace{j\left[(L_d - L_q)(\omega_e i_d - di_q/dt) + \omega_e \psi_{pm}\right] e^{j\theta_r}}_{\boldsymbol{u}_e} \tag{3.12}$$

where $\boldsymbol{u}_s = u_\alpha + ju_\beta$, $\boldsymbol{i}_s = i_\alpha + ji_\beta$ are stator voltage vector and stator current vector respectively, $\boldsymbol{u}_e = j[(L_d - L_q)(\omega_e i_d - di_q/dt) + \omega_e \psi_{pm}]e^{j\theta_r}$ is the extended EMF.

To improve the robustness against parameter, speed and load variation, the concept of the extended flux is developed in [160] by rewriting (3.11) as

$$L_q \frac{d\boldsymbol{i}_s}{dt} = \boldsymbol{u}_s - R_s \boldsymbol{i}_s - \frac{d\left(\psi_{ext} e^{j\theta_r}\right)}{dt} \tag{3.13}$$

where $\psi_{ext} = \psi_{pm} + (L_d - L_q)i_d$ is the extended flux.

Mathematical model in the dq synchronous reference frame

In the rotor flux oriented synchronous reference frame, the PMSM model can be expressed as

$$\begin{bmatrix} \frac{di_d}{dt} \\ \frac{di_q}{dt} \end{bmatrix} = \begin{bmatrix} -\frac{R_s}{L_d} & \omega_e \frac{L_q}{L_d} \\ -\omega_e \frac{L_d}{L_q} & \frac{-R_s}{L_q} \end{bmatrix} \cdot \begin{bmatrix} i_d \\ i_q \end{bmatrix} + \begin{bmatrix} \frac{1}{L_d} & 0 \\ 0 & \frac{1}{L_q} \end{bmatrix} \cdot \begin{bmatrix} u_d \\ u_q \end{bmatrix} + \begin{bmatrix} 0 \\ -\frac{\psi_{pm}}{L_q}\omega_e \end{bmatrix} \tag{3.14}$$

Compared with the dynamic model of IM shown in (3.9), the PMSM model is more complex due to the asymmetrical inductance in the dq reference frame. Although the equations (3.12) and (3.13) convert the PMSM model into an equivalent nonsalient-pole PMSM, they are not suitable for designing the current controller because both the extended EMF and the derivative of extended flux contain the large disturbances, i.e., $(L_d - L_q)di_q/dt$ and $(L_d - L_q)di_d/dt$, during transient processes. In [6], different gains are used for i_d and i_q control to solve the issue related to the salient machine. However, it only works fine in high-speed range [103].

The electromagnetic torque of a PMSM can be expressed as

$$T_e = \frac{3}{2} n_p (\psi_{pm} i_q + (L_d - L_q) i_d i_q) \tag{3.15}$$

3.3 Model of Dual Motor based Multi-speed Transmission

In this section, the dynamic model and characteristic of the dual motor based multi-speed transmission (DMMT) will be analyzed. Fig. 3.2 illustrates the block diagram of the powertrain model. In this study, only longitudinal dynamics is considered and the following mathematical equations can be derived based on Newtonian mechanics.

$$(J_{M1} + J_{G1} + J_{P1}/r_1^2)\ddot{\theta}_{M1} = T_{M1} - C_{M1}\dot{\theta}_{M1} - T_{D1}/r_1 - T_{D3} \tag{3.16}$$

$$(J_{M2} + J_{G2} + J_{P2}/r_2^2)\ddot{\theta}_{M2} = T_{M2} - C_{M2}\dot{\theta}_{M2} - T_{D2}/r_2 + T_{D3} \tag{3.17}$$

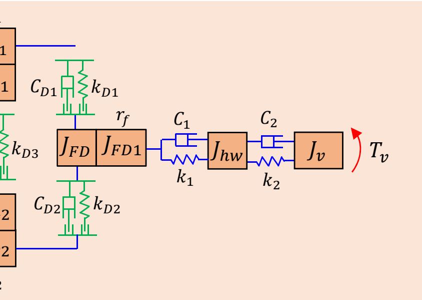

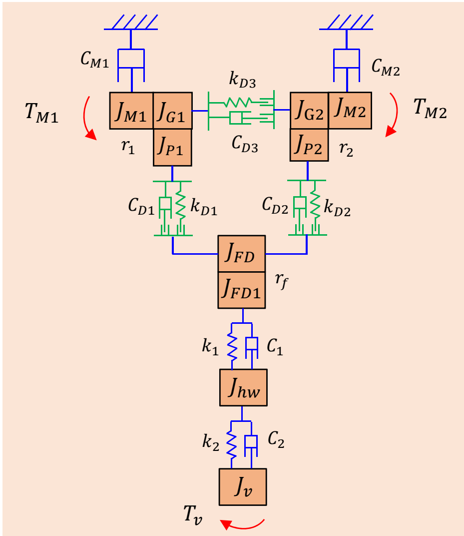

Fig. 3.2: Block diagram of the powertrain model.

$$(r_f^2 J_{FD} + J_{FD1})\ddot{\theta}_{FD1} = r_f(T_{D1} + T_{D2}) - k_1(\theta_{FD1} - \theta_h) - C_1(\dot{\theta}_{FD1} - \dot{\theta}_h) \tag{3.18}$$

$$J_h\ddot{\theta}_h = k_1(\theta_{FD1} - \theta_h) + C_1(\dot{\theta}_{FD1} - \dot{\theta}_h) - k_2(\theta_h - \theta_v) - C_2(\dot{\theta}_h - \dot{\theta}_v) \tag{3.19}$$

$$J_v\ddot{\theta}_v = k_2(\theta_h - \theta_v) + C_2(\dot{\theta}_h - \dot{\theta}_v) - T_v \tag{3.20}$$

where T_{D1}, T_{D2} and T_{D3} are the torque transmitted by the dog clutch D1, D2 and D3 respectively; θ is angular displacement; J denotes the inertia of an element and r represents gear ratio. Subscripts $M1$, $M2$, FD, h, v represent motor M1, motor M2, final drive, half shaft and vehicle body respectively. More details about these symbols expressed in the equations (3.16)-(3.20) have been summarized in Table A.1 in Appendix. The contact force of dog clutch is zero when the clutch is disengaged and it is calculated as (3.21)-(3.23) when the clutch is engaged.

$$T_{D1} = k_{D1}(\theta_{M1}/r_1 - r_f\theta_h) + C_{D1}(\dot{\theta}_{M1}/r_1 - r_f\dot{\theta}_h) \tag{3.21}$$

$$T_{D2} = k_{D2}(\theta_{M2}/r_2 - r_f\theta_h) + C_{D1}(\dot{\theta}_{M2}/r_2 - r_f\dot{\theta}_h) \tag{3.22}$$

$$T_{D3} = k_{D3}(\theta_{M1} - \theta_{M2}) + C_{D3}(\dot{\theta}_{M1} - \dot{\theta}_{M2}) \tag{3.23}$$

The detailed model during the engagement and disengagement processes of the dog clutch is not considered here for simplicity because the torque transmitted by the clutch is controlled to be zero in such process by the proposed gearshift control. Thus, the dynamics of dog clutch in these stages has little impact on the powertrain responses. Nevertheless, a simple time delay is employed to capture the time required for the actuator to complete engagement/disengagement. In (3.20), T_v is the resistance torque including rolling resistance, air drag and inclined resistance, which can be expressed as [158]

$$T_v = \left(C_v m_v g \cos\varphi + \frac{1}{2}\rho A C_d v^2 + m_v g \sin\varphi \right) r_w \tag{3.24}$$

where m_v is the vehicle mass, g represents gravity acceleration, C_v denotes rolling resistance coefficient, φ is the incline angle of the road, ρ is the air density, A is the vehicle frontal area and r_w is the tire radius.

Typically, the inner flux and torque control loop of an AC machine can be simplified as a first order system [47]. Hence, the relationship between the output torque T_M and the torque command T_M^{ref} can be described by

$$G_M(s) = \frac{T_M}{T_M^{ref}} = \frac{1}{\tau s + 1} \tag{3.25}$$

where τ is a time constant whose typical value is around $1-5$ms and s is the Laplace operator. To evaluate the driveline oscillations, the variable $\Delta\omega_1 = \omega_{M1} - r_1 r_f \omega_v$ and $\Delta\omega_2 = \omega_{M2} - r_2 r_f \omega_v$ are defined for the motor M1 and M2 respectively. The defined $\Delta\omega$ represents the speed difference between the motor and vehicle which is indicative of vibrations in the powertrain and such information can be used for vibration damping control [153]. Based on DMMT dynamic equations (3.16)-(3.20), the transfer function of $\Delta\omega_1(s)$ and $\Delta\omega_2(s)$ to the torque command T_M^{ref} can be

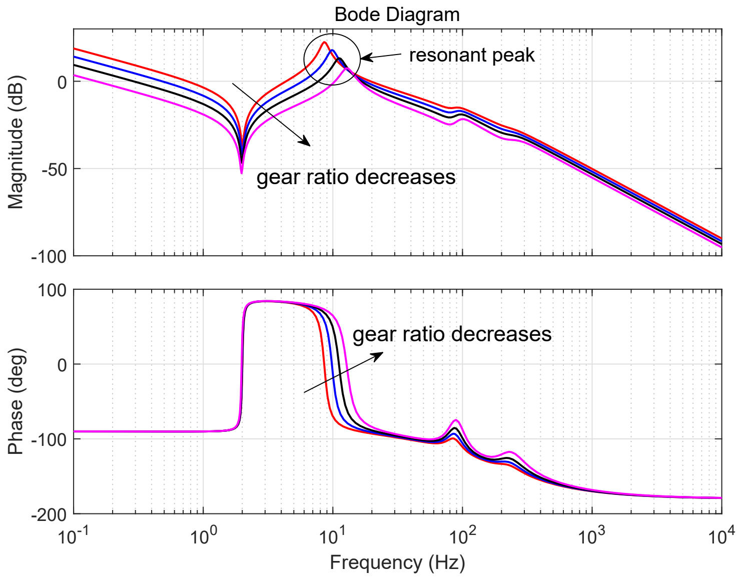

Fig. 3.3: Bode diagram of $G_{pt}(s)$ with different gear ratios.

derived. As analytical expression is too complex and lengthy, it is not expressed here for simplicity. Nevertheless, numerical result is calculated as follow when the motor M1 is connected to the gear G1.

$$\begin{aligned} G_{pt}(s) &= \frac{\Delta\omega_1(s)}{T_M^{ref}(s)} \\ &= \frac{6.78\text{e}4s^6 + 2.29\text{e}8s^5 + 5.99\text{e}11s^4 + 1.64\text{e}14s^3 + 1.54\text{e}17s^2 + 8.21\text{e}16s + 2.37\text{e}19}{s^8 + 4652s^7 + 1.3\text{e}7s^6 + 1.3\text{e}10s^5 + 6.6\text{e}12s^4 + 3.4\text{e}15s^3 + 1.2\text{e}17s^2 + 2.6\text{e}19s + 7.5\text{e}14} \end{aligned} \tag{3.26}$$

The bode diagram of the system (3.26) is shown in Fig. 4.6. Following the same procedure, the case when the motor M1 is connected to the other gear pairs can also be obtained. As shown in Fig. 4.6, four resonant peaks are clearly observable in the magnitude-frequency responses indicating the system damping is very low at these points and thus driveline oscillations can be easily induced during transient process. When the gear ratio decreases, the resonant peak decreases as well with resonant frequency shifts from 8.9 Hz to 14.4 Hz. As stated in [162], the oscillations around the frequency range 1 Hz - 10 Hz have large impact on the driving comfort.

Therefore, active damping control is essential for the presented DMMT to suppress low-frequency vibrations.

3.4 Summary

In this chapter, the mathematical models of IM, PMSM and DMMT are introduced. These dynamic models are fundamentals for the theoretical analysis and the design of observers and controllers in the following chapters. Unlike the IM model in the synchronous reference frame, PMSM model in the synchronous reference frame has different values of terms on the diagonal and antidiagonal in the evolution matrix. Additionally, we need to write the matrix in the synchronous reference frame to follow the anisotropy thereby simplifying their expression because the dq-axis inductances could be different in the PMSM model [163]. The analysis of the DMMT model shows that the powertrain damping at some specific frequencies are poor which may result in vibrations when the motor torque varies. To achieve better driving comfort, the proper control scheme should be designed.

Chapter 4

Control of Induction Motor Drives

4.1 Introduction

Induction motor (IM) features low cost, wide availability and easy construction [102]. As a traction motor, its maximum speed is designed to be very high for higher power density. For example, the speed of the IM adopted in the Tesla Model S P85 can be up to 15840 rpm. Considering it is a 2 pole pairs machine, the maximum electrical frequency is 528 Hz (31680 rpm).

To reduce the inverter power losses, the switching frequency f_s of a inverter is limited, especially under heavy load conditions. As a result, the pulse ratio $N = f_s/f_e$, i.e., the pulse number during one fundamental cycle, may become very small at high-speed operation under heavy load conditions. With a low pulse ratio N, the discretization effect cannot be ignored and must be carefully considered when designing the current controllers. Otherwise, deteriorated control performance or even instability could be observed [5, 63]. Hence, the conventional method, i.e., designing the current controller in the continuous-time domain with subsequent discretization for digital implementation can not guarantee the desired performance

Part of this chapter has been pulished in [164–167].

over the full speed-torque range.

To deal with the increased cross-coupling caused by the relatively larger sampling delay under low pulse ratio, a first-order delay model is used in the design of a complex-coefficient current controller [64]. It is shown that the transient performance is significantly improved if the signal delay is explicitly considered. To address the issue of instability at high-speed operation, a voltage compensation strategy is proposed in [63]. Both controllers in [63] and [64] are designed in the continuous-time domain and thus a discretization method is required for digital implementation. Without proper discretization, the controller performance may be degraded in practical implementation. For better performance, it is suggested to design controllers directly in the discrete-time domain [5, 65]. As the discrete nature of the digital implementation, such as sampling delay and zero-order-hold (ZOH), can be explicitly considered in the design stage, the bandwidth and improved coupling performance may be obtained by using the discrete-time controller. In this chapter, a discrete-time predictive current controller with disturbance estimation is proposed to achieve fast dynamic response and good robustness against parameter mismatches. The comparison with the prior discrete-time controller [5] is presented to validate its effectiveness.

To satisfy the demand over a wide speed range and different load conditions, a combination of PWM schemes with different pulse patterns may be employed in practical application. This imposes the requirement of smooth transition between different PWM methods. Especially for the synchronized PWM schemes, the sudden jump of the switching frequency caused by the change of the pulse ratio make the smooth transition difficult. In [141], the transition is enabled when the voltage angle falls into a fixed range. But the selection of this range is not clearly addressed with theory analysis. In [168], the transition is started when the harmonic current is around zero. It is shown that the transition is smooth. However, the gate pulses of three phases are shifted separately at different points, increasing the complexity and duration of PWM shifting process. To improve the overall performance, SHEPWM is employed in [140] during steady-state operation while it is switched to SVPWM during dynamic process. The smooth transition is achieved by optimizing the switching state so that there is no more than one pulse jump during transition. As the the pulse number is as high as 29 in quarter fundamental cycle, the harmonic current is very small and nearly zero. According to [168], the transition can be started at any positions. Since operation with low switching frequency presents abundant harmonic components, this method is not applicable when the pulse number is low. In [137, 150], the dynamic error caused by transition between different pulse patterns is combined with the tracking error induced by load change, reference variation, etc. All these disturbances are compensated in the controller by directly manipulating original switching instants according to the tracking error of stator flux. As the problem of achieving smooth transition is solved in the design of controller, it is applicable for various pulse patterns. In this thesis, the dynamic error induced by transition between different pulse patterns will not be compensated in the controller but solved in the modulation stage. In this way, the controller design and modulation schemes are decoupled. Namely, it is not necessary for inner current controller to consider the effect of shifting between different pulse patterns. Thus, the proposed method can be easily implemented with existing current controllers.

To achieve speed-sensorless operation, the adaptive full-order observer (AFO) is employed [165, 167]. The presented AFO is simple and effective, which is not only suitable for the initial speed estimation but also applicable for normal operation. First, convergence condition of the estimated speed based on AFO is deduced. Then, a feedback gain matrix is proposed to ensure the successful start of the motor with any initial speed. Finally, its detailed implementation is demonstrated with simulation and experimental verification.

4.2 Adaptive Flux Observer and Restarting Free-running Motor

4.2.1 Basic Principle of AFO

For high-performance motor control, accurate flux information is usually essential. Based on (3.1), the AFO can be constructed as

$$s\hat{\boldsymbol{x}} = \boldsymbol{A}\hat{\boldsymbol{x}} + \boldsymbol{B}\boldsymbol{u}_s + \boldsymbol{G}(\boldsymbol{i}_s - \hat{\boldsymbol{i}}_s) \tag{4.1}$$

$$\boldsymbol{A} = \begin{bmatrix} -\frac{1}{T_\sigma} & \lambda L_m(\frac{1}{T_r} - j\hat{\omega}_r) \\ \frac{L_m}{T_r} & -\frac{1}{T_r} + j\hat{\omega}_r \end{bmatrix} \tag{4.2}$$

$$\boldsymbol{B} = \begin{bmatrix} \frac{1}{L_\sigma} \\ 0 \end{bmatrix} \tag{4.3}$$

$$\boldsymbol{G} = \begin{bmatrix} \boldsymbol{g}_1 \\ \boldsymbol{g}_2 \end{bmatrix} = \begin{bmatrix} g_{1r} + j \cdot g_{1i} \\ g_{2r} + j \cdot g_{2i} \end{bmatrix} \tag{4.4}$$

where $\sigma = 1 - L_m^2/(L_sL_r)$, $T_\sigma = \sigma L_s/\left(R_s + (L_m/L_r)^2R_r\right)$, $\lambda = 1/(L_sL_r - L_m^2)$, $T_r = L_r/R_r$, $\hat{\boldsymbol{x}} = \begin{bmatrix} \hat{\boldsymbol{i}}_s & \hat{\boldsymbol{\psi}}_r \end{bmatrix}^T$ and $\boldsymbol{G}$ is the feedback gain matrix of AFO. The speed can be estimated based on the conventional adaptation law as [93, 96]

$$\frac{d\hat{\omega}_r}{dt} = (\boldsymbol{i}_s - \hat{\boldsymbol{i}}_s) \otimes \hat{\boldsymbol{\psi}}_r \tag{4.5}$$

$$= \left|\boldsymbol{i}_s - \hat{\boldsymbol{i}}_s\right| \cdot \left|\hat{\boldsymbol{\psi}}_r\right| \sin\theta. \tag{4.6}$$

where, $\otimes$ represent cross-product of two complex variables, and θ is the phase angle between the complex vector $\hat{\boldsymbol{\psi}}_r$ and $(\boldsymbol{i}_s - \hat{\boldsymbol{i}}_s)$, namely

$$\theta = \text{angle}(\hat{\psi}_r) - \text{angle}(\boldsymbol{i}_s - \hat{\boldsymbol{i}}_s). \tag{4.7}$$

In practical applications, a proportional-integral (PI) controller is generally used to obtain $\hat{\omega}_r$ as

$$\hat{\omega}_r = (k_{p\omega} + k_{i\omega}/s) \cdot \left((\boldsymbol{i}_s - \hat{\boldsymbol{i}}_s) \otimes \hat{\boldsymbol{\psi}}_r\right) \tag{4.8}$$

Fig. 4.1 shows the schematic diagram of the AFO. For better accuracy in digital implementation, the so-called Heun's method [169] is used to discretize (4.1) and the results are show as follows.

$$\begin{cases} \hat{\boldsymbol{x}}_p^{k+1} & = \hat{\boldsymbol{x}}^k + T_{sc}(\boldsymbol{A}\hat{\boldsymbol{x}}^k + \boldsymbol{B}\boldsymbol{u}_s^k + \boldsymbol{G}(\boldsymbol{i}_s - \hat{\boldsymbol{i}}_s)) \\ \hat{\boldsymbol{x}}^{k+1} & = \hat{\boldsymbol{x}}_p^{k+1} + \frac{T_{sc}}{2}\boldsymbol{A}(\hat{\boldsymbol{x}}_p^{k+1} - \hat{\boldsymbol{x}}^k) \end{cases} \tag{4.9}$$

4.2.2 Analysis of Speed Convergence Condition

First, the following Lyapunov function is defined.

$$V = \frac{(\omega_r - \hat{\omega}_r)^2}{2} \tag{4.10}$$

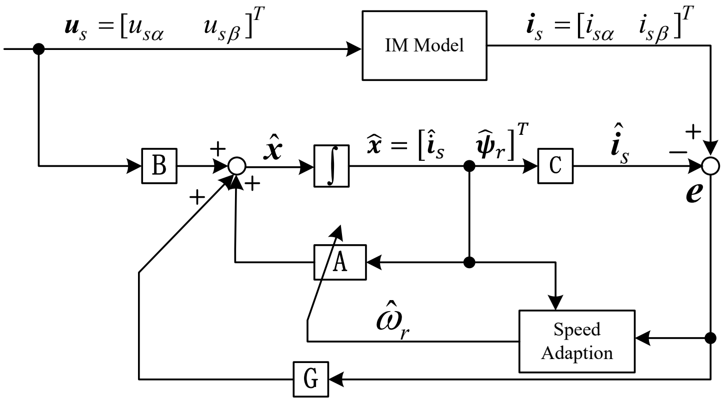

Fig. 4.1: Schematic diagram of the AFO.

Supposing that ω_r is constant during one control period [170], the time derivative of V is

$$\frac{dV}{dt} = -(\omega_r - \hat{\omega}_r) \cdot \frac{d\hat{\omega}_r}{dt} \tag{4.11}$$

$\hat{\omega}_r$ will always approach to ω_r, if

$$\frac{dV}{dt} < 0 \tag{4.12}$$

Namely, if equation (4.13) holds, the estimated speed $\hat{\omega}_r$ will converge to the actual speed ω_r.

$$\mathrm{sign}(\omega_r - \hat{\omega}_r) \cdot \frac{d\hat{\omega}_r}{dt} > 0 \tag{4.13}$$

According to (4.6), (4.13) can be equivalently rewritten as

$$\mathrm{sign}(\omega_r - \hat{\omega}_r) \cdot \mathrm{sign}(\sin\theta) > 0 \tag{4.14}$$

From (3.1) and (4.1), the estimation error of stator current and rotor flux can be derived as shown in the following equations [97].

$$\begin{bmatrix} s\boldsymbol{e}_i \\ s\boldsymbol{e}_\psi \end{bmatrix} = F \begin{bmatrix} \boldsymbol{e}_i \\ \boldsymbol{e}_\psi \end{bmatrix} + H \begin{bmatrix} \hat{\boldsymbol{i}}_s \\ \hat{\boldsymbol{\psi}}_s \end{bmatrix} \tag{4.15}$$

$$F = \begin{bmatrix} -\frac{1}{T_\sigma} - \boldsymbol{g}_1 & \lambda L_m(\frac{1}{T_r} - j\omega_r) \\ \frac{L_m}{T_r} - \boldsymbol{g}_2 & -\frac{1}{T_r} + j\omega_r \end{bmatrix} \tag{4.16}$$

$$H = \begin{bmatrix} 0 & -j\lambda L_m \triangle\omega_r \\ 0 & j\triangle\omega_r \end{bmatrix} \tag{4.17}$$

Based on (4.15), transfer function $N(s)$ can be derived as expressed in (4.18).

$$N(s) = \frac{\hat{\boldsymbol{\psi}}_r}{(\boldsymbol{i}_s - \hat{\boldsymbol{i}}_s)} = \frac{s^2 + (h_1 + jh_2)\cdot s + d_1 + jd_2}{-j\triangle\omega_r \cdot \lambda L_m \cdot s} \tag{4.18}$$

$$h_1 = (g_{1r} + \frac{R_s}{\sigma L_s} + \frac{R_r}{\sigma L_r}) \tag{4.19}$$

$$h_2 = (g_{1i} - \omega_r) \tag{4.20}$$

$$d_1 = \frac{1}{T_r}(g_{1r} + \frac{R_s}{\sigma L_s} + \lambda L_m g_{2r}) + \omega_r(g_{1i} + \lambda L_m g_{2i}) \tag{4.21}$$

$$d_2 = \frac{1}{T_r}(g_{1i} + \lambda L_m g_{2i}) - \omega_r(g_{1r} + \frac{R_s}{\sigma L_s} + \lambda L_m g_{2r}) \tag{4.22}$$

When estimating the free-running speed, torque reference is set as zero, namely the slip frequency is zero. Hence, the output frequency of the inverter equals the estimated speed $\hat{\omega}_r$. According to (4.18) and assuming $s = j\hat{\omega}_r$, $N(j\hat{\omega}_r)$ can be derived as:

$$N(j\hat{\omega}_r) = \frac{-\hat{\omega}_r^2 + d_1 - h_2\hat{\omega}_r + j(h_1\hat{\omega}_r + d_2)}{\lambda L_m \hat{\omega}_r \triangle\omega_r}. \tag{4.23}$$

Furthermore, $\hat{\boldsymbol{\psi}}_r/(\boldsymbol{i}_s - \hat{\boldsymbol{i}}_s)$ can be expressed in a different way as shown in (4.24).

$$\frac{\hat{\boldsymbol{\psi}}_r}{(\boldsymbol{i}_s - \hat{\boldsymbol{i}}_s)} = \left|\frac{\hat{\boldsymbol{\psi}}_r}{\boldsymbol{i}_s - \hat{\boldsymbol{i}}_s}\right| e^{j\theta} = \frac{\left|\hat{\boldsymbol{\psi}}_r\right|}{\left|\boldsymbol{i}_s - \hat{\boldsymbol{i}}_s\right|}(\cos\theta + j\sin\theta) \tag{4.24}$$

Comparing (4.23) and (4.24), it can be easily found that the sign of $\sin\theta$ is the same as the sign of imaginary part of $N(j\hat{\omega}_r)$. Hence, the condition (4.14) can be changed as:

$$\mathrm{sign}(\hat{\omega}_r)\cdot\mathrm{sign}(h_1\hat{\omega}_r+d_2)>0 \tag{4.25}$$

If feedback gain matrix is set as zero, the estimated speed can always converge to ω_r only when $\hat{\omega}_r$ satisfies the following conditions.

$$|\hat{\omega}_r|>(\frac{L_rR_s}{L_rR_s+R_rL_s})\,|\omega_r| \tag{4.26}$$

It is clear that if motor is rotating at a high speed, $\hat{\omega}_r$ can not converge to ω_r when $\hat{\omega}_r$ is initially set as zero. This problem can be solved by setting $\hat{\omega}_r$ to a sufficiently large value with the same sign of ω_r, as can be seen from (4.26). However, if the motor can rotate at both forward and backward direction, the rotational direction must be estimated before determining whether $\hat{\omega}_r$ is set to a positive or a negative value. To avoid the estimation of rotational direction, the feedback gain matrix is adjusted so that $d_2=0$. If $d_2=0$, the condition (4.25) deduced from (4.23) can be simplified as:

$$h_1>0 \tag{4.27}$$

By solving (4.27) and $d_2=0$, a simple gain matrix $\boldsymbol{G}$ is proposed as shown in (4.28).

$$\boldsymbol{G}=\begin{bmatrix}-\frac{R_s}{\sigma L_s}\\ 0\end{bmatrix} \tag{4.28}$$

With the proposed feedback gain matrix (4.28), the estimated speed can always converge to the actual speed with any initial value. As only the feedback gain matrix is changed, it is very simple in implementation.

4.2.3 Starting a Rotating Motor

In many cases, such as resuming to normal operation after short power interruption, starting a machine rotated by external load or re-powering after coasting condition of an electric vehicle, the motor needs to be started with nonzero speed. During the estimation of free-running speed, the PI controller for speed regulation is disabled and i_q^{ref} is set as zero. i_d^{ref} is set as its maximum value I_{dmax} to minimize the process for building rotor flux. To respond to both forward and backward rotational direction quickly, the initial value of $\hat{\omega}_r$ is set as zero. As analyzed in section 4.2.2, the estimated speed $\hat{\omega}_r$ can converge to the actual speed ω_r with the proposed feedback gain matrix (4.28) even if there is a large initial difference. The remaining problem is to judge whether $\hat{\omega}_r$ is close to ω_r and thus the normal operation can be subsequently enabled.

When $\hat{\omega}_r$ approaches to ω_r, $d\hat{\omega}_r/dt$ in (4.5) becomes smaller. Hence, if the filtered value of $d\hat{\omega}_r/dt$ is smaller than a predefined threshold, the estimation of free-running speed is terminated and normal operation is enabled. As $d\hat{\omega}_r/dt$ is zero before the

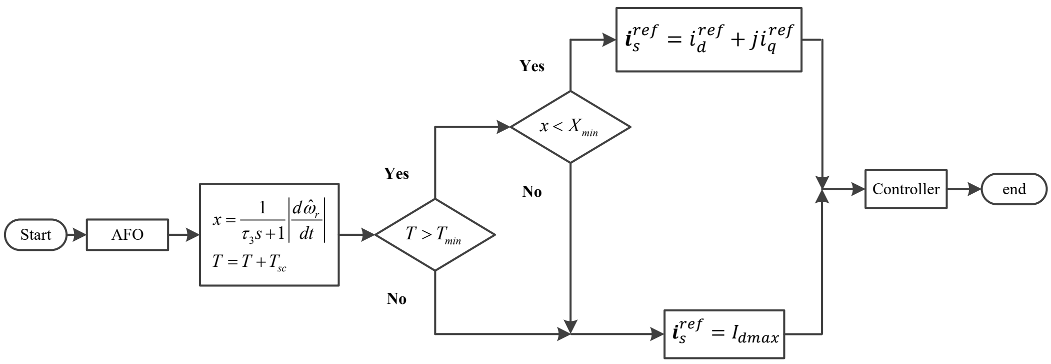

Fig. 4.2: Procedure of starting a free-running IM.

control system is activated, a minimum time T_{min} is hold for the estimation of free-running speed to improve the reliability. The flow chart of the proposed procedure is shown in Fig. 4.2.

4.3 Current Control Under Low Pulse Ratio

4.3.1 Parameter Tuning of Discrete-time Current Controller

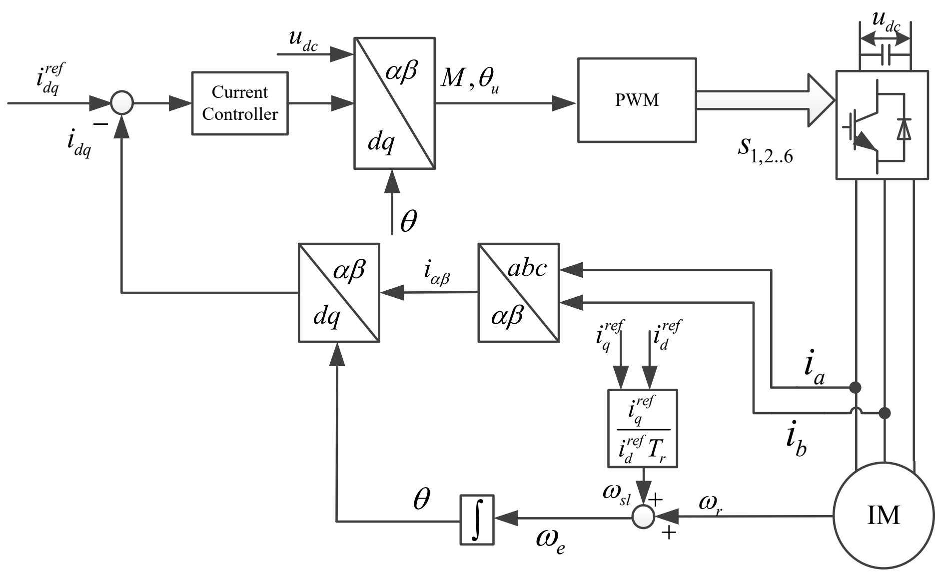

Fig. 4.3: Control diagram of FOC for IM drives.

Fig. 4.3 shows the control diagram of the indirect FOC for IM drives. In practical application, there is usually one step digital delay between the reference voltage and the applied voltage [63, 171]. As a consequence, the voltage command computed at the kth control period cannot change the $(k+1)$th instant current but only can regulate the current at the $(k+2)$th instant. According to (3.9) and assuming that the machine speed ω_e is constant during a short period, the current sampled at the

$(k+2)$th instant can be calculated by solving the differential equation as [172]

$$\boldsymbol{i}_{dq}^{k+2} = e^{-(1/\tau + j\omega_e)T_{sc}} \boldsymbol{i}_s^{k+1} + \frac{1}{L_\sigma} \int_0^{T_{sc}} e^{-(1/\tau + j\omega_e)(t - T_{sc})} \left[\boldsymbol{u}_{dq}(t) - \boldsymbol{u}_{emf}(t)\right] dt \tag{4.29}$$

where the superscript k denotes a kth instant variable, T_{sc} is the sampling period, and $\tau = L_\sigma / R_s$. Considering the one step digital delay, zero-order-hold (ZOH) characteristic of the inverter and the fact that the d axis is rotating at the speed of ω_e, the actual $\boldsymbol{u}_{dq}(t)$ is

$$\boldsymbol{u}_{dq}(t) = \boldsymbol{u}_{dq}^k e^{-j\omega_e (T_{sc} + t)} \tag{4.30}$$

The back electromotive force (EMF) $\boldsymbol{u}_{emf} = j\omega_e \frac{L_m}{L_r} \psi_d$ is assumed to be constant, i.e., $\boldsymbol{u}_{emf}(t) = \boldsymbol{u}_{emf}^k$. Then, the current response in (4.29) can be expressed as

$$\begin{aligned} \boldsymbol{i}_{dq}^{k+2} = e^{-(1/\tau + j\omega_e)T_{sc}} \boldsymbol{i}_s^{k+1} - \frac{1 - e^{-(1/\tau + j\omega_e)T_{sc}}}{R + j\omega_e L} \boldsymbol{u}_{emf}^k \\ + \frac{e^{-j\omega_e T_{sc}}(1 - e^{-T_{sc}/\tau})}{R} e^{-j\omega_e T_{sc}} \boldsymbol{u}_{dq}^k \end{aligned} \tag{4.31}$$

Based on (4.31), the following discrete-time transfer function can be obtained

$$\frac{\boldsymbol{i}_{dq}(z)}{\boldsymbol{u}_{dq}(z)} = \frac{1}{R_s} \frac{e^{-j\omega_e T_{sc}} - e^{-(1/\tau + j\omega_e)T_{sc}}}{z e^{j\omega_e T_{sc}} (z - e^{-(1/\tau + j\omega_e)T_{sc}})} \tag{4.32}$$

Based on the principle of zero/pole cancellation [5], a digital current controller can be constructed as follow

$$G_d(z) = k_d \frac{1 - z^{-1} \cdot e^{-(1/\tau + j\omega_e)T_{sc}}}{(1 - z^{-1})} e^{2j\omega_e T_{sc}} \tag{4.33}$$

The results presented in [5] show that the performance of current controllers designed in $s-$domain degrades significantly when compared to (4.33) if the pulse ratio decreases. Though good results are presented, a proper selection of gain k_d is not clearly addressed. Owing to the simple structure and good performance, the

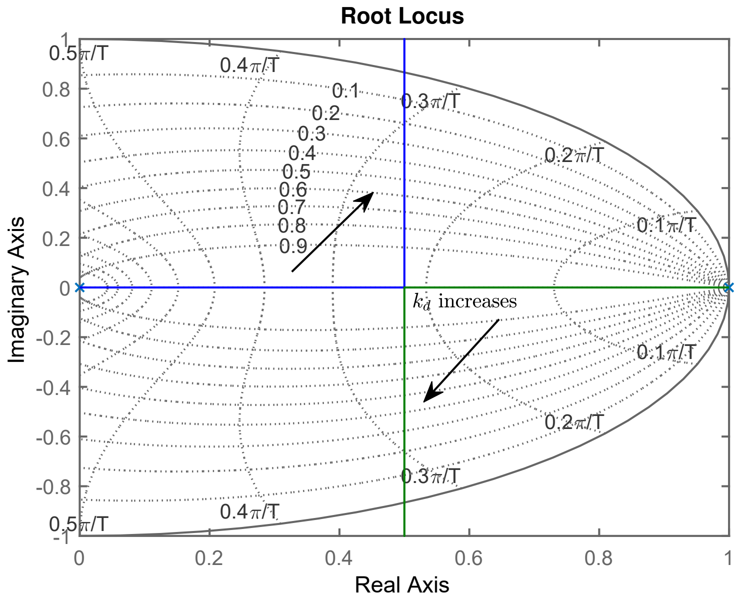

Fig. 4.4: Root locus of the current control loop.

gain k_d of the digital current controller (4.33) will be investigated in the following text.

Based on (4.32) and (4.33), the closed-loop transfer function can be deduced as

$$G(z) = \frac{R}{R_s \cdot z^2 - R_s \cdot z + R} \tag{4.34}$$

$$R = k_d(1 - e^{-T_{sc}/\tau}) \tag{4.35}$$

The pole of $G(z)$ can be obtained according to the above two equations as

$$p_{1,2} = \frac{R_s \pm \sqrt{(R_s)^2 - 4 \cdot R_s \cdot R}}{2 \cdot R_s} \tag{4.36}$$

As indicated by the root locus of current loop shown in Fig. 4.4, if two poles coincide with each other, the damping ratio is unity and the decay rate reaches its maximum value [173, 174]. Thus, there is ideally no overshoot while the dynamic performance is satisfactory. Hence, by making square root in (4.36) equal to zero, k_d can be

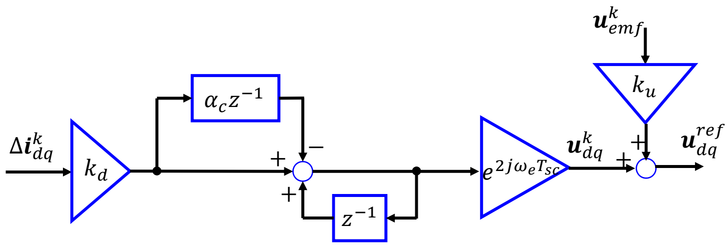

Fig. 4.5: Block diagram of the current controller (4.33).

obtained as

$$k_d = \frac{R_s}{4(1 - e^{-T_{sc}/\tau})}. \tag{4.37}$$

From (4.31), it is clear that the following voltage should be added to the voltage command to decouple the influence of the back EMF.

$$\boldsymbol{u}_d^k = \boldsymbol{u}_{emf}^k \underbrace{\frac{e^{j\omega_e T_{sc}}}{1 + j\omega_e \tau} \frac{e^{j\omega_e T_{sc}} - e^{-T_{sc}/\tau}}{1 - e^{-T_{sc}/\tau}}}_{k_u} \tag{4.38}$$

The block diagram of the current controller (4.33) is shown in Fig. 4.5, where

$$\alpha_c = e^{-(1/\tau + j\omega_e)T_{sc}} \tag{4.39}$$

4.3.2 Discrete-time Predictive Current Control

Although the discrete-time current controller developed in [5] can operate stably under low pulse ratio, it suffers from relatively slow dynamic response. To improve the dynamic performance and the robustness against parameter mismatches, a discrete-time predictive current controller (DPCC) will be designed in this section.

Assuming a constant speed during each sampling period, the discretized model of (3.5) can be described as

$$\boldsymbol{i}_s^{k+1} = \frac{1}{L_\sigma}\int_0^{T_{sc}} e^{-(t-T_{sc})/\tau}\left(\boldsymbol{u}_s(t) - \boldsymbol{u}_{emf}\right)dt + e^{-T_{sc}/\tau}\boldsymbol{i}_s^k \tag{4.40}$$

For a inverter-fed IM drive, the voltage $\boldsymbol{u}_s$ can be assumed as a constant during the sampling period, i.e.,

$$\boldsymbol{u}_s(t) = \boldsymbol{u}_s(k) \tag{4.41}$$

If only the fundamental component is considered, the back EMF term $\boldsymbol{u}_{emf}(t)$ can be expressed as

$$\boldsymbol{u}_{emf}(t) = \boldsymbol{u}_{emf}^k e^{j\omega_e t} \tag{4.42}$$

Substituting (4.41) and (4.42) into (4.40) yields [175]

$$\boldsymbol{i}_s^{k+1} = e^{-T_{sc}/\tau}\boldsymbol{i}_s^k + \frac{1-e^{-T_{sc}/\tau}}{R_s}\boldsymbol{u}_s^k - \frac{e^{j\omega_e T_{sc}} - e^{-T_{sc}/\tau}}{R_s + j\omega_e L_\sigma}\boldsymbol{u}_{emf}^k \tag{4.43}$$

According to (4.43), the reference voltage that force the stator current to arrive its reference at the next sampling period can be computed as

$$\left(\boldsymbol{u}_{s1}^k\right)^{ref} = \frac{\hat{R}_s}{1-e^{-T_{sc}/\hat{\tau}}}\left[\left(\boldsymbol{i}_s^{k+1}\right)^{ref} - e^{-T_{sc}/\hat{\tau}}\boldsymbol{i}_s^k + + \frac{e^{j\omega_e T_{sc}} - e^{-T_{sc}/\hat{\tau}}}{\hat{R}_s + j\omega_e \hat{L}_\sigma}\boldsymbol{u}_{emf}^k\right] \tag{4.44}$$

where the hat ˆ denotes the estimated variable. As (4.44) is directly calculated based on the system model, the calculated voltage would not achieve the desired tracking performance in practical application due to the imperfect prior-knowledge of motor parameters, unknown disturbances, etc.

Using the estimated stator resistance $\hat{R}_s$ and inductance $\hat{L}_\sigma$, the system model (3.5) can be rewritten as

$$\hat{L}_\sigma\frac{d\boldsymbol{i}_s(t)}{dt} = \boldsymbol{u}_s(t) - \hat{R}_s\boldsymbol{i}_s(t) - \hat{\boldsymbol{u}}_{emf}(t) - \boldsymbol{u}_d(t) \tag{4.45}$$

where

$$\boldsymbol{u}_d = -\Delta L \cdot d\boldsymbol{i}_s(t)/dt - \Delta R \boldsymbol{i}_s(t) - \Delta \boldsymbol{u}_e(t) \tag{4.46}$$

is the disturbance voltage compensating for the inconsistency between (3.5) and (4.45); $\Delta L = L - \hat{L}_\sigma$, $\Delta R = R_s - \hat{R}_s$ and $\Delta \boldsymbol{u}_e = \boldsymbol{u}_{emf} - \hat{\boldsymbol{u}}_{emf}$ are estimation errors of the inductance, resistance and back EMF respectively. Similar to the derivation of (4.43), the following equation can be obtained

$$\boldsymbol{i}_s^{k+1} = e^{-T_{sc}/\hat{\tau}} \boldsymbol{i}_s^k + \frac{1 - e^{-T_{sc}/\hat{\tau}}}{\hat{R}_s} \boldsymbol{u}_s^k - \frac{e^{j\omega_e T_{sc}} - e^{-T_{sc}/\hat{\tau}}}{\hat{R}_s + j\omega_r \hat{L}_\sigma} \left(\hat{\boldsymbol{u}}_{emf}^k + \boldsymbol{u}_d^k \right) \tag{4.47}$$

It should be noted that only the fundamental component of $\boldsymbol{u}_d$ is considered in (4.47). The dynamics of $\boldsymbol{u}_d$ can thus be expressed as

$$\boldsymbol{u}_d^{k+1} = e^{j\omega_e T_{sc}} \boldsymbol{u}_d^k \tag{4.48}$$

According to (4.47), the voltage forcing the stator current to reach its reference can be calculated as

$$\left(\boldsymbol{u}_{s2}^k \right)^{ref} = \frac{\hat{R}_s}{1 - e^{-T_{sc}/\hat{\tau}}} \left\{ \left(\boldsymbol{i}_s^{k+1} \right)^{ref} - e^{-T_{sc}/\hat{\tau}} \boldsymbol{i}_s^k + + \frac{e^{j\omega_e T_{sc}} - e^{-T_{sc}/\hat{\tau}}}{\hat{R}_s + j\omega_r \hat{L}_\sigma} \left[\hat{\boldsymbol{u}}_{emf}^k + \boldsymbol{u}_d^k \right] \right\} \tag{4.49}$$

Comparing (4.44) and (4.49), it can be seen that the additional disturbance voltage $\boldsymbol{u}_d$ is required to achieve the desired control target when the estimated motor parameters are used in the control algorithm. However, since the actual motor parameters is unknown, it is difficult to obtain its value directly. In the following text, an adaptive disturbance estimation will be developed. According to (4.47), the following equation can be derived

$$\left(\boldsymbol{i}_s^k \right)^{ref} = e^{-T_{sc}/\hat{\tau}} \boldsymbol{i}_s^{k-1} + \frac{1 - e^{-T_{sc}/\hat{\tau}}}{\hat{R}_s} \boldsymbol{u}_{s2}^{k-1} - \frac{e^{j\omega_e T_{sc}} - e^{-T_{sc}/\hat{\tau}}}{\hat{R}_s + j\omega_e \hat{L}_\sigma} \left(\hat{\boldsymbol{u}}_{emf}^{k-1} + \boldsymbol{u}_d^{k-1} \right) \tag{4.50}$$

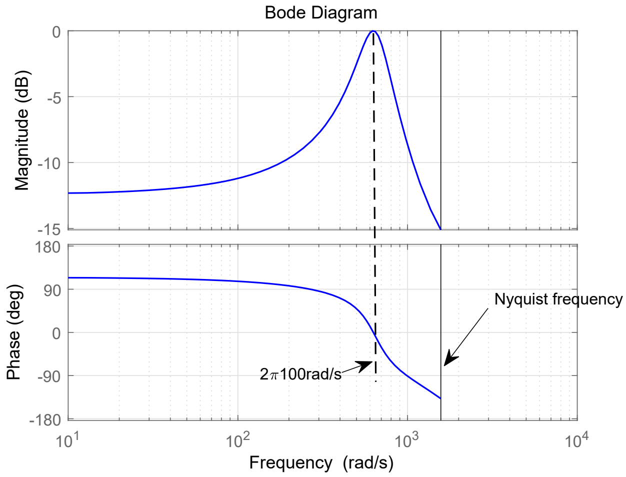

Fig. 4.6: Bode diagram of $F(z)$ at 100 Hz with $h = 0.25$.

Considering the actual disturbance $\boldsymbol{u}_d$ is unknown, the applied voltage can be computed with the estimated disturbance as

$$\left(\boldsymbol{u}_s^{k-1}\right)^{ref} = \left(\boldsymbol{u}_{s1}^{k-1}\right)^{ref} + \frac{\hat{R}_s}{1 - e^{-T_{sc}/\hat{\tau}}} \cdot \frac{e^{j\omega_e T_{sc}} - e^{-T_{sc}/\hat{\tau}}}{\hat{R}_s + j\omega_e \hat{L}_\sigma} \hat{\boldsymbol{u}}_d^{k-1} \tag{4.51}$$

where $\boldsymbol{u}_{s1}^{ref}$ was expressed in (4.44). When the above voltage is applied, the actual stator current at kth instant can be obtained as

$$\boldsymbol{i}_s^k = e^{-T_{sc}/\hat{\tau}} \boldsymbol{i}_s^{k-1} + \frac{1 - e^{-T_{sc}/\hat{\tau}}}{\hat{R}_s} \left(\boldsymbol{u}_s^{ref}\right)^{k-1} - \frac{e^{j\omega_e T_{sc}} - e^{-T_{sc}/\hat{\tau}}}{\hat{R}_s + j\omega_e \hat{L}_\sigma} \left(\hat{\boldsymbol{u}}_{emf}^{k-1} + \hat{\boldsymbol{u}}_d^{k-1}\right) \tag{4.52}$$

It is clear that if $\hat{\boldsymbol{u}}_d$ is not accurately estimated, there would be error between $\boldsymbol{i}_s^k$ and $\left(\boldsymbol{i}_s^k\right)^{ref}$. Considering (4.48), a sliding-mode disturbance adaptation scheme is developed as

$$\boldsymbol{e}_i^k = \left(\boldsymbol{i}_s^k\right)^{ref} - \boldsymbol{i}_s^k \tag{4.53}$$

$$\hat{\boldsymbol{u}}_d^k = \hat{\boldsymbol{u}}_d^{k-1} e^{j\omega_e T_{sc}} + \lambda Z\left(\boldsymbol{e}_i^k\right) \tag{4.54}$$

where $\lambda > 0$ is adaptation gain of the disturbance and $Z(\bullet)$ is a boundary switching function which is defined as

$$Z(\boldsymbol{e}_i) = \begin{cases} \frac{\boldsymbol{e}_i}{|\boldsymbol{e}_i|} & \text{if } |\boldsymbol{e}_i| > \sigma \\ \\ \boldsymbol{e}_i & \text{if } |\boldsymbol{e}_i| < \sigma \end{cases} \tag{4.55}$$

with σ as the boundary width. Subtracting (4.52) from (4.50) yields

$$\boldsymbol{e}_i(k) = \frac{e^{j\omega_e T_{sc}} - e^{-T_{sc}/\hat{\tau}}}{\hat{R}_s + j\omega_r \hat{L}_\sigma} \boldsymbol{e}_u(k-1) \tag{4.56}$$

where $\boldsymbol{e}_u^{k-1} = \boldsymbol{u}_d^{k-1} - \hat{\boldsymbol{u}}_d^{k-1}$ is the estimation error of disturbance. If λ is designed as

$$\lambda = h e^{j\omega_e T_{sc}} \frac{\hat{R}_s + j\omega_r \hat{L}_\sigma}{e^{j\omega_e T_{sc}} - e^{-T_{sc}/\hat{\tau}}} \tag{4.57}$$

the relationship between $\hat{\boldsymbol{u}}_d$ and $\boldsymbol{u}_d$ can be calculated based on (4.53)-(6.27) as

$$F(z) = \frac{\hat{\boldsymbol{u}}_d(z)}{\boldsymbol{u}_d(z)} = \frac{h e^{j\omega_e T_{sc}} z^{-1}}{1 - (1-h) e^{j\omega_e T_{sc}} z^{-1}} \tag{4.58}$$

To ensure stability of the disturbance estimation, h should be selected in the range of $0 < h < 2$. Noted that $F(z)$ is derived when the state variable stays within boundary width, i.e., $|\boldsymbol{e}_i| < \sigma$. It is clear that $F(e^{j\omega_e T_{sc}}) = 1$. Thus, the developed method can track the disturbance at fundamental frequency without magnitude error and phase delay, as also be confirmed by the bode plot in Fig. 4.6.

After obtaining the estimated disturbance $\hat{\boldsymbol{u}}_d^k$, it is used in (4.49) instead of unknown $\boldsymbol{u}_d^k$ to calculate the voltage reference. It should be noted that in practical application, there is one-step delay between the calculated voltage and the applied voltage. To compensate for the delay, (4.49) should be shifted forward by one step. The required stator current $\boldsymbol{i}_s^{k+1}$ and $\hat{\boldsymbol{u}}_d^{k+1}$ can be simply predicted by shifting (4.47) and (4.54) one-step ahead respectively. In conclusion, the procedure of the proposed discrete-time predictive current control is summarized as the following steps:

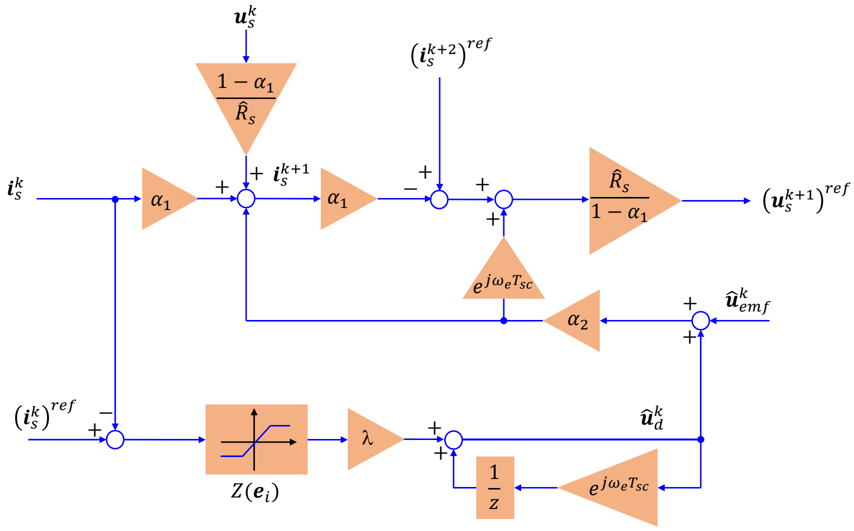

Fig. 4.7: Schematic diagram of the proposed DPCC.

1. Estimate disturbance voltage $\hat{\boldsymbol{u}}_d^k$ according to (4.53) and (4.54).

2. Predict $\boldsymbol{i}_s^{k+1}$ according to (4.47) based on the measured current i_s^k and the estimated $\hat{\boldsymbol{u}}_d^k$.

3. Calculate the reference voltage $\left(\boldsymbol{u}_s^{k+1}\right)^{ref}$ based on the step 1) and 2) by shifting (4.49) one-step ahead as

$$\left(\boldsymbol{u}_s^{k+1}\right)^{ref} = \frac{\hat{R}_s}{1-e^{-T_{sc}/\hat{\tau}}}\left\{\left(\boldsymbol{i}_s^{k+2}\right)^{ref} - e^{-T_{sc}/\hat{\tau}}\boldsymbol{i}_s^{k+1} + \right.$$
$$\left. + \frac{e^{j\omega_e T_{sc}} - e^{-T_{sc}/\hat{\tau}}}{\hat{R}_s + j\omega_r \hat{L}_\sigma}\left[\hat{\boldsymbol{u}}_e^{k+1} + \hat{\boldsymbol{u}}_d^{k+1}\right]\right\} \tag{4.59}$$

where $\left(\boldsymbol{i}_s^{k+2}\right)^{ref} = (i_d^{ref} + i_q^{ref})e^{j(\theta_r + 2\omega_e T_{sc})}$, $\hat{\boldsymbol{u}}_{emf}^{k+1} = j\omega_e \frac{L_m}{L_r}\psi_d e^{j(\theta_r+\omega_e T_{sc})}$ and $\hat{\boldsymbol{u}}_d^{k+1} = \hat{\boldsymbol{u}}_d^k e^{j\omega_e T_{sc}}$.

The schematic diagram of the whole algorithm is shown in Fig. 4.7. In the figure,

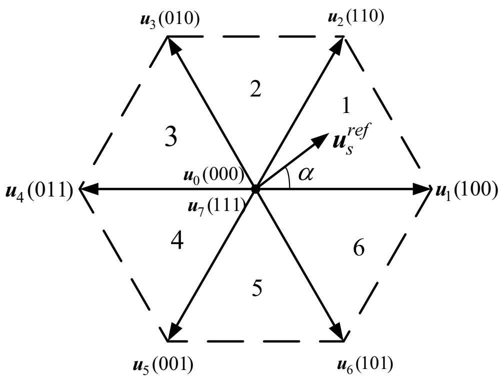

Fig. 4.8: Illustration of voltage vectors, switching states and 6 sectors for a two-level inverter.

the parameters α_1 and α_2 are expressed as follows

$$\alpha_1 = e^{-T_{sc}/\hat{\tau}} \tag{4.60}$$

$$\alpha_2 = \frac{e^{j\omega_e T_{sc}} - e^{-T_{sc}/\hat{\tau}}}{\hat{R}_s + j\omega_e \hat{L}_\sigma} \tag{4.61}$$

4.4 Closed-loop Control With Synchronized PWM Schemes

Under low pulse ratio operation, the conventional space vector modulation (SVM) or carrier based sinusoidal PWM (SPWM) presents significant current distortions including large low-order harmonics and sub-harmonics [137]. The harmonic components would lead to higher motor losses, larger torque ripples and poorer current control bandwidth, etc. To address this problem without increasing switching frequency of the inverter, a feasible method is to apply synchronized PWM schemes.

4.4.1 Hybrid Synchronized PWM Schemes

For a two-level inverter, there are two zero vectors and six different active vectors, dividing the complex plane into six sectors, as shown in Fig. 4.8. Generally, PWM schemes with higher pulse ratio N can produce better harmonic performance but higher switching losses. When the motor speed increases, the switching frequency increases accordingly when N is kept constant. Additionally, the inverter switching losses increase when the output power is increased. Hence, to reduce switching losses, pulse ratio should be decreased with higher motor speed and larger output power. For satisfying the requirements over the whole speed range, the hybrid PWM schemes with different pulse ratios are usually employed. In this study, the following PWM schemes, synchronous SVPWM with $N = 15, 3$ and basic bus clamping strategy-I (BBCS-I) PWM with $N = 11, 7$ are selected according to [139, 144]. For simplicity, they are named as SVPWM_15, SVPWM_3, BBCS_11 and BBCS_7 respectively in the following text. The vector sequences of these PWM schemes during sector 1 are listed in Table 4.1. More characteristics about these PWM schemes can be found in [139, 144, 176]. According to Table 4.1, two conditions should be satisfied to generate the desired pulse shapes. The first one is that the phase angle of voltage vector must equal the sampling positions defined in the second column. The second one is that the voltage vector at these sampling positions should be synthesized by the corresponding vector sequences as shown in the third column. The modulation index here is defined as

$$M^{ref} = \frac{\sqrt{3}u_s^{ref}}{U_{dc}} \tag{4.62}$$

The maximum value of M^{ref} is $2\sqrt{3}/\pi \approx 1.1027$ when inverter operates at six step mode.

Before these PWM methods are employed in the closed-loop control system, some issues must be solved. Firstly, the synchronization must be well kept in both steady and dynamic processes. Secondly, the smooth and fast transition between different

Table 4.1 : Synchronous PWM Schemes

P	Position of samples in sector 1	Vector Sequences in sector 1
15	6°, 18°, 30°, 42°, 54°	0127, 7210, 0127, 7210, 0127
11	6°, 18°, 30°, 42°, 54°	012, 210, 0127, 721, 127
7	10°, 30°, 50°	127, 7210, 012
3	30°	0127

PWM schemes should be achieved to avoid current/torque oscillations. Thirdly, the output fundamental voltage of the inverter must coincide with the reference voltage. Because the reference voltage is usually used in the observer to get the information of flux. Finally, stable and fast control of stator current should be guaranteed under low switching frequency operation. The following text will present some methods to cope with these problems. It is assumed in this study that both the current sampling and PWM updating instant are synchronized with the sampling position as shown in the second column of Table 4.1. This is based on the consideration that there is no switching transition at these sampling position and thus the current sampling would not be polluted by switching noise. Additionally, the selected PWM schemes are space vector based methods, the acquisition of fundamental current is permitted at the end of each subcycle [137]. This makes control of stator current without fundamental component estimation possible. Another benefit is that, as the current sampling is synchronized with PWM updating instant, it is easier to analyze and handle the modulation delay based on previous researches, such as [5, 63].

4.4.2 Synchronization Scheme

To maintain synchronization, two following steps are taken. The first step is to set a proper PWM updating frequency f_{pwm} to keep the pulse ratio constant over a speed range, which are $30f_e$, $30f_e$, $18f_e$ and $6f_e$ for SVPWM_15, BBCS_11, BBCS_7 and SVPWM_3 respectively. The second step is to match the PWM updating instant. During the steady state, the voltage vector rotates in the complex plane smoothly. Thus, if the first step is implemented, the increment of the angle of the voltage vector will always be the same. Take the SVPWM_15 as an example, if the starting position of the voltage vector is 6°, then the following phase angles of the voltage vector would be $6° + k \cdot 12°$ ($k = 1, 2, 3...$). However, in the closed-loop system, the phase angle of the voltage vector θ_u may vary sharply at any time, it is difficult to keep θ_u matching the sampling position shown in Table 4.1. To address this problem, the PWM interval set in the first step is compensated in a deadbeat fashion to correct the mismatch. Take SVPWM_15 as an example to clarify this point, the difference of the phase angle between θ_u and the sampling position shown in Table 4.1 is calculated at each starting instant of the PWM interval as

$$\theta_{err} = \theta^{ref} - \theta_u \tag{4.63}$$

Where $\theta_u = \text{angle}(\boldsymbol{u}_s)$ (degree), $\theta^{ref} = 12k + 6$, $k = \text{round}\left((\theta_u - 6)/12\right)$. It is clear that to cancel θ_{err}, the compensation of the time required is

$$T_{com} = \frac{\pi\theta_{err}}{180} \cdot \frac{1}{2\pi f_e} = \frac{\theta_{err}}{360 f_e} \tag{4.64}$$

After obtaining T_{com}, the PWM updating interval for SVPWM_15 is

$$T_{pwm} = \frac{1}{30 f_e} + T_{com} \tag{4.65}$$

For the synchronization of other PWM schemes, the same method is applied. As the compensation is performed in a deadbeat fashion, any mismatch will be corrected in one PWM interval. Thus keeping synchronization during fast dynamic process can be ensured.

4.4.3 Keeping Linearity between Reference and Output

With very low pulse ratio of 3, the relationship between actual modulation index of the invert output voltage and u_s^{ref} may be not linear. In this study, the compensation for linearity and overmodulation is investigated directly by analyzing PWM sequences. It is found that the gain compensation is required for SVPWM_3 and analytic solution is derived in order to avoid using lookup tables.

For space vector based PWM, the reference voltage vector in each sector can be synthesized by two adjacent active vectors $\boldsymbol{u}_x$ and $\boldsymbol{u}_y$, and one or two zero vectors, with their respective duty ratio calculated as

$$d_x = M^{ref} \cdot \sin(60° - \alpha) \tag{4.66}$$

$$d_y = M^{ref} \cdot \sin \alpha \tag{4.67}$$

$$d_0 = 1 - d_1 - d_2 \tag{4.68}$$

where α is the angle between $\boldsymbol{u}_s^{ref}$ and $\boldsymbol{u}_x$. Fig. 4.9 shows the pole voltage of SVPWM_3 in the range of $0° \sim 90°$ of the stator flux trajectory depicted in Fig. 4.10d. According to (4.66)-(4.68), the angle β can be obtained as

$$\beta = 30° \cdot \left\{1 - M^{ref}\right\}. \tag{4.69}$$

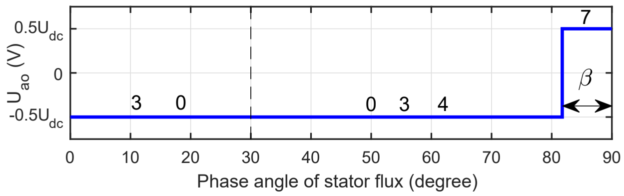

Fig. 4.9: Pole Voltage of phase 'a' and corresponding vector number for SVPWM_3.

Then, the output fundamental voltage can be expressed as [148]

$$U = \frac{2U_{dc}}{\pi}\left[1 - 2\sin\beta\right]$$

Thus, the actual output modulation index of the inverter voltage for SVPWM_3 is

$$M_3^{inv} = \frac{2\sqrt{3}}{\pi}\left[1 - 2\sin\beta\right]. \tag{4.70}$$

Based on (4.70), to make the M_3^{inv} equal to M^{ref}, the original M^{ref} in (4.69) should be modified as

$$M_{mod}^{ref} = \frac{30^\circ - \arcsin(0.5 - \sqrt{3}\pi M^{ref}/12)}{30^\circ}. \tag{4.71}$$

After the modulation index M^{ref} is obtained from the output of the current controller using (4.62), a modified virtual modulation index M_{mod}^{ref} should be calculated based on (4.71). Then, the duty ratio of each voltage vector can be calculated according to (4.66)-(4.68) using M_{mod}^{ref} instead of M^{ref}. It should be noted that as the deduction of (4.71) is directly based on mathematical analysis, it is precise for the whole range of M^{ref}, including over modulation.

Additionally, the original vector sequence in SVPWM_3 is modified and the sampling rate is increased to 18 times of the fundamental frequency to reduce time delay. Take the sector 1 as an example, the original vector sequence 0127 accounts for 60° as shown in Table 4.1 will be modified as 01, 12, 27 with each sequence accounts for

Table 4.2 : Modified scheme of SVPWM_3

P	Position of samples in sector 1	Vector Sequences in sector 1
3	10°, 30°, 50°	01, 12, 27

20°. After this modification, the whole vector sequence for every 60° is still the same as the original. But the sampling frequency can be improved to $18f_e$. This would bring some benefits to the current closed-loop control, such as lower sampling delay and higher controller bandwidth. The modified vector sequences are listed in Table 4.2. It should be noted that the duration of each voltage vector should be kept the same as the original to produce the same output. According to (4.68), the duration of zero vector can be calculated as

$$T_0 = \frac{1 - M_{mod}^{ref}}{6f_e}. \tag{4.72}$$

Considering that T_0 is divided equally for $\boldsymbol{u}_0$ and $\boldsymbol{u}_7$, the duration of the active vector $\boldsymbol{u}_1$ can be calculated as (4.73) when the sampling position of 10° is considered in this example.

$$T_1 = \frac{1}{18f_e} - 0.5T_0 = \frac{3M_{mod}^{ref} - 1}{36f_e} \tag{4.73}$$

The duration of an active vector combining with a zero vector at other sampling positions can be calculated in the same way. When the sampling position is 30°, 90°...330°, both active voltage vectors account for $1/(36f_e)$.

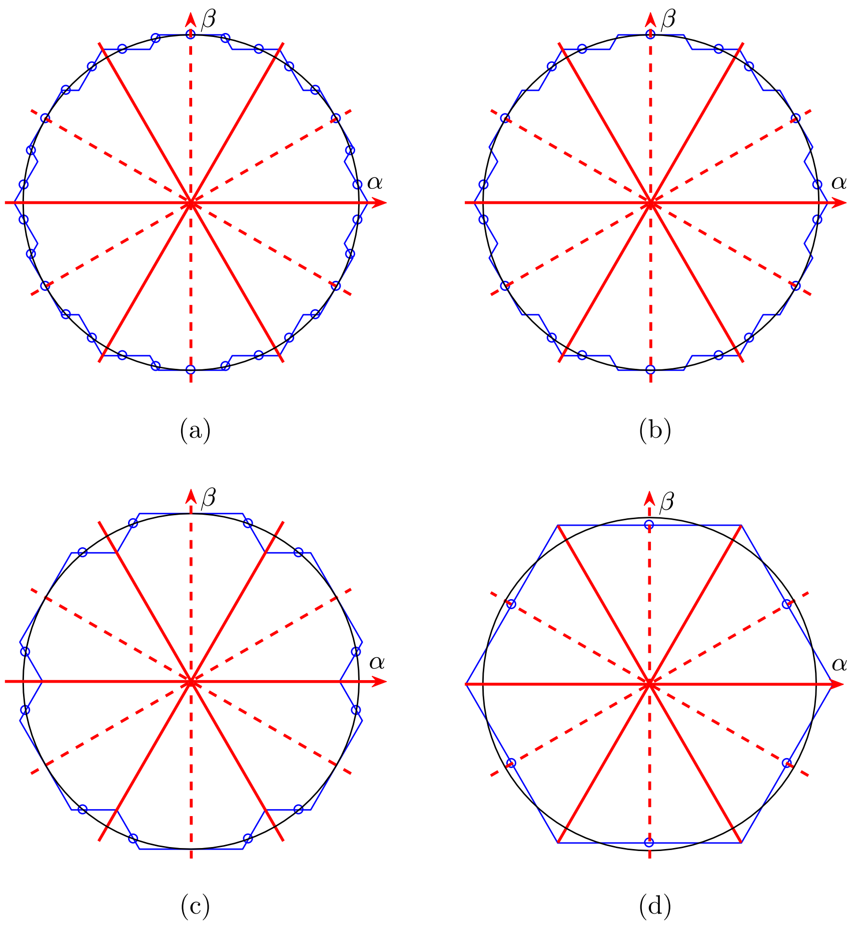

Fig. 4.10: Flux trajectories for (a) SVPWM_15, (b) BBCS_11, (c) BBCS_7 and (d) SVPWM_3.

4.4.4 Transition Strategy

As the current/flux trajectory of the PWM pattern is different from each other, the transition strategy should be carefully designed to avoid dynamic error which may cause torque oscillation and over-current event. In this study, the transition strategy is designed based on the analysis of flux trajectories of different PWM schemes. To achieve smooth transition, the original voltage reference will be compensated by a complex gain so that the end point of flux trajectory will be located on the new flux trajectory after the transition. As discontinuities of stator flux trajectory due to the transition between different PWM patterns is compensated using this method, there would be no dynamic error and thus the transition would be smooth and fast [177].

The flux trajectory can be obtained according to the vector sequence listed in Table 4.1 by integration, and they are shown in Fig. 4.10. The small circles in the figures indicating that there is a zero vector and the flux vector $\boldsymbol{\psi}_s$ is stationary at those positions until an active vector is applied.

Transition between conventional SVPWM and SVPWM_15

Transition between asynchronous SVPWM and SVPWM_15 is relatively easy. As both PWM schemes are traditional SVPWM, harmonic current is zero at the end of each subcycle. Thus, the transition can be started at the beginning of each PWM interval [168]. It should be noted that, though the phase angle of the voltage vector at the transition instant may be not the same as those listed in the Table 4.1 when transferring to SVPWM_15, the synchronization scheme described in Section 4.4.2 will help to setup the match with these positions and thus the symmetry of the output voltage can be well maintained.

Transition between SVPWM_15 and BBCS_11

It can be seen from Table 4.1 that the sampling position of BBCS_11 is the same as SVPWM_15, and there is only difference in the use of zero vectors for generating vector sequences. As the zero vector does not alter the flux vector, the flux trajectory of BBCS_11 should be the same as that of SVPWM_15. This can be clearly seen in Fig. 4.10. It is obvious that there are more zero vectors in SVWPM_15 and the

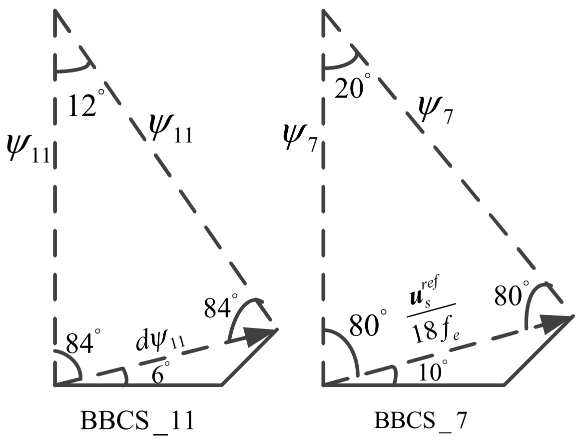

Fig. 4.11: Illustration of flux trajectories of BBCS_11 and BBCS_7 during one subcycle.

shapes of flux trajectory of SVPWM_15 and BBCS_11 are same. This indicates that the transition between SVPWM_15 and BBCS_11 can be started at any sampling position, because the flux trajectory coincides with each other. Hence, there is no dynamic error when the transition between SVPWM_15 and BBCS_11 happens.

Transition between BBCS_11 and BBCS_7

The stator flux vector rotates 12° and 20° for BBCS_11 and BBCS_7 during their respective subcycle. The Fig. 4.11 shows the flux trajectory in the subcycle of 270° $\sim$ 282° and 270° $\sim$ 290° for BBCS_11 and BBCS_7 respectively. The corresponding sampling positions of voltage are 6° and 10° respectively. Then, ψ_{11} in Fig. 4.11 can be simply calculated according to the law of sines as follows.

$$\frac{\psi_{11}}{\sin(84^\circ)} = \frac{d\psi_{11}}{\sin(12^\circ)} \tag{4.74}$$

The time of every subcyle of BBCS_11 is $1/(30f_e)$, thus $d\psi_{11}$ is

$$d\psi_{11} = \frac{\left|\boldsymbol{u}_s^{ref}\right|}{30f_e}. \tag{4.75}$$

where $|\bullet|$ represents the magnitude of the complex vector. Based on above two equations, ψ_{11} is obtained as

$$\psi_{11} = \frac{\sin(84^\circ)}{\sin(12^\circ)} \cdot \frac{\left|\boldsymbol{u}_s^{ref}\right|}{30 f_e}. \tag{4.76}$$

Similarly, ψ_7 can be deduced as

$$\psi_7 = \frac{\sin(80^\circ)}{\sin(20^\circ)} \cdot \frac{\left|\boldsymbol{u}_s^{ref}\right|}{18 f_e} \tag{4.77}$$

When a transition from BBCS_11 to BBCS_7 occurs, the original reference vector $\boldsymbol{u}_s^{ref}$ should be multiplied by a complex compensation gain $\boldsymbol{k}_{11\_7}$ to make the flux vector rotates from $\psi_{11} \cdot e^{j \cdot 270^\circ}$ to $\psi_7 \cdot e^{j \cdot 290^\circ}$ at the end of the transition. Thus, $\boldsymbol{k}_{11\_7}$ can be calculated as follows

$$\boldsymbol{k}_{11\_7} \cdot \boldsymbol{u}_s^{ref} = \left(\psi_7 \cdot e^{j \cdot 290^\circ} - \psi_{11} \cdot e^{j \cdot 270^\circ}\right) \cdot 18 f_e \tag{4.78}$$

As $\boldsymbol{u}_s^{ref} = \left|\boldsymbol{u}_s^{ref}\right| e^{j \cdot 6^\circ}$ in this subcyle for BBCS_11, $\boldsymbol{k}_{11\_7}$ can be obtained from (4.78) as

$$\boldsymbol{k}_{11\_7} = \left\{\frac{\sin(80^\circ)\cos(70^\circ)}{\sin(20^\circ)} - j \cdot A\right\} e^{-j \cdot 6^\circ} \tag{4.79}$$

$$A = \frac{0.6 \sin(84^\circ)}{\sin(12^\circ)} - \frac{\sin(80^\circ)\sin(70^\circ)}{\sin(20^\circ)} \tag{4.80}$$

It can be found that the expression of $\boldsymbol{k}_{11\_7}$ is somewhat complicated. Fortunately, it is a fixed value independent of any parameters. Thus an approximate numerical solution of $\boldsymbol{k}_{11\_7}$ can be calculated offline and used in practical application, which is

$$\boldsymbol{k}_{11\_7} \approx e^{j \cdot 3.47^\circ} \tag{4.81}$$

It turns out that the phase angle of $\boldsymbol{u}_s^{ref}$ should be compensated by 3.47° when transferring from BBCS_11 to BBCS_7 at the voltage vector sampling position of

$6°$. The conclusion is valid for all transitions beginning at $60° \cdot k - 54°$ ($k = 1, 2...6$). Thus, there are 6 points where the transition from BBCS_11 to BBCS_7 can be started with the proposed method.

Similarly, the transition from BBCS_7 to BBCS_11 can be started at sampling position $60° \cdot k - 50°$ ($k = 1, 2...6$) and the complex gain $\boldsymbol{k}_{7\_11}$ can be obtained as

$$\boldsymbol{k}_{7\_11} = \left\{ \frac{\sin(84°)\cos(78°)}{\sin(12°)} - j \cdot B \right\} e^{-j \cdot 10°}, \tag{4.82}$$

$$B = \frac{\sin(80°)}{0.6 \cdot \sin(20°)} - \frac{\sin(84°)\sin(78°)}{\sin(12°)}. \tag{4.83}$$

The approximate numerical solution of $\boldsymbol{k}_{7\_11}$ is calculated as follow.

$$\boldsymbol{k}_{7\_11} \approx e^{-j \cdot 3.11°} \tag{4.84}$$

From (4.84), $3.11°$ should be subtracted from the phase angle of $\boldsymbol{u}_s^{ref}$ when transferring from BBCS_7 to BBCS_11.

Transition between BBCS_7 and SVPWM_3

Fig. 4.12 shows the trajectories of flux vector in the range of $270° \sim 330°$ for BBCS_7 and SVPWM_3, covering the sampling positions of $10°, 30°$ and $50°$ as listed in Table 4.2. The θ in the figure represents the rotating angle of the flux vector within first subcyle. For SVPWM_3, it takes a time of $1/(6f_e)$ for stator flux rotates from $270°$ to $330°$. According to (4.62) and (4.71), the $d\psi_3$ in Fig. 4.12 can

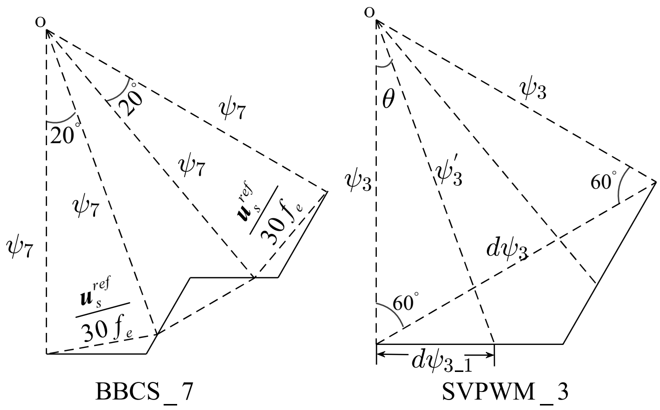

Fig. 4.12: Flux trajectories of BBCS_7 and SVPWM_3 during 270° ∼ 330°.

be calculated as follows.

$$
\begin{aligned}
d\psi_3 &= \left|\psi_3 e^{j330^\circ} - \psi_3 e^{j270^\circ}\right| \\
&= \frac{M_{mod}^{ref} \cdot U_{dc}}{\sqrt{3}} \cdot \frac{1}{6f_e} \\
&= \frac{M_{mod}^{ref}}{M^{ref}} \cdot \frac{\left|\boldsymbol{u}_s^{ref}\right|}{6f_e}
\end{aligned}
\tag{4.85}
$$

It can be found from Fig. 4.12 that ψ_3 is equal to $d\psi_3$. Hence, ψ_3 can be obtained as

$$\psi_3 = \frac{M_{mod}^{ref}}{M^{ref}} \cdot \frac{\left|\boldsymbol{u}_s^{ref}\right|}{6f_e}. \tag{4.86}$$

Based on (4.73), the $d\psi_{3\_1}$ in Fig. 4.12 can be deduced as

$$d\psi_{3\_1} = \frac{2}{3}U_{dc} \cdot T_1 = \frac{\sqrt{3}\left(3M_{mod}^{ref} - 1\right)}{M^{ref}} \frac{\left|\boldsymbol{u}_s^{ref}\right|}{54f_e}. \tag{4.87}$$

After obtaining ψ_3 and $d\psi_{3\_1}$, ψ_3' can be calculated as

$$\psi_3' = \sqrt{(\psi_3)^2 + (d\psi_{3\_1})^2} \tag{4.88}$$

And θ can be obtained as

$$\theta = \arctan(\frac{d\psi_{3\_1}}{\psi_3}) \tag{4.89}$$

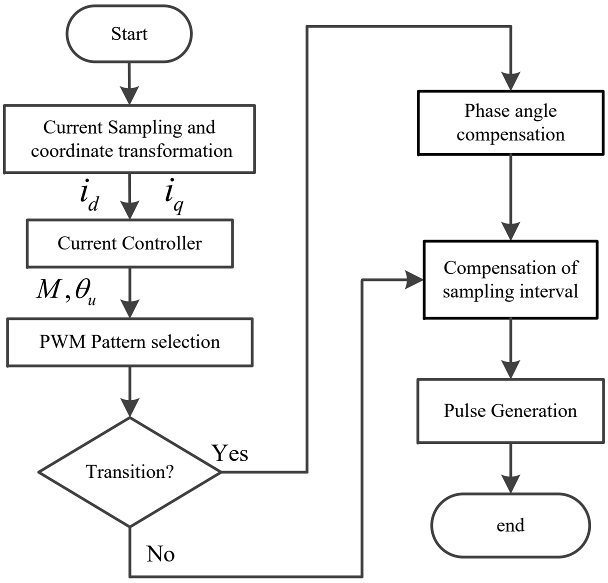

Fig. 4.13: Flowchart of applying synchronized PWM schemes in the closed-loop current control.

In this study, SVPWM_3 is employed when $M^{ref} > 1$. Namely that, the transition between BBCS_7 and SVPWM_3 would begin at $M^{ref} = 1$. As shown in Table 4.2, the sampling positions of the SVPWM_3 are the same as those of BBCS_7 after modification. Thus, if there is a position where the flux trajectories of two PWM schemes coincide with each other, the transition can be started and then the stator flux vector will follow the new one without error. To achieve this, the reference of voltage vector is first compensated by $\boldsymbol{k}_{7\_3}$ for BBCS_7 to cancel the error of flux vector and then the transition is started at the next sampling position. For example, if the transition begins at sampling position of 50°, the compensation stage should be performed at 30° . And, $\boldsymbol{k}_{7\_3}$ can be calculated as follows.

$$\frac{\boldsymbol{k}_{7\_3} \left| \boldsymbol{u}_s^{ref} \right| e^{j30^\circ}}{18 f_e} = \psi_3' e^{j(330^\circ - \theta)} - \psi_7 e^{j310^\circ} \tag{4.90}$$

Based on (4.77), (4.88) and (4.90), $\boldsymbol{k}_{7\_3}$ is obtained when $M^{ref} = 1$ as

$$\boldsymbol{k}_{7\_3} \approx e^{-j1.82^\circ}. \tag{4.91}$$

It is shown that only the phase angle of $\boldsymbol{u}_s^{ref}$ should be compensated by -1.82°. Then, the smooth transition from BBCS_7 to SVPWM_3 can be triggered at the next PWM interval. Due to the symmetry, the conclusion is valid for all transition at sampling position of $60^\circ k - 10^\circ$ ($k = 1, 2...6$). In summary, the phase angle of $\boldsymbol{u}_s^{ref}$ is first compensated by -1.82° at the sampling position $60^\circ k - 30^\circ$, then the output vector sequence is shifted from BBCS_7 to SVPWM_3 at the sampling position of $60^\circ k - 10^\circ$.

Similarly, the compensation gain of $\boldsymbol{k}_{3\_7}$ can be obtained as (4.92) when transferring from SVPWM_3 to BBCS_7 at the sampling position of $60^\circ k - 10^\circ$.

$$\boldsymbol{k}_{3\_7} \approx e^{j1.7^\circ} \tag{4.92}$$

Unlike other transition schemes, there are two steps for transferring from BBCS_7 to SVPWM_3, because the desired voltage vector can not be synthesized by the individual vector sequence shown in Table 4.2. As a result, the compensation has to be implemented in BBCS_7 before entering SVPWM_3.

It should be noted that the concept of flux trajectory here is only used for analysis, but not used in the control system. The flowchart of the proposed method is shown in Fig. 4.13.

Table 4.3 : Parameters of IMs Under Test

Rated power	P_N	2.2 kW	180 kW
DC-bus voltage	U_{dc}	550 V	550 V
Rated voltage	U_N	380 V	380 V
Rated frequency	f_N	50 Hz	68 Hz
Number of pole pairs	N_p	2	2
Stator resistance	R_s	1.76 Ω	0.0334 Ω
Rotor resistance	R_r	1.29 Ω	0.0147 Ω
Mutual inductance	L_m	0.158 H	0.0114 H
Stator inductance	L_s	0.170 H	0.0118 H
Rotor inductance	L_r	0.170 H	0.0118 H

4.5 Simulation and Experimental Results

To verify the effectiveness of the proposed methods, simulation tests and experimental tests were carried out on the two-level inverter fed IM drive platform. The motor parameters are listed in Table 4.3. Unless otherwise specified, the tests were made on the down-scaled 2.2 kW IM drive. The other results are obtained with the 180 kW IM drive. In experimental tests, the developed algorithms are implemented on a 32bit floating point DSP TMS320F28335. The internal variables are acquired via on-board DA converter. However, the waveform of stator current is directly obtained by the current probe. The experimental test rig with a 2.2 kW IM is shown in Fig. 4.14. All the data are sampled by a digital oscilloscope and then transferred

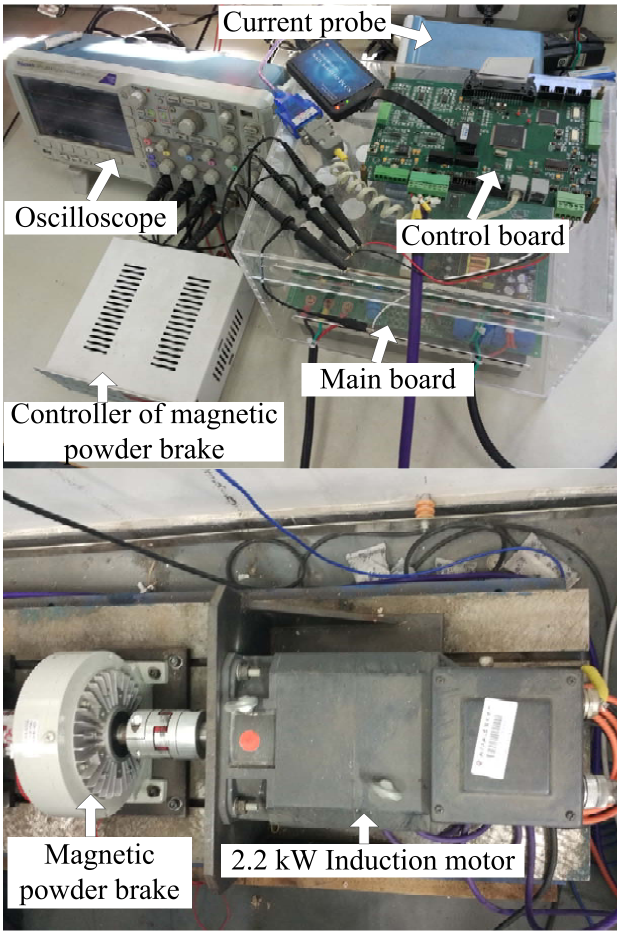

Fig. 4.14: Experimental setup.

to the PC for analysis and plotting.

4.5.1 Verification of Speed-sensorless Operation

The effectiveness of the proposed feedback gain matrix based AFO for speed estimation is firstly validated in this subsection with model predictive current control presented in [167].

Fig. 4.15 shows the responses of the AFO when the motor is started from a free-running speed 1200 rpm. It is seen that the estimated speed $\hat{\omega}_r$ converges to the actual speed quickly. There is no oscillation or inrush current during starting pro-

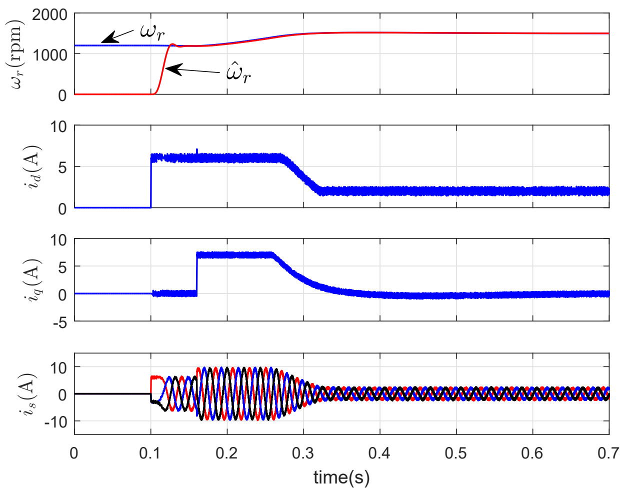

Fig. 4.15: Simulated responses of starting from 1200 rpm to 1500 rpm with the proposed method.

cess. After $\hat{\omega}_r$ reaches ω_r, the normal operation is enabled and the motor speed is accelerated to the reference speed 1500 rpm. When i_q decreases, i_d decreases accordingly. Hence, the efficiency can be improved during light load conditions. From the time the control system is activated to the time the speed control loop is enabled, the whole process takes less than 0.1 second. This test confirms that a free-running motor can be smoothly and quickly started without speed sensor using the proposed method.

To illustrate the effectiveness of the proposed feedback gain matrix (4.28), the same tests were carried out when the gain matrix are selected as zero and $\boldsymbol{G}_1$. With $\boldsymbol{G}_1$, the poles of the observer is proportional to the poles of IM itself [178].

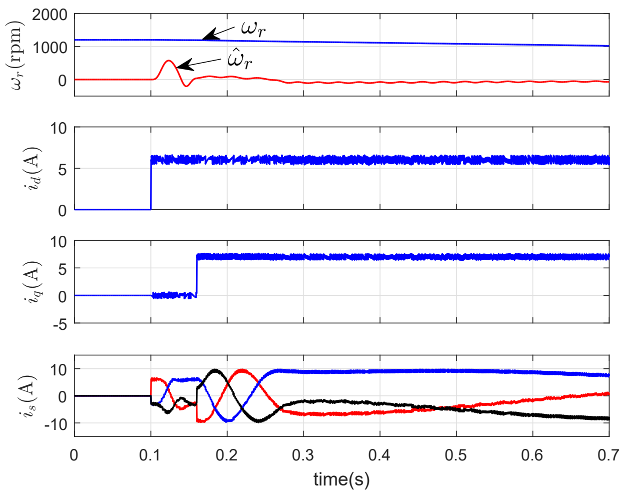

(a)

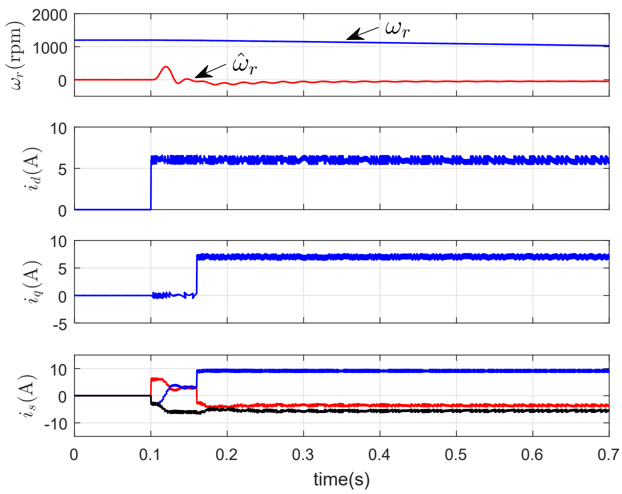

(b)

Fig. 4.16: Simulated responses of starting from 1200 rpm to 1500 rpm with (a) zero gain matrix and (b) $\boldsymbol{G}_1$.

$$\boldsymbol{G}_1 = \begin{bmatrix} f \\ \frac{\lambda L_r (k^2-1) R_s - f}{\lambda L_m} \end{bmatrix} \tag{4.93}$$

$$f = \lambda(k-1)(R_s L_r + R_r L_s) + j(1-k)\hat{\omega}_r \tag{4.94}$$

where, k is a proportional constant and it is set as $k = 1.2$ in the test. As can

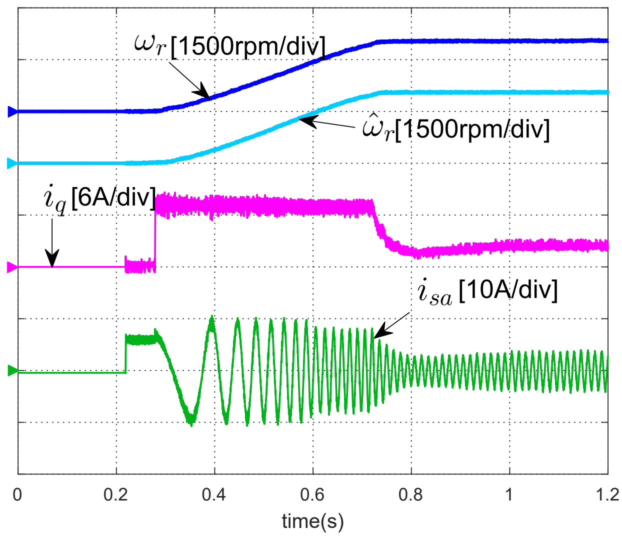

Fig. 4.17: Experimental results of starting from standstill to 2100 rpm with the proposed method.

be seen from Fig. 4.16, the estimated speed can not converge to the actual speed in both cases and start of the motor fails. Hence, the smooth and quick start of a free-running motor can only be achieved with the AFO based on the proposed gain matrix (4.28).

Fig. 4.17 shows the experimental results when the machine starts from standstill to 2100 rpm without load. The recorded curves from top to the bottom are actual speed, estimated speed, torque current i_q and one-phase stator current. It can be seen that the motor accelerates quickly to the reference speed after initial speed estimation. The estimated speed follows the actual speed well during the whole process, indicating that the AFO works well over a wide speed range.

The proposed AFO can help to start the motor not only from standstill but also from a rotating state. Fig. 4.18 shows the experimental results when the motor is started from free-running conditions. At the beginning, the motor is steadily rotating at

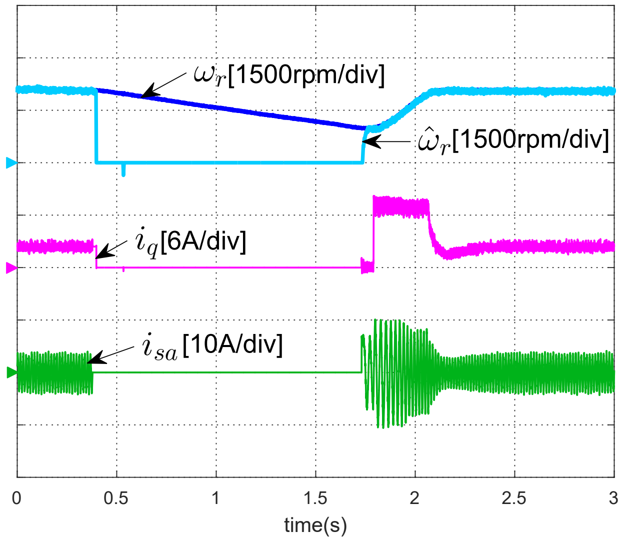

(a)

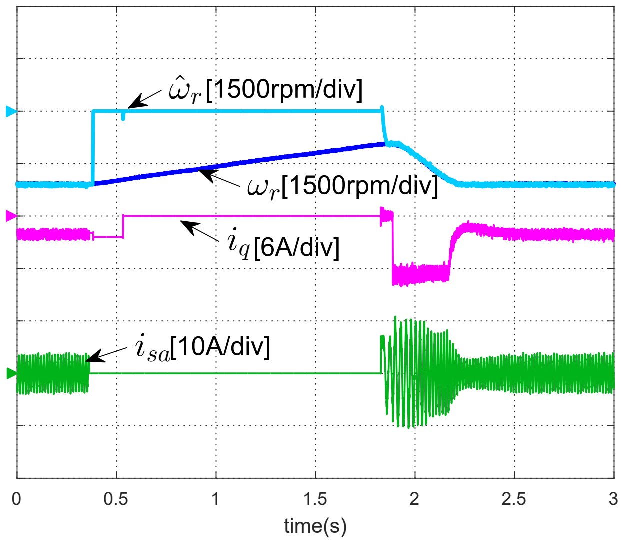

(b)

Fig. 4.18: Experimental results of starting from free-running state with (a) forward speed and (b) backward speed based on the proposed method.

2100 rpm and -2100 rpm as shown in Figs. 4.18a and 4.18b respectively. Then, the power is turned off and the rotor speed decreases gradually due to the friction load. After a moment, the PWM inverter is re-powered. For a direct comparison, the zero

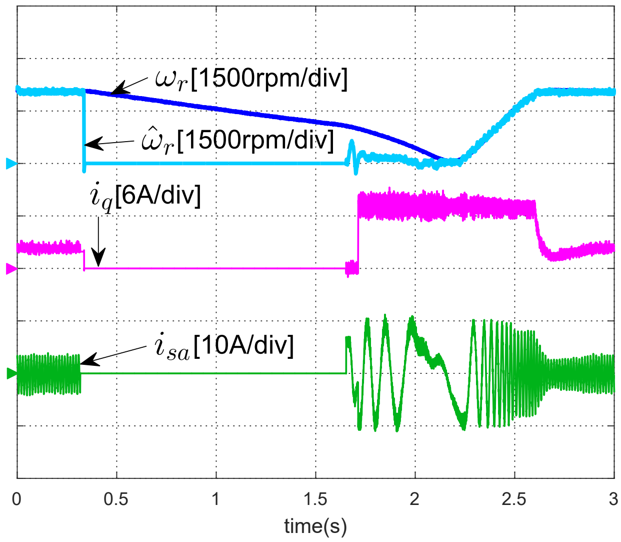

Fig. 4.19: Experimental results of starting from a high initial speed with zero feedback gain matrix.

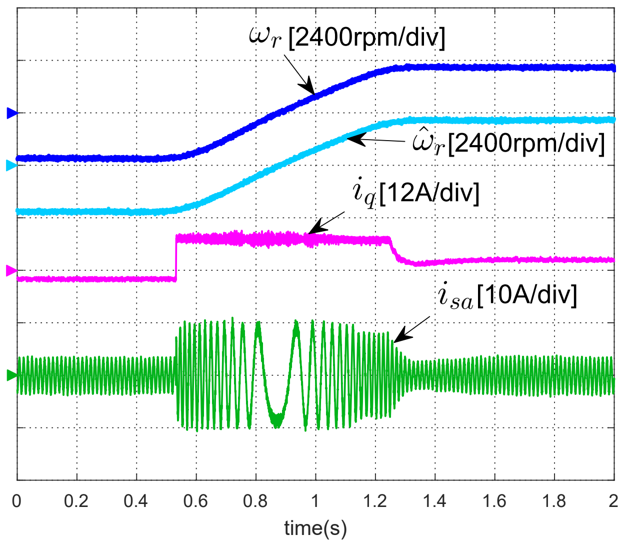

Fig. 4.20: Responses during speed reversal with the proposed AFO.

position of actual speed and estimated speed is set the same in this test. It is clear that, the estimated speed can respond for both rotational directions quickly.

No obvious oscillation and inrush current can be observed during starting process. After the estimation of initial speed, the rotor speed is quickly re-accelerated to the original reference. The estimated speed almost coincides with the actual speed, showing good accuracy during dynamic and steady operations.

However, if feedback gain matrix is set as zero, the estimated speed can not converge to the actual speed if the motor is initially running at a high speed, as shown in Fig. 4.19. It is seen that when the rotor speed decreases to a smaller value which is close to the estimated speed, the motor states can still be estimated and the motor can be precisely controlled again. However, if there is a large shaft inertia, it would be time consuming to wait for the motor to stop. While with the proposed gain matrix, the motor can be started without speed sensor even at a high rotating speed.

Fig. 4.20 shows speed reversal from -2100 rpm to 2100 rpm. The motor speed quickly decelerates to zero and then accelerates to the reference. The zero-crossing of speed is relatively smooth without obvious chattering. This test confirms satisfactory performance of the proposed AFO during dynamic processes with variable speed.

4.5.2 Test Results for the Digital Current Controller

First, the effectiveness of the gain k_d designed in (4.37) is verified by the test on a 180 kW IM with parameters listed in Table 4.3. Fig. 4.21 shows the simulated step responses of q-axis current i_q when the pulse ratio N is only 7. One can see that the transient response of i_q is fast and smooth without significant overshoot when applying the proposed k_d. Compared with the result in Fig. 4.21b, the other two tests indicate that employing smaller controller gain leads to a relatively slower

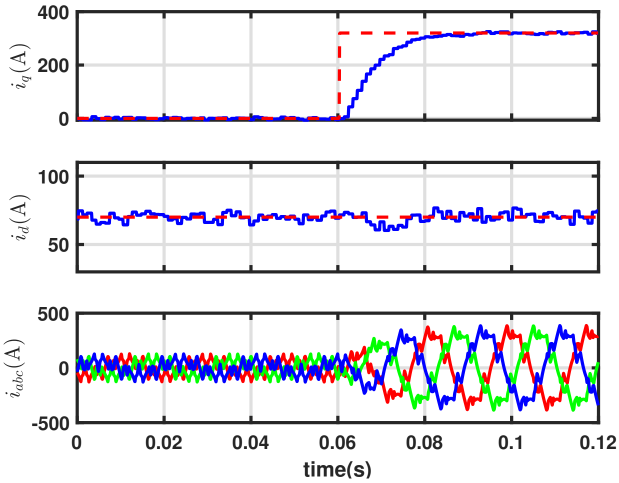

(a)

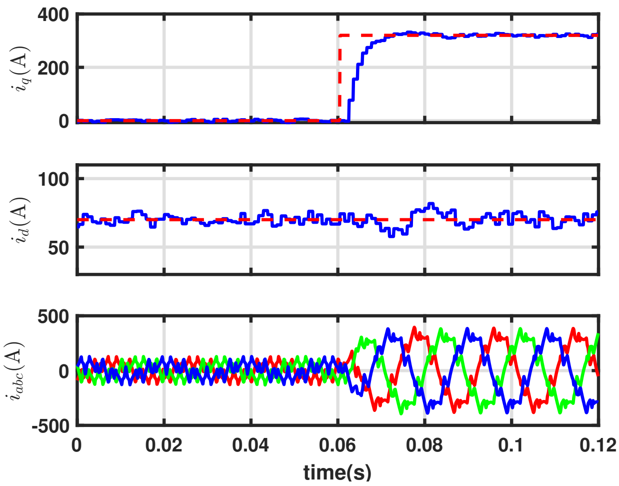

(b)

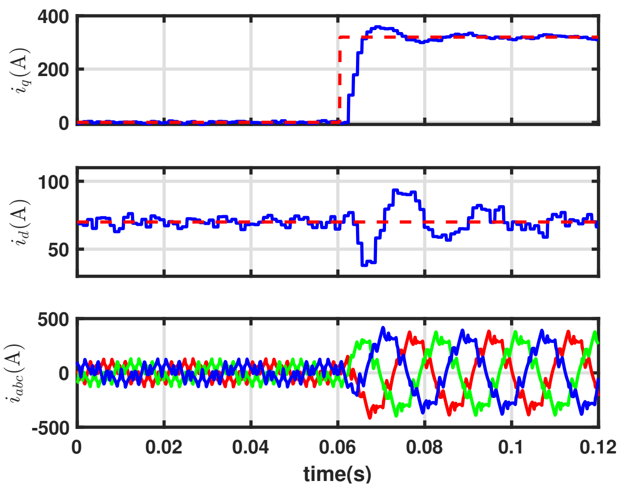

(c)

Fig. 4.21: Simulated step responses of i_q with (a) $0.5k_d$, (b) k_d and (c) $1.5k_d$ when $N = 7$.

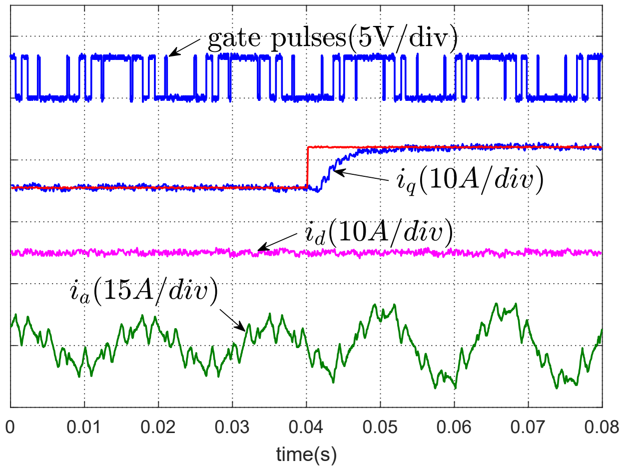

(a)

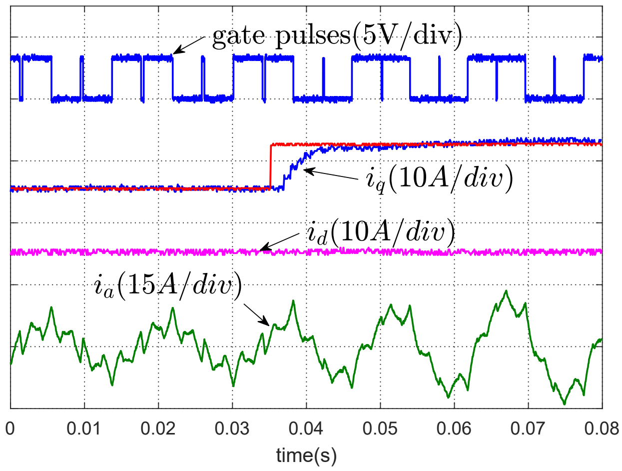

(b)

Fig. 4.22: Experimental results of i_q step responses when (a) $N = 7$ and (b) $N = 3$.

dynamic response while using a higher gain results in overshoot and significant oscillations. The test results justify the satisfactory overall performance of the current controller (4.33) with the designed k_d. Fig. 4.22 shows the experimental results from the down-scaled 2.2 kW IM drive when $N = 7$ and $N = 3$. The curves from top to bottom in two figures are A-phase gate pulses, i_q, i_d and A-phase current

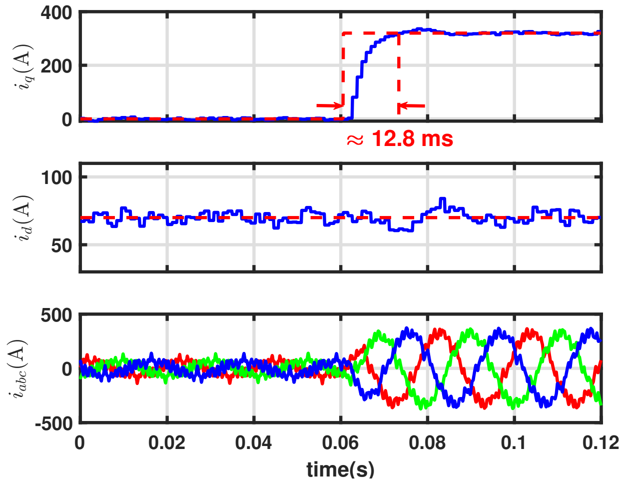

(a)

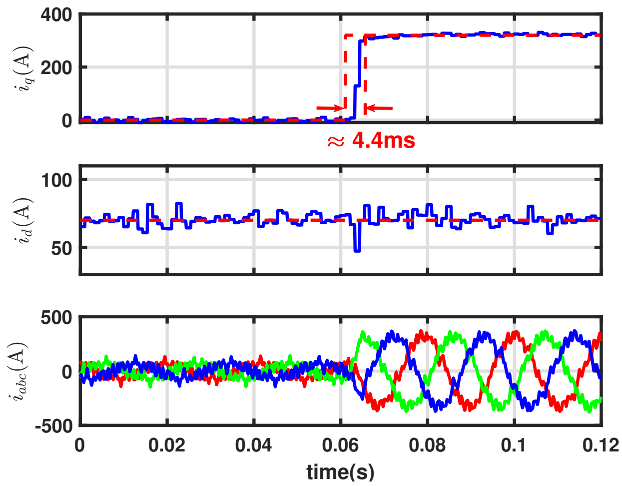

(b)

Fig. 4.23: Simulated i_q step responses of (a) the controller (4.33) [5] and (b) the proposed DPCC when $N = 10$.

respectively. It can be seen that i_q can track its reference quickly with low pulse ratio. These dynamic tests show that the whole regulation loop works well with the designed parameter even when the pulse ratio is as low as 3.

Then, the performance of the proposed DPCC introduced in Section 4.3.2 is validated. The i_q step responses of the proposed DPCC and the prior method [5] are

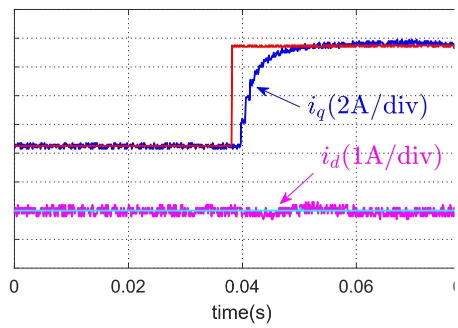

(a)

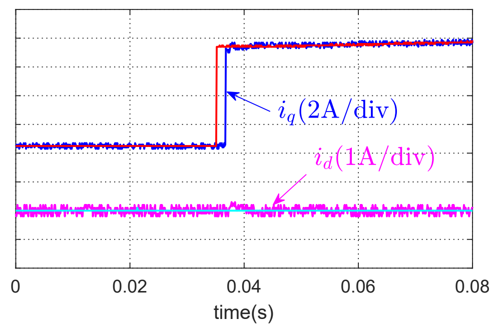

(b)

Fig. 4.24: Experimental results of i_q step responses for (a) the prior controller [5] and (b) the proposed DPCC.

simulated with the 180 kW IM drive and the results are shown in Fig. 4.23. It is seen that the actual q-axis current i_q can track its reference quickly during dynamic processes and there is no steady-state error during steady state for both methods. The settling time of the prior method and the proposed method is 12.8 ms and 4.4 ms respectively when the i_q^{ref} steps from zero to its rated value. Obviously, the proposed DPCC is superior with much faster transient response when compared with the existing method [5]. The experimental tests on the down-scaled 2.2 kW IM were also made to confirm the effectiveness of the proposed DPCC. One can see from Fig. 4.24 that the proposed DPCC shows very fast dynamic responses which can eliminate tracking error in two control steps. By comparison, the i_q takes much more time to reach its reference when the prior current controller is employed.

4.5.3 Validation of Synchronized PWM Schemes based-Current Control

Fig. 4.25 shows the responses during transition between different PWM schemes. Current and gate pulses plotted in these figures are directly measured by probe

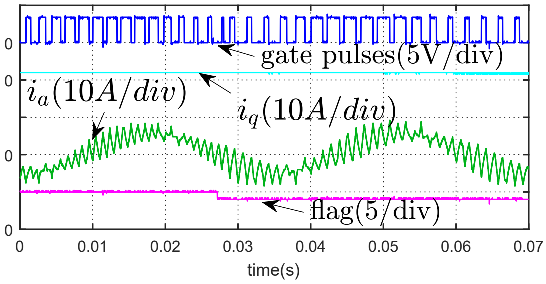

(a) Transition from conventional SVPWM to SVPWM_15.

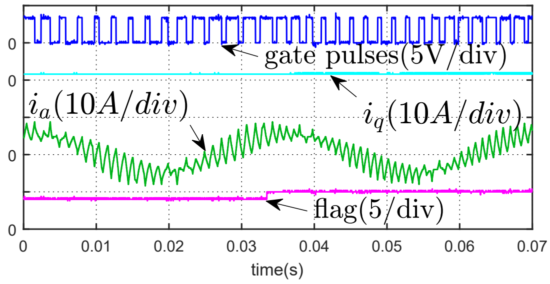

(b) Transition from SVPWM_15 to conventional SVPWM.

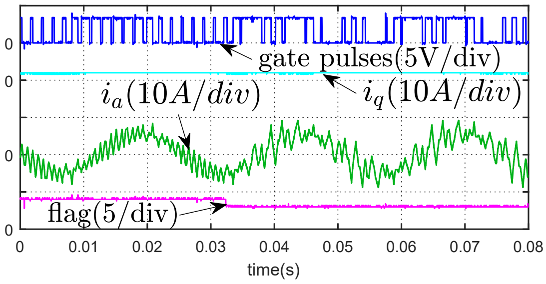

(c) Transition from SVPWM_15 to BBCS_11.

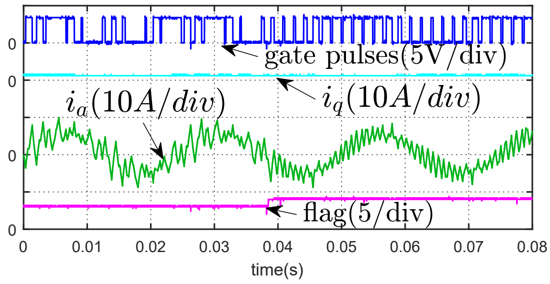

(d) Transition from BBCS_11 to SVPWM_15.

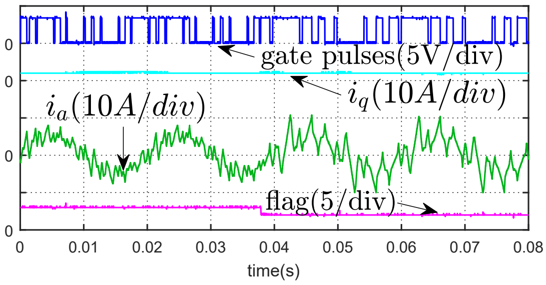

(e) Transition from BBCS_11 to BBCS_7.

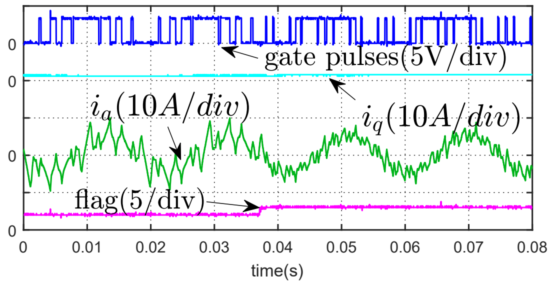

(f) Transition from BBCS_7 to BBCS_11.

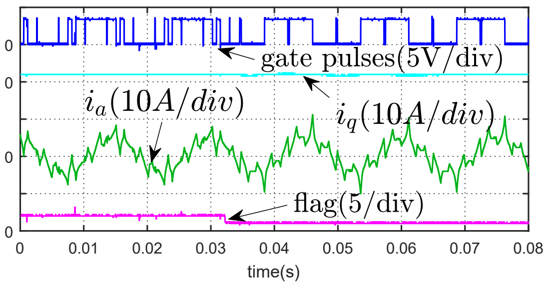

(g) Transition from BBCS_7 to SVPWM_3.

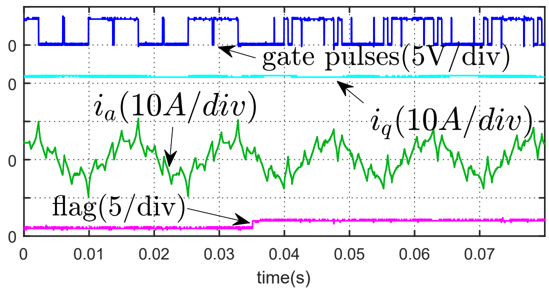

(h) Transition from SVPWM_3 to BBCS_7.

Fig. 4.25: Closed-loop test results of transition between different PWM schemes.

while the information of other variables are obtained via on-board DA converter. From top to bottom in each figure, the curves are a-phase gate pulses, i_q, a-phase current and variable $flag$ representing different PWM schemes. From results it can be seen that the symmetry of the gate pulse is well maintained for each synchronous PWM method and the transition is fast and smooth without inducing any obvious dynamic error.

Fig. 4.26 shows line voltages and corresponding weighted total harmonic distortion (WTHD) for different PWM strategies. WTHD is calculated as

$$U_{\text{WTHD}} = \frac{\sqrt{\sum (U_n/n)^2}}{U_1},\ n \neq 1. \tag{4.95}$$

where, U_1 and U_n are the root mean square values of the fundamental and nth harmonic voltages, respectively. It can be seen that the waveforms of line voltage are symmetry. There are no obvious sub-harmonics in line voltage and discrete nontriplen-odd-order harmonic components are distinctly identifiable, indicating that the pulse ratio is well synchronized with the operating speed.

As current deviation may be corrected by the closed-loop controller, the open loop test were also carried out, in order to clearly justify that the smooth transition can be achieved with only transition schemes. Fig. 4.27 shows the results during transition from BBCS_11 to BBCS_7. It is clear that there is a large current excursion during transition if the proposed method is not applied. This test confirms the effectiveness of the proposed method for achieving smooth transition.

Fig. 4.28 shows the dynamic performance when speed reference steps from 15 rpm to 1500 rpm. During the whole dynamic process, i_d is constant regardless of the

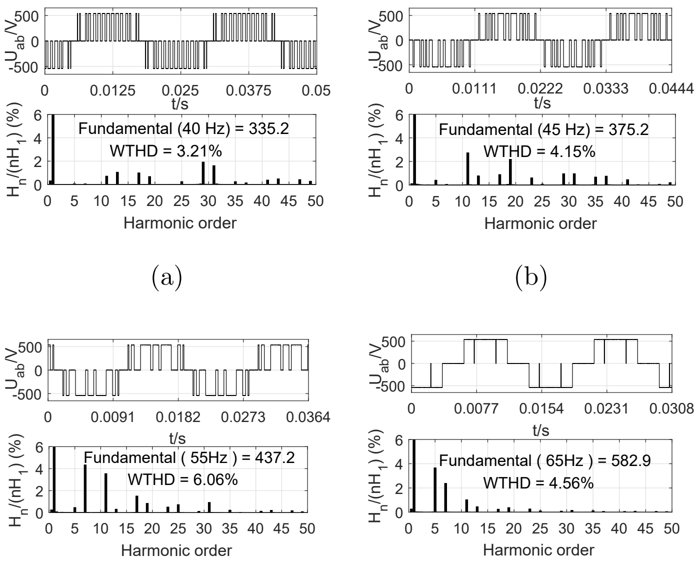

(a) (b)

(c) (d)

Fig. 4.26: Line voltage and corresponding WTHD for (a) SVPWM_15, (b) BBCS_11, (c) BBCS_7 and (d) SVPWM_3.

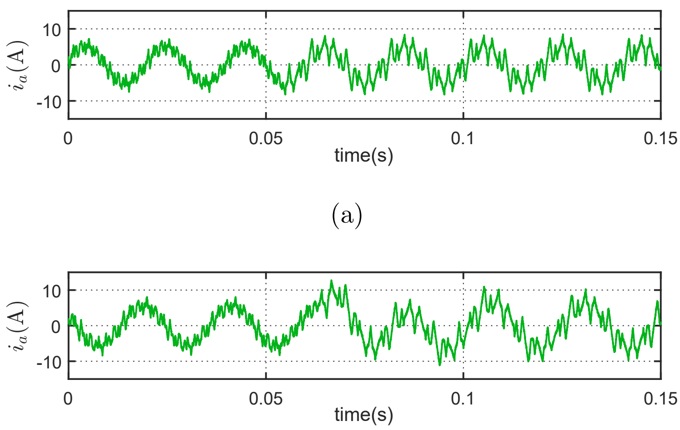

(a)

(b)

Fig. 4.27: Open loop test results of transition from BBCS_11 to BBCS_7 (a) with proposed method and (b) without proposed method.

variation of i_q, justifying that decoupling control of flux and torque is well achieved. It is also clear that the transitions between different PWM strategies are smooth

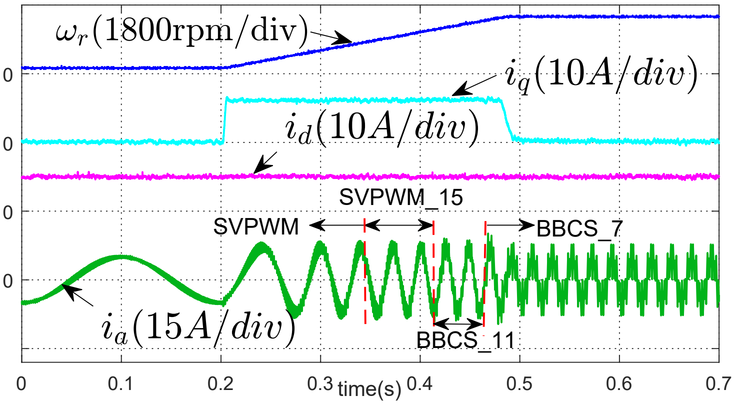

Fig. 4.28: Dynamic behavior of the machine with stepped speed command from 5 rpm to 1500 rpm.

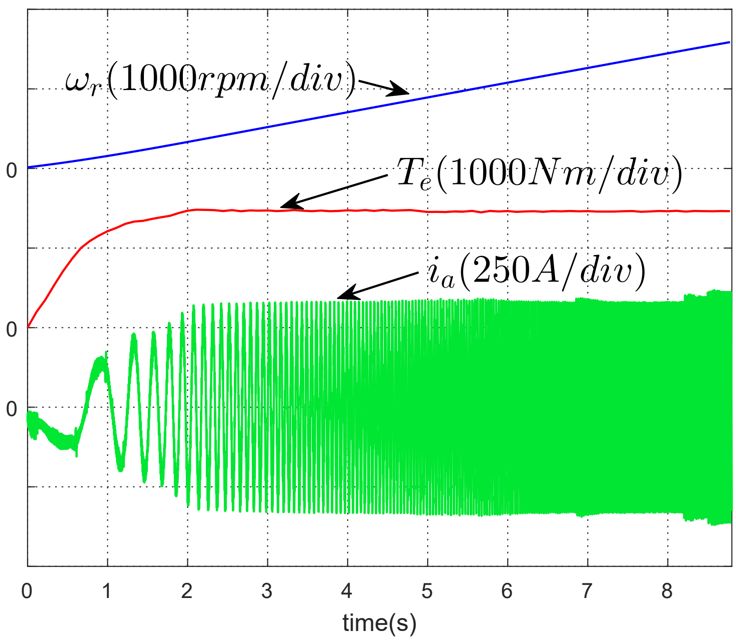

Fig. 4.29: Responses of starting from standstill. i_q^{ref} increases from zero to 160 A at the rate of 80 A/s.

without introducing any oscillation in i_d or i_q.

After the investigation on a down-scaled power testing platform, the proposed methods are implemented on the 180 kW IM drive. In the tests, speed and torque are sampled and transferred to the monitoring computer through serial communication every 0.1 second. The data of current is obtained through Yokogawa's DL850E scopecoder. Fig. 4.29 shows the responses of rotor speed, electromagnetic torque and phase current during motor acceleration. To avoid mechanical shock, i_q^{ref} gradually increases to 160 A within 2 seconds. It can be seen that the transition is smooth between different PWM schemes. The current and torque are well controlled during the whole process and there is no current/torque oscillation when pulse ratio/switching frequency jumps.

4.6 Summary

In this chapter, the speed-sensorless control, current regulation under low pulse ratio and the closed-loop control with synchronized PWM schemes are investigated for IM drives. Firstly, the convergence condition of speed estimation for adaptive full order observer was theoretically analyzed and then a feedback gain matrix was proposed to make the controller capable of starting a rotating motor with unknown rotational direction and initial speed. With the proposed method, motors rotating at a high speed can be smoothly and quickly started without the use of a speed sensor. Secondly, the proper gain design of a discrete time complex current controller was investigated to achieve a critically damped closed-loop system. However, the transient response of the complex current controller is relatively slow. Therefore, a discrete-time predictive current control was developed to improve the dynamic performance. In order to compensate for the side-impact of parameter mismatches, a sliding-mode disturbance observer was proposed to eliminate the steady-state tracking error. Thirdly, the implementation of closed-loop current control based on hybrid synchronous PWM schemes was introduced. A method by compensating phase angle of the voltage reference is deduced in detail to achieve fast and smooth transition between different PWM schemes. Additionally, the varying sampling rate with online correction was proposed to maintain symmetry of the output voltage pulses from the inverter during both dynamic and steady-state operation. The whole scheme is verified by simulation and experimental tests on both down-scaled and high power induction motor drive platforms. The obtained steady-state and dynamic responses validate the effectiveness of the proposed methods.

Chapter 5

Control of Permanent Magnet Synchronous Motor drives

5.1 Introduction

Permanent magnet synchronous motor (PMSM) drives have been widely used in the applications of traction, lathe, renewable energy, etc. owing to their excellent efficiency, satisfactory controllability, and good power density [112, 179–181]. For inverter-fed PMSM, the operation under low switching frequency to fundamental frequency ratio may occur for high power and high speed applications [182]. In the first case, switching frequency is usually restrained at a low value to reduce switching losses, while in the second case the rated speed of the motor is designed at a high value, e.g. to reduce motor volume [164, 182]. In both cases, the discretization effect cannot be ignored and must be carefully considered. Otherwise, deteriorated control performance or even instability could be observed [5, 63]. Hence, the conventional method, i.e., designing the current controller in the continuous-time domain with subsequent discretization for digital implementation can not guarantee the desired performance.

Part of this chapter has been pulished in [112, 136].

To improve the control performance with low pulse ratio, various current controllers have been proposed, such as complex-vector current controller [64, 67] , discrete-time current regulator [5, 65] and digital predictive current controller [166]. However, these methods are all designed for non-salient motors and thus not suitable for salient machines, e.g., interior permanent magnet synchronous motor (IPMSM) and synchronous reluctance motor [6, 103]. In [6], the discrete-time design principles presented in [5, 65] was extended to the machine with asymmetrical impedance. However, its performance at low speed operation is relatively poor [103]. To design discrete-time current controller, it is required to develop the discrete-time system model first. For IPMSM, the different values of dq-axis inductance make it more complex to design the regulator to realize the decoupled control of i_d and i_q with low pulse ratio. In [183], the concept of transfer matrix was employed to analyze and design the current controller for both salient/non-salient motors. However, all the theoretical analysis and controller design were carried out in the continuous-time domain. For digital implementation, a proper discretization algorithm is required, which increases complexity. Additionally, the performance at high-speed operation may be deteriorated [5]. The reference [172] introduces a discrete-time design methods for salient machine based on state-space description. However, the controller design requires computation of matrix exponential, which is complicated for analysis and implementation.

Traditionally, the current control of PMSM is implemented in the rotor flux oriented synchronous rotating reference frame, which requires rotor position for coordinate transformation. In practical applications, the installation of position sensor is usually inconvenient due to complex mechanical joint and higher cost. Additionally, the optical encoder, which is most widely used for high performance position/speed control is sensitive to the vibration, dust, etc. Therefore, the sensorless control methods have been drawn much attention and were intensively studied during last decades [104, 129, 134, 184]. Among various position estimators, sliding-mode observer (SMO) has attracted much attention due to its simplicity and satisfactory performance [106, 185]. The main issues of SMO in practical application include high frequency chattering and harmonic ripples in the estimated position caused by inverter nonlinearity and flux spatial harmonics, etc. To filter out harmonic components, low pass filter is usually implemented. This inevitably causes phase-delay in the disturbance estimation [136]. Apart from SMO, a low-frequency-ratio full order observer was proposed and verified in [186]. However, to ensure stable operation with low sampling frequency to fundamental frequency ratio, the expression of the observer is very complicated.

To ensure satisfactory current control performance, the mathematical model of PMSM is revised in this chapter to make it possible to extend the design principle of the discrete-time current controller to the salient machine. Unlike that shown in [6] which is only applicable in high-speed range, the proposed controller can achieve the decoupled control of dq-axis current components over the entire speed range in spite of the delay introduced by the digital implementation. Theoretical analysis and comparison with the prior art are presented to confirm the advantages of the proposed method.

In order to achieve position-sensorless operation, a position estimator is designed and analyzed in the discrete-time domain, which can ensure accurate position estimation under low switching frequency to fundamental frequency ratio. Normally, the conventional SMO cannot directly provide a smooth estimation due to high frequency chattering [111]. Thus filters are usually employed in practical application to suppress ripples in the conventional SMO [136]. For the proposed position estimator, theoretical study shows that a complex-coefficient filter is inherently incorporated, which can preserve fundamental components while suppressing harmonics. Hence, the position information can be accurately estimated without high frequency chattering or phase-delay during steady-state operation. Additionally, the designed position estimator can operate stably under low sampling frequency to fundamental frequency ratio. Simulation and experimental tests were presented to justify the effectiveness of the proposed method.

5.2 Discrete-time Current Controller for IPMSM

Unlike surface-mounted permanent magnet synchronous motor (SPMSM), the dq-axis inductances of IPMSM, i.e., L_d and L_q, are different. Thus, the current regulator presented in [5, 65] cannot be directly applied to control the current of an IPMSM. Defining the current $i_d^{'}$ and $i_q^{'}$ as $i_d^{'} = L_d i_d$ and $i_q^{'} = L_q i_q$, the mathematical model (2.16) can be rewritten as

$$\begin{bmatrix} \frac{di_d^{'}}{dt} \\ \frac{di_q^{'}}{dt} \end{bmatrix} = \begin{bmatrix} -\frac{R_s}{L_d} & \omega_e \\ -\omega_e & -\frac{R_s}{L_q} \end{bmatrix} \cdot \begin{bmatrix} i_d^{'} \\ i_q^{'} \end{bmatrix} + \begin{bmatrix} 1 & 0 \\ 0 & 1 \end{bmatrix} \cdot \begin{bmatrix} u_d \\ u_q \end{bmatrix} + \begin{bmatrix} 0 \\ -\omega_e \psi_{pm} \end{bmatrix} \tag{5.1}$$

It can be seen from (5.2) that the asymmetric cross-coupling term in original model becomes symmetric by defining new control variable $i_d^{'}$ and $i_q^{'}$. This facilitates the design of current controller as will be introduced in the following text. Equation (5.1) can be further expressed in the complex-vector form as

$$\frac{d\boldsymbol{i}'_{dq}}{dt} = -f_1\boldsymbol{i}'_{dq} - j\omega_e\boldsymbol{i}'_{dq} + \boldsymbol{u}_{dq} - \underbrace{\left(j\omega_e\psi_{pm} + \left(\boldsymbol{i}'_{dq}\right)^* f_2\right)}_{\boldsymbol{u}_{ed}} \tag{5.2}$$

where $f_1 = R_s\frac{L_d+L_q}{2L_dL_q}$, $f_2 = R_s\frac{L_q-L_d}{2L_dL_q}$ and $(\bullet)^*$ represent the conjugate complex variable. The discretized form of (5.2) can be obtained by solving the following equation

$$\boldsymbol{i}'^{,k+1}_{dq} = e^{-(f_1+j\omega_e)T_{sc}}\boldsymbol{i}'^{,k}_{dq} + \int_0^{T_{sc}} e^{-(f_1-j\omega_e)(T_{sc}-t)}\left(\boldsymbol{u}_{dq}(t) - \boldsymbol{u}_{ed}(t)\right)dt \tag{5.3}$$

According to (5.3) and considering $\boldsymbol{u}_{dq}(t) = \boldsymbol{u}^k_{dq}e^{-j\omega_e t}$, $\boldsymbol{u}_{ed}(t) = \boldsymbol{u}^k_e$, the discrete-time model can be obtained as [172]

$$\boldsymbol{i}'^{,k+1}_{dq} = e^{-(f_1+j\omega_e)T_{sc}}\boldsymbol{i}'^{,k}_{dq} + \frac{e^{-j\omega_e T_{sc}}\left(1-e^{-T_{sc}f_1}\right)}{f_1}\boldsymbol{u}^k_{dq} - \frac{1-e^{-(f_1+j\omega_e)T_{sc}}}{f_1+j\omega_e}\boldsymbol{u}^k_{ed} \tag{5.4}$$

It should be noted that only the fundamental component of $\boldsymbol{u}_{ed}$ is considered and the magnitude variation of $\boldsymbol{u}_{ed}$ is neglected when deriving (5.4).

5.2.1 Discrete-time Complex-vector PI Controller

After the model is revised, the principle introduced in [5] can be employed to design a discrete-time complex-vector PI controller. Take the $\boldsymbol{u}_{ed} = j\omega_e\psi_{pm} + \left(\boldsymbol{i}'_{dq}\right)^* f_2$ as the disturbance, the following discrete-time transfer function can be obtained

$$\frac{\boldsymbol{i}'_{dq}(z)}{\boldsymbol{u}_{dq}(z)} = \frac{1}{f_1}\frac{1-e^{-T_{sc}f_1}}{ze^{j\omega_e T_{sc}} - e^{-T_{sc}f_1}} \tag{5.5}$$

The digital delay in the synchronous reference frame is modeled as $z^{-1}e^{-j\omega_e T_{sc}}$. Then, the current controller can be obtained by zero/pole cancellation as [5]

$$G_c = k_c\frac{1-z^{-1}e^{-T_{sc}(j\omega_e+f_1)}}{1-z^{-1}}e^{2j\omega_e T_{sc}} \tag{5.6}$$

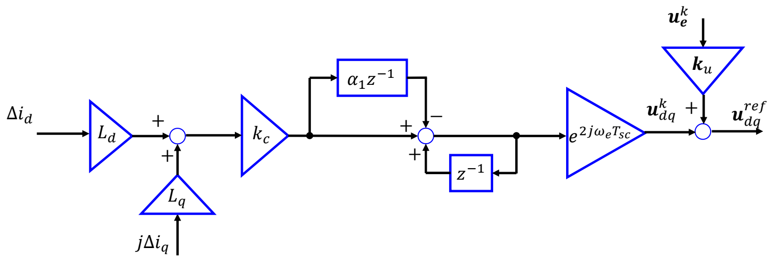

Fig. 5.1: Schematic diagram of the discrete-time current controller for IPMSM.

Fig. 5.1 shows the schematic diagram of the revised digital current controller which is suitable for IPMSM. It should be noted that the feedforward disturbance compensation should be compensated by $\boldsymbol{k}_u = \frac{2}{\omega_r T_{sc}}\sin(\frac{\omega_e T_{sc}}{2})e^{1.5j\omega_e T_{sc}}$ [63]. Unlike [6], in which the influence of the stator resistance is neglected, the proposed controller is constructed based on a more detailed model and thus works well not only in the high speed range but also in low and medium speed range. The difference from [5] is that the proposed digital current controller requires a simple pre-processing step, i.e., multiplying the d-axis current and q-axis current with the coefficient L_d and L_q respectively so that it is applicalbe for the salient machine.

5.2.2 Discrete-time Disturbance Observer based Predictive Current Control

Based on (5.4), the voltage that can force $\boldsymbol{i}_{dq}^{\prime,k+1}$ to reach its reference can be solved as

$$\boldsymbol{u}_{dq}^k = \frac{f_1 e^{j\omega_e T_{sc}}}{(1-e^{-T_{sc}f_1})}\left(\boldsymbol{i}_{dq}^{\prime,ref} - e^{-(f_1+j\omega_e)T_{sc}}\boldsymbol{i}_{dq}^{\prime,k} + \frac{1-e^{-(f_1+j\omega_e)T_{sc}}}{f_1+j\omega_e}\boldsymbol{u}_e^k\right) \tag{5.7}$$

However, the motor parameters may deviate from its nominal value during the operation due to saturation, temperature variation, etc. It is shown in [111, 112] that parameter mismatch would result in steady-state error in the reference tracking for predictive current control. Thus, the voltage computed in (5.7) cannot guarantee zero steady error in practical application. If there are parameter mismatches, (5.4) can be rewritten as [112]

$$\boldsymbol{i}_{dq}^{\prime,k+1} = e^{-(f_1+j\omega_e)T_{sc}}\boldsymbol{i}_{dq}^{\prime,k} + \frac{e^{-j\omega_e T_{sc}}(1-e^{-T_{sc}f_1})}{f_1}\boldsymbol{u}_{dq}^{k} - \frac{1-e^{-(f_1+j\omega_e)T_{sc}}}{f_1+j\omega_e}\left(\boldsymbol{u}_{ed}^{k} + \boldsymbol{d}_{p}^{k}\right) \tag{5.8}$$

where $\boldsymbol{d}_p^k$ is the disturbance resulted from parameter mismatches.

To eliminate the steady-state tracking error, a simple sliding-mode disturbance observer is developed as follows.

$$\Delta\boldsymbol{i}^{k} = \boldsymbol{i}_{dq}^{\prime,ref} - \boldsymbol{i}_{dq}^{\prime,k} \tag{5.9}$$

$$\hat{\boldsymbol{d}}_p^{k} = \hat{\boldsymbol{d}}_p^{k-1} + \lambda\frac{f_1+j\omega_e}{1-e^{-(f_1+j\omega_e)T_{sc}}}Z(\Delta\boldsymbol{i}^{k}) \tag{5.10}$$

where $\lambda > 0$ is adaptation gain of the disturbance and $Z(\bullet)$ is a boundary switching function which is defined as

$$Z(\Delta\boldsymbol{i}) = \begin{cases} \frac{\Delta\boldsymbol{i}}{|\Delta\boldsymbol{i}|} & \text{if } |\Delta\boldsymbol{i}| > \sigma \\ \\ \Delta\boldsymbol{i} & \text{if } |\Delta\boldsymbol{i}| < \sigma \end{cases} \tag{5.11}$$

With the estimated $\hat{\boldsymbol{d}}_p^k$, the voltage command can be calculated according to (5.8) as

$$\boldsymbol{u}_{dq}^{k} = \frac{f_1 e^{j\omega_e T_{sc}}}{(1-e^{-T_{sc}f_1})}\left(\boldsymbol{i}_{dq}^{\prime,ref} - e^{-(f_1+j\omega_e)T_{sc}}\boldsymbol{i}_{dq}^{\prime,k} + \frac{1-e^{-(f_1+j\omega_e)T_{sc}}}{f_1+j\omega_e}\left[\boldsymbol{u}_{e}^{k} + \hat{\boldsymbol{d}}_p^{k}\right]\right) \tag{5.12}$$

Substituting (5.12) into (5.8) yields

$$\Delta\boldsymbol{i}^{k+1} = \frac{1-e^{-(f_1+j\omega_e)T_{sc}}}{f_1+j\omega_e}\left(\boldsymbol{d}_p^{k} - \hat{\boldsymbol{d}}_p^{k}\right) \tag{5.13}$$

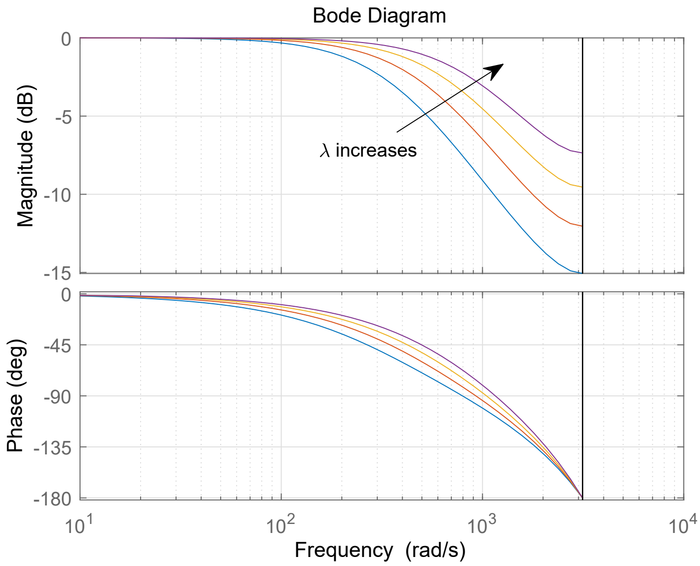

Fig. 5.2: Bode diagram of $\hat{\boldsymbol{d}}_p(z)/\boldsymbol{d}_p(z)$ with different λ.

Based on (5.10) and (5.13), the relationship between the estimated disturbance $\hat{\boldsymbol{d}}_p^k$ and its actual value $\boldsymbol{d}_p^k$ can be easily derived as

$$\frac{\hat{\boldsymbol{d}}_p(z)}{\boldsymbol{d}_p(z)} = \frac{\lambda}{z - (1 - \lambda)} \tag{5.14}$$

To ensure a stable estimation, λ should satisfy the following condition

$$0 < \lambda < 2 \tag{5.15}$$

It is seen from (5.14) that the estimated disturbance $\hat{\boldsymbol{d}}_p^k$ is its actual value passing through a low pass filter, as seen from Fig. 5.2. A larger λ results in faster dynamic response but also less noise immunity. Therefore, λ should be selected based on the trade-off between the dynamic and steady-state performance.

In practical application, there is usually one-step digital delay between the voltage command and the actual voltage. To compensate for the side-impact of the digital delay, the voltage $\boldsymbol{u}_{dq}^{k+1}$ should be calculated. The detailed implementation steps are summarized as follows.

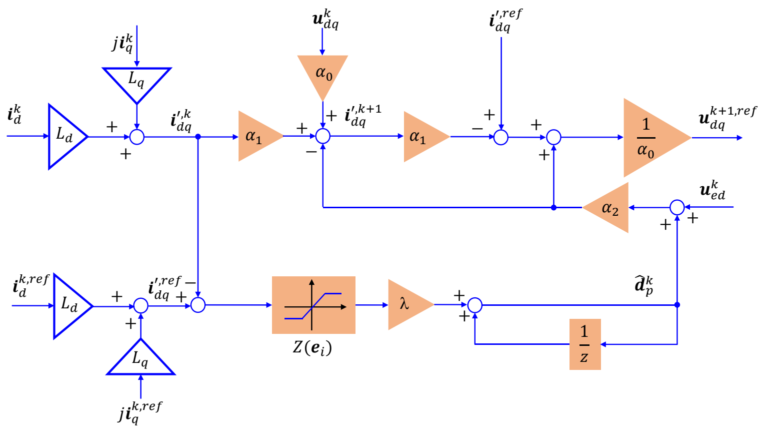

Fig. 5.3: Block diagram of the proposed discrete-time predictive current controller.

1. Calculate the disturbance $\hat{\boldsymbol{d}}_p^k$ based on (5.9) and (5.10);

2. Calculate $\boldsymbol{i}_{dq}^{\prime,k+1}$ based on (5.8) using the estimated disturbance and the voltage calculated in the last control period;

3. Calculate $\boldsymbol{u}_{dq}^{k+1}$ by shifting (5.12) one-step ahead as

$$\boldsymbol{u}_{dq}^{k+1} = \frac{f_1 e^{j\omega_e T_{sc}}}{(1-e^{-T_{sc}f_1})}\left(\boldsymbol{i}_{dq}^{\prime,ref} - e^{-(f_1+j\omega_e)T_{sc}}\boldsymbol{i}_{dq}^{\prime,k+1} + \frac{1-e^{-(f_1+j\omega_e)T_{sc}}}{f_1+j\omega_e}\left[\boldsymbol{u}_e^k + \hat{\boldsymbol{d}}_p^k\right]\right) \tag{5.16}$$

   It is assumed that $\boldsymbol{u}_e^{k+1} \approx \boldsymbol{u}_e^k$ and $\hat{\boldsymbol{d}}_p^{k+1} \approx \hat{\boldsymbol{d}}_p^k$ hold from kth instant to $(k+1)$th instant, which is usually reasonable because they are DC component during steady state. After the calculation of $\boldsymbol{u}_{dq}^{k+1}$, the voltage reference at the stationary reference frame can be finally computed as

$$\boldsymbol{u}_{\alpha\beta}^{k+1} = \boldsymbol{u}_{dq}^{k+1} e^{j(\theta_r^k+\omega_e T_{sc})} \tag{5.17}$$

The schematic diagram of the proposed disturbance observer based predictive current control is shown in Fig. 5.3. The detailed expressions of the coefficient $\alpha_{0,1,2}$

are listed as follows.

$$\begin{cases} \alpha_0 & = \frac{e^{-j\omega_e T_{sc}}(1-e^{-T_{sc}f_1})}{f_1} \\ \alpha_1 & = e^{-(f_1+j\omega_e)T_{sc}} \\ \alpha_2 & = \frac{1-e^{-(f_1+j\omega_e)T_{sc}}}{f_1+j\omega_e} \end{cases} \tag{5.18}$$

5.3 Discrete-time Position Estimator

5.3.1 Design of the discrete-time Position Estimator

In the prior research [104, 129, 134], the discrete-time PMSM model is usually obtained by applying the simple Euler method, which is not accurate under low sampling frequency ratio [186]. However, the detailed model shown in [175, 186] is somewhat complicated in practical application. In this section, a simple but accurate model will be developed and employed for designing the sliding-mode observer for position estimation.

The accurate discrete-time version of (3.13) can be derived as

$$\boldsymbol{i}_s^{k+1} = e^{-T_{sc}/\tau}\boldsymbol{i}_s^k + \frac{1-e^{-T_{sc}/\tau}}{R_s}\boldsymbol{u}_s^k - \underbrace{\frac{e^{j\omega_e T_{sc}} - e^{-T_{sc}/\tau}}{R_s\,(1+j\omega_e\tau)}}_{\boldsymbol{k}_E}\boldsymbol{E}^k \tag{5.19}$$

where $\tau = L_q/R_s$, $\boldsymbol{E}^k = d\psi_{ext}e^{j\theta_r}/dt$ is the EMF term and $\psi_{ext} = \psi_{pm} + (L_d - L_q)i_d$ is the extended flux. It can be seen from (5.19) that the coefficient $\boldsymbol{k}_E$ is a little complex. By applying the second-order Taylor series, $e^{j\omega_e T_{sc}} - e^{-T_{sc}/\tau}$ can be approximately expressed as

$$e^{j\omega_e T_{sc}} - e^{-T_{sc}/\tau} \approx \frac{T_{sc}}{\tau}(1+j\omega_e\tau) - \frac{T_{sc}^2}{\tau^2}(1+\omega_e^2\tau^2) \tag{5.20}$$

Substituting (5.20) into $\boldsymbol{k}_E$ yields

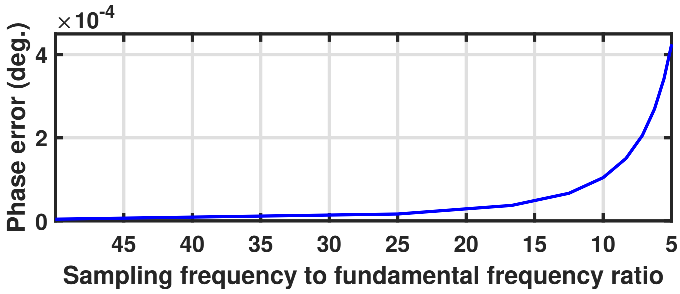

Fig. 5.4: Phase error introduced by simplifying $\boldsymbol{k}_E$.

$$\boldsymbol{k}_E \approx \frac{T_{sc}}{L_q}\left(1 - \frac{T_{sc}}{\tau} + j\omega_e \frac{T_{sc}}{2}\right) \approx \frac{T_{sc}}{L_q} e^{0.5j\omega_e T_{sc}} \tag{5.21}$$

Fig. 5.4 shows the phase angle difference between the simplified $\boldsymbol{k}_E$ (5.21) and its actual value under different sampling frequency to fundamental frequency ratio. It can be seen that the phase error resulted from the simplified $\boldsymbol{k}_E$ is no more than 5×10^{-4} degrees even when the pulse ratio decreases to 5. Therefore, utilizing the simplified $\boldsymbol{k}_E$ would not introduce significant phase error for rotor position estimation in practical application. With the simplified $\boldsymbol{k}_E$, (5.19) is rewritten as

$$\boldsymbol{i}_s^{k+1} = e^{-T_{sc}/\tau} \boldsymbol{i}_s^k + \frac{1 - e^{-T_{sc}/\tau}}{R_s} \boldsymbol{u}_s^k - \frac{T_{sc}}{L_q} e^{0.5j\omega_e T_{sc}} \boldsymbol{E}^k \tag{5.22}$$

Additionally, $\boldsymbol{E}^k$ can be calculated during steady state as

$$\boldsymbol{E}^k = e^{j\omega_e T_{sc}} \boldsymbol{E}^{k-1} \tag{5.23}$$

Based on (5.22) and (5.23), a discrete-time sliding mode observer is designed as

$$\hat{\boldsymbol{E}}^k = e^{j\omega_e T_{sc}} \hat{\boldsymbol{E}}^{k-1} + hT_{sc} \boldsymbol{u}_o^k \tag{5.24}$$

$$\hat{\boldsymbol{i}}_s^{k+1} = e^{-T_{sc}/\tau} \hat{\boldsymbol{i}}_s^k + \frac{1 - e^{-T_{sc}/\tau}}{R_s} \left(\boldsymbol{u}_s^k - \boldsymbol{u}_o^k\right) - \frac{T_{sc}}{L_q} e^{0.5j\omega_e T_{sc}} \hat{\boldsymbol{E}}^k \tag{5.25}$$

where $h > 0$ is a gain and $\boldsymbol{u}_o$ is the control function. Subtracting (5.22) from (5.25)

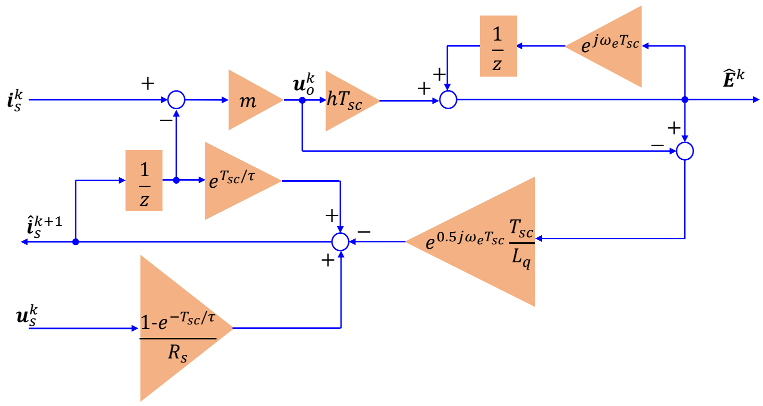

Fig. 5.5: Block diagram of the proposed discrete-time observer.

yields

$$\Delta \boldsymbol{i}^{k+1} = e^{-T_{sc}/\tau}\Delta \boldsymbol{i}^k - \frac{T_{sc}}{L_q}e^{0.5j\omega_e T_{sc}}\Delta E^k - \frac{1-e^{-T_{sc}/\tau}}{R_s}\boldsymbol{u}_o^k \tag{5.26}$$

where $\Delta \boldsymbol{i} = \hat{\boldsymbol{i}}_s - \boldsymbol{i}_s$, $\Delta E = \hat{\boldsymbol{E}} - \boldsymbol{E}$ are estimation errors. Setting the estimation error decays exponentially, i.e.,

$$\Delta \boldsymbol{i}^{k+1} = (1 - gT_{sc})e^{j\omega_e T_{sc}}\Delta \boldsymbol{i}^k \tag{5.27}$$

where $g > 0$ is a parameter needs to be designed. Moreover, taking unknown $\Delta \boldsymbol{E}^k$ as the disturbance, the control function $\boldsymbol{u}_o^k$ can be derived from (5.26) as

$$\boldsymbol{u}_o^k = \frac{R_s}{1-e^{-T_{sc}/\tau}}\left(e^{-T_{sc}/\tau} - (1-gT_{sc})e^{j\omega_e T_{sc}}\right)\Delta \boldsymbol{i}^k \tag{5.28}$$

With the developed $\boldsymbol{u}_o^k$, the EMF term $\hat{\boldsymbol{E}}^k$ can be accurately estimated based on (5.24) and (5.25). Considering $\hat{\boldsymbol{E}}^k = j\omega_e\psi_{pm}e^{j\theta_r^k}$ during steady state, the rotor position θ_r^k can be estimated as

$$\hat{\theta}_r^k = \text{angle}(\hat{\boldsymbol{E}}^k) - \text{sgn}(\omega_e)\frac{\pi}{2} \tag{5.29}$$

where angle$(\hat{\boldsymbol{E}}^k)$ represents phase angle of $\hat{\boldsymbol{E}}^k$ and sgn() represents sign function. The block diagram of the proposed position estimator is shown in Fig. 5.5. In the figure, the detailed expression of m is $m = g + (e^{-T_{sc}/\tau} - 1)/T_{sc}$. Due to the inherent filtering capacity, the high-frequency ripples can be effectively suppressed in the estimated $\hat{\boldsymbol{E}}^k$, which will be validated in the next section. Hence, the position $\hat{\theta}_r^k$ can be directly calculated as (5.29) without necessity of employing a phase-locked loop.

5.3.2 Analysis of the Position Estimator

Submitting $\boldsymbol{u}_o^k$ into (5.26) results in

$$\Delta \boldsymbol{i}^{k+1} = (1 - gT_{sc})e^{j\omega_e T_{sc}} \Delta \boldsymbol{i}^k - \frac{T_{sc}}{L_q} e^{0.5j\omega_e T_{sc}} \Delta \boldsymbol{E}^k \tag{5.30}$$

According to (5.30), the following transfer function can be obtained.

$$F_1(z) = \frac{\Delta \boldsymbol{i}(z)}{\Delta \boldsymbol{E}(z)} = -\frac{T_{sc} e^{0.5j\omega_e T_{sc}}}{L_q} \frac{1}{z - (1 - gT_{sc})e^{j\omega_e T_{sc}}} \tag{5.31}$$

To ensure stability, the pole $p = 1 - gT_{sc}$ must satisfy the requirement of $|P| < 1$, i.e.,

$$0 < g < \frac{2}{T_{sc}} \tag{5.32}$$

According to (5.28) and (5.31), the relationship between $\boldsymbol{u}_o$ and $\Delta \boldsymbol{E}$ can be derived as

$$F_2(z) = \frac{\boldsymbol{u}_o(z)}{\Delta \boldsymbol{E}(z)} = -\frac{T_{sc} R_s e^{0.5j\omega_e T_{sc}}}{L_q(1 - e^{-T_{sc}/\tau})} \frac{e^{-T_{sc}/\tau} - (1 - gT_{sc})e^{j\omega_e T_{sc}}}{z - (1 - gT_{sc})e^{j\omega_e T_{sc}}} \tag{5.33}$$

Additionally, the relationship between $\hat{\boldsymbol{E}}$ and $\boldsymbol{u}_o$ can be obtained from (5.24) as

$$\hat{\boldsymbol{E}}(z) = \frac{hT_{sc}}{1 - e^{j\omega_e T_{sc}} z^{-1}} \boldsymbol{u}_o(z) \tag{5.34}$$

Setting the parameter h as

$$h = \frac{\omega_c L_q (1 - e^{-T_{sc}/\tau}) g e^{j\omega_e T_{sc}}}{\left(e^{-T_{sc}/\tau} - (1 - gT_{sc})e^{j\omega_e T_{sc}}\right) R_s e^{0.5j\omega_e T_{sc}}} \approx \frac{\omega_c g T_{sc} e^{0.5j\omega_e T_{sc}}}{\left(e^{-T_{sc}/\tau} - (1 - gT_{sc})e^{j\omega_e T_{sc}}\right)} \tag{5.35}$$

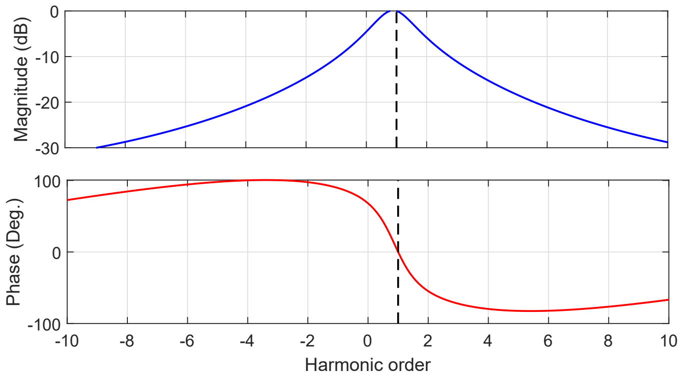

Fig. 5.6: Frequency-magnitude responses of $F_3(z)$.

the term $h\boldsymbol{u}_o$ can be simplified as

$$h\boldsymbol{u}_o(z) = \frac{-\omega_c g T_{sc} e^{j\omega_e T_{sc}}}{z - (1 - gT_{sc})e^{j\omega_e T_{sc}}} \Delta \boldsymbol{E}(z) \tag{5.36}$$

where $\omega_c > 0$ is a parameter. Based on (5.34) and (5.36), the following transfer function can be obtained.

$$F_3(z) = \frac{\hat{\boldsymbol{E}}(z)}{\boldsymbol{E}(z)} = \frac{g\omega_c T_{sc}^2 e^{j\omega_e T_{sc}}}{1 + g\omega_c T_{sc}^2 e^{j\omega_e T_{sc}} + e^{j\omega_e T_{sc}}(gT_{sc} - 2)z^{-1} - e^{2j\omega_e T_{sc}}(gT_{sc} - 1)z^{-2}} \tag{5.37}$$

From (5.37), it can be found that $F_3(e^{j\omega_e T_{sc}}) = 1$, indicating that the proposed method can estimate fundamental component of the concerned EMF term $\boldsymbol{E}$ without magnitude or phase error. Additionally, the frequency-magnitude responses as shown in Fig. 5.6 justify that the proposed method can maintain the fundamental component while suppressing the undesired harmonics.

5.4 Simulation and Experimental Results

Both simulation and experimental tests were carried out to verify the effectiveness

Table 5.1 : Parameters of PMSMs Under Test

Rated power	P_N	2.2 kW	150 kW
Rated frequency	f_N	100 Hz	300 Hz
Number of pole pairs	N_p	4	4
Stator resistance	R_s	2.58 Ω	0.015 Ω
d-axis inductance	L_d	28.1 mH	0.19 mH
q-axis inductance	L_q	42.5 mH	0.58 mH
Flux linkage	ψ_{pm}	0.38 Wb	0.092 Wb

of the proposed methods. The motor parameters are listed in Table 5.1. The simulation tests are performed on a 150 kW IPMSM drive. However, the experimental tests were made on a down-scaled 2 kW IPMSM drive due to the limitation of the test-rig in the laboratory. In practical tests, the developed algorithms are implemented on a 32bit floating point DSP TMS320F28335. The implemented control algorithm can be easily applied for a high-power IPMSM drive but just changing motor parameters. The internal variables are acquired via on-board DA converter. However, the waveform of stator current is directly obtained by the current probe. All the data are sampled by a digital oscilloscope and then transferred to the PC for analysis and plotting. Fig. 2.3 shows the block diagram of the vector control for the PMSM drives. To improve the efficiency, the look-up tables are used to generate current commands to achieve maximum torque per ampere (MTPA) control.

5.4.1 Test Results for the Designed Current Controller

For simplicity, the discrete-time complex-vector PI controller in Section 5.2.1 and disturbance observer based predictive current controller in Section 5.2.2 are named as DT-CVPI and DO-PCC respectively in the following text.

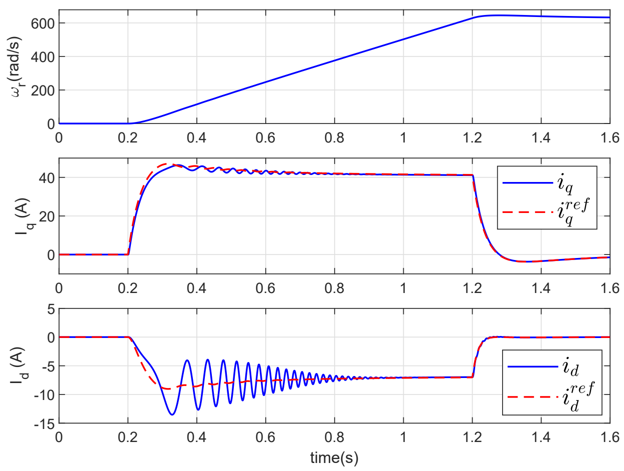

(a)

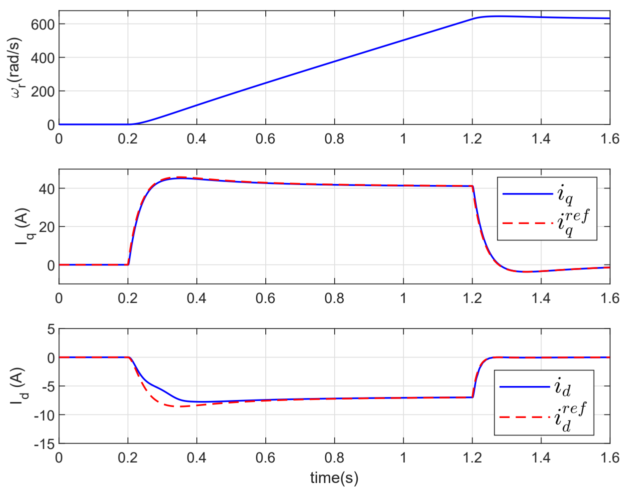

(b)

Fig. 5.7: Simulated dynamic responses of (a) the existing current controller [6] and (b) DT-CVPI with 2 kHz sampling frequency when the motor starts from standstill to 100 Hz.

Fig. 5.7 shows the simulated response of the prior current controller [6] and the

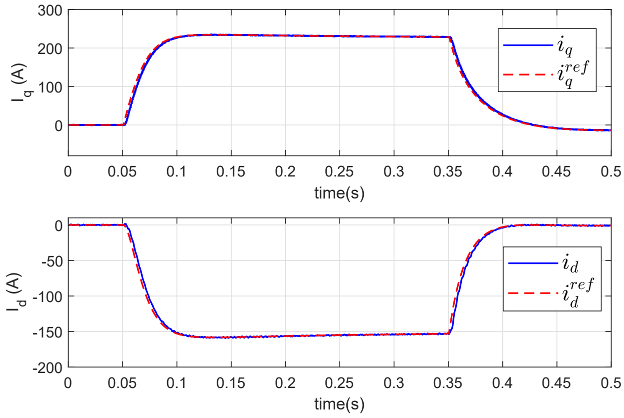

(a)

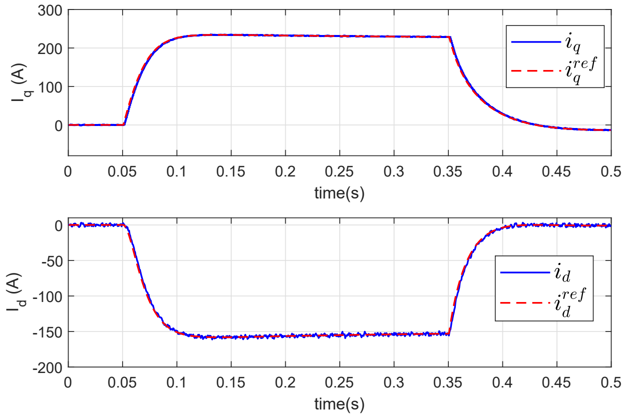

(b)

Fig. 5.8: Simulated dynamic responses of (a) DT-CVPI and (b) DO-PCC with 2 kHz sampling frequency at 300 Hz. $\hat{L}_d = 1.2L_d$, $\hat{L}_q = 1.2L_q$, $\hat{\psi}_{pm} = 0.5\psi_{pm}$.

proposed DT-CVPI when the motor accelerates from standstill to 100 Hz. It is shown that there are significant ripple components in the dq-axis currents when the prior current controller is employed at low-speed range. The same conclusion can be found in [103]. By comparison, the waveform of the feedback current is smooth if the proposed DT-CVPI is adopted. This test confirms that the proposed DT-CVPI is superior when compared with the prior method [6] at low-speed operation.

Fig. 5.8 shows simulation results of the DT-CVPI and DO-PCC under parameter mismatches: $\hat{L}_d = 1.2L_d$, $\hat{L}_q = 1.2L_q$, $\hat{\psi}_{pm} = 0.5\psi_{pm}$. The sampling frequency is 2 kHz and the electrical rotor speed is 300 Hz. Thus, the sampling frequency to fundamental frequency ratio f_{ratio} is $f_{ratio} = 2000/300 \approx 6.67$. It is seen that both controllers can work stably under low frequency ratio. Although there are some parameter mismatches, there is no static error during steady state. Additionally, the actual i_d and i_q can well track their references during dynamic process. The test can confirm good parameter robustness and satisfactory steady-state and transient performance of both controllers. However, the DO-PCC presents faster dynamic response when compared with DT-CVPI. As shown in Fig. 5.9, when the current commands steps from zero to its rated value, it takes 8.6 ms for the DT-CVPI to arrive the reference. On the contrary, the settling time of the proposed DO-PCC is only about 1 ms. The prior current controller [5] is also tested to confirm the effectiveness of modifying the IPMSM model for the design of DT-CVPI. As the prior current controller is designed for the nonsalient machine, the average inductance $(L_d + L_q)/2$ is applied in practical implementation [6]. It can be seen that the prior current controller consumes longest time to reach its reference and there is significant overshoot in the i_d. It is clear that the proposed DT-CVPI is more suitable for IPMSM than the prior current controller.

Fig. 5.10 shows experimental results of the dynamic responses when the rotor speed increases from 50 Hz to 100 Hz. The switching frequency and sampling frequency is 500 Hz in the test. One can see that both controllers perform well when the frequency ratio f_{ratio} decreases from 10 to 5. The main difference is that DO-PCC presents much faster transient response than DT-CVPI. Fig. 5.11 shows experimental results

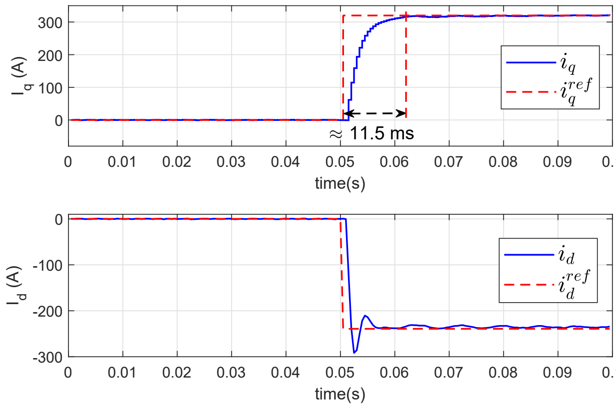

(a)

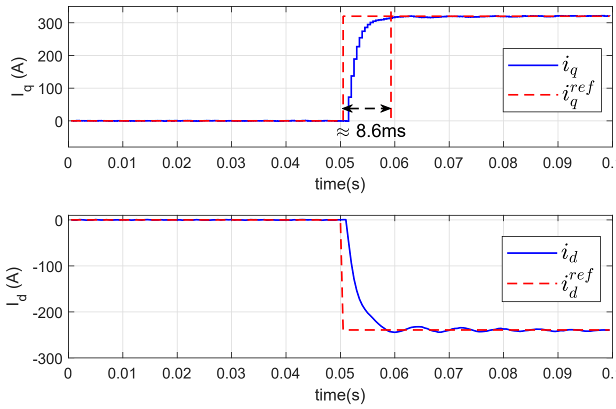

(b)

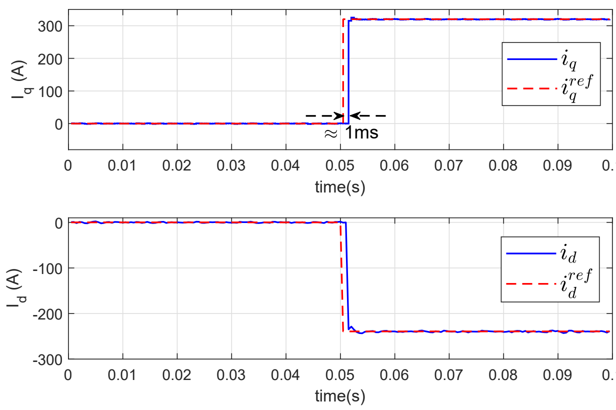

(c)

Fig. 5.9: Simulated step responses of (a) the prior current controller [5] (b) DT-CVPI and (c) DO-PCC with 2 kHz sampling frequency at 200 Hz.

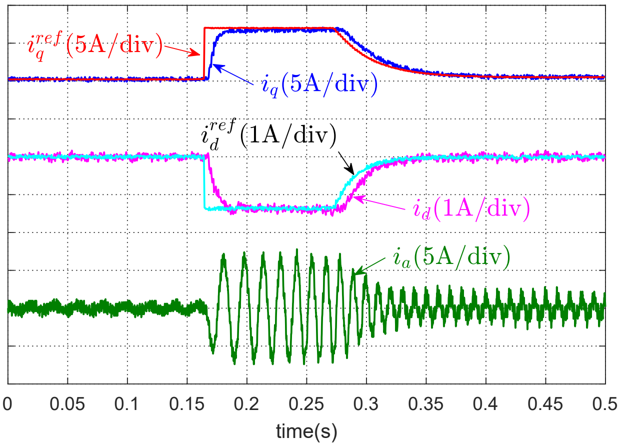

(a)

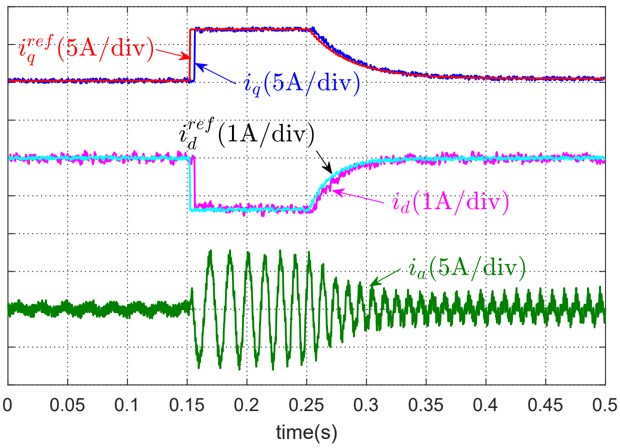

(b)

Fig. 5.10: Experimental results of dynamic responses for (a) DT-CVPI and (b) DO-PCC with 500 Hz sampling frequency when rotor speed increases from 50 Hz to 100 Hz.

when the external load is suddenly applied and then released. In the test, a PI controller is utilized to regulate speed and the speed reference is kept constant at 100 Hz. It is seen that when the load is changed, the rotor speed can quickly return to its reference. The actual q-axis current i_q can accurately track the command without static error for both controllers.

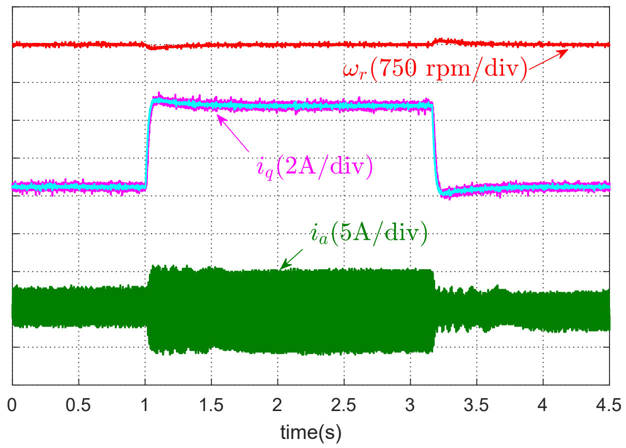

(a)

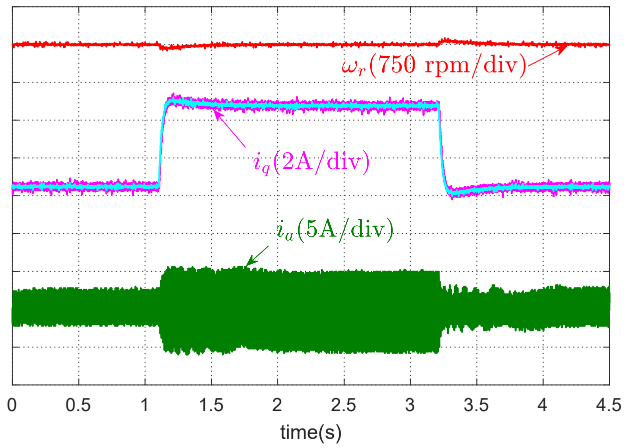

(b)

Fig. 5.11: Experimental results of dynamic responses for (a) DT-CVPI and (b) DO-PCC with 500 Hz sampling frequency when the load is suddenly applied and then released.

5.4.2 Verification of the Position-sensorless Operation

Fig. 5.12 shows the simulated responses of the estimated position at speed of 10 Hz and 300 Hz. As the sampling frequency is 2 kHz, the corresponding frequency ratios f_{ratio} are 20 and 6.67 respectively. From the simulation results, one can see that the estimated position coincides very well with the actual rotor position at both low and high speeds. Although there are significant current ripples when the frequency

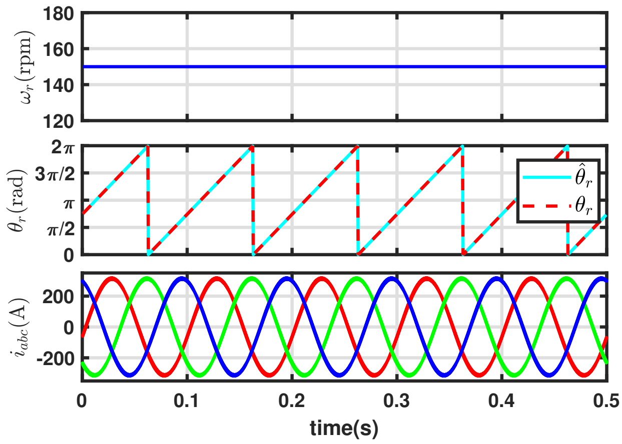

(a)

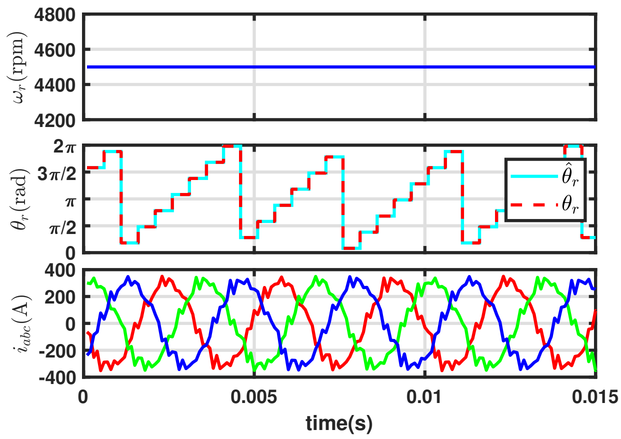

(b)

Fig. 5.12: Simulation results of position estimation with 2 kHz sampling frequency at the speed of (a) 10 Hz ($f_{ratio} = 20$) and (b) 300 Hz ($f_{ratio} \approx 6.67$).

ratio f_{ratio} decreases to relatively low value, there are no harmonics in the estimated position.

Fig. 5.13 shows the simulated position error when the rotor speed accelerates from 10 Hz to 300 Hz. If the conventional observer with Euler discretization is employed, the rotor position estimation error $\Delta\theta = \theta_r - \hat{\theta}_r$ gradually increases when the rotor speed increases. Hence, the performance of the conventional Euler based observer

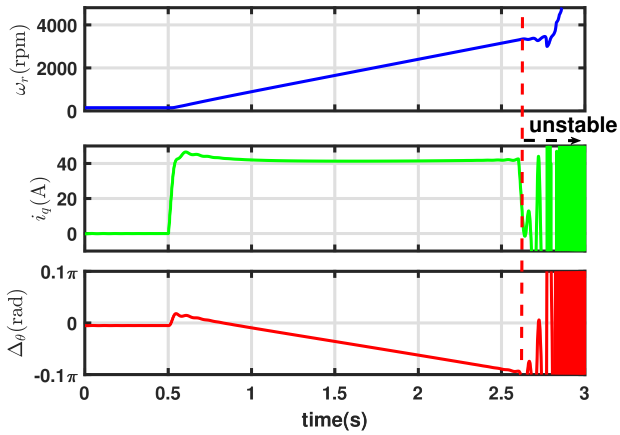

(a)

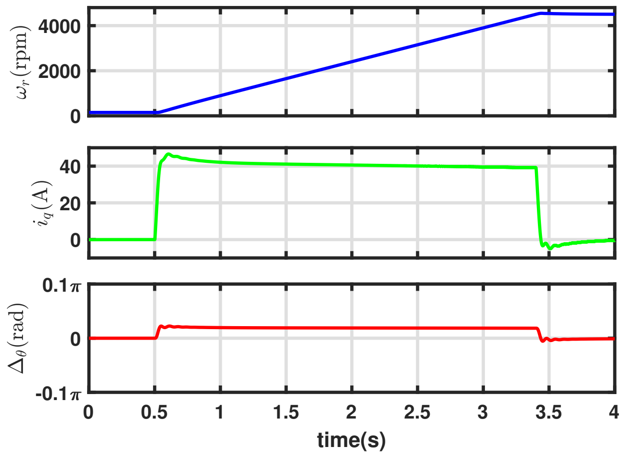

(b)

Fig. 5.13: Simulated position estimation error when the rotor speed increases from 10 Hz to 300 Hz with 2 kHz sampling frequency. (a) Using the observer with the conventional Euler discretization. (b) Using the proposed observer.

degrades under low sampling frequency to fundamental frequency ratio. When the rotor speed reaches to 3200 rpm ($f_{ratio} \approx 9$), the whole control system becomes unstable. By comparison if the proposed observer is employed, the rotor speed can be increased to the rated value. The maximum estimation error is only 0.07 rad during the speed variation. However, the steady state error is zero at both low

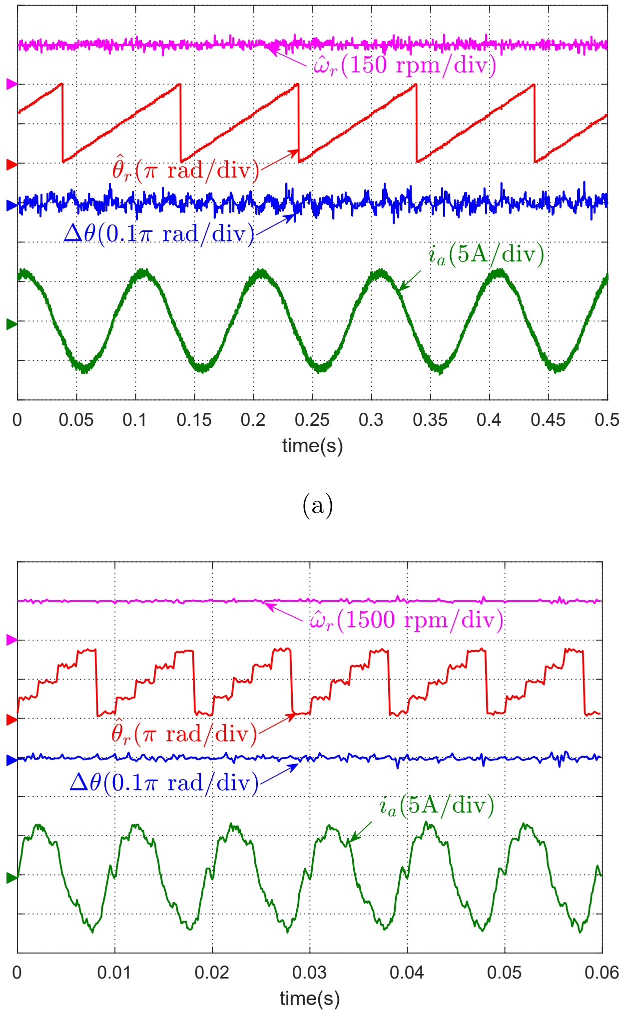

Fig. 5.14: Steady-state responses of the position-sensorless control under the rated load with 500 Hz sampling frequency at (a) 10 Hz ($f_{ratio} = 50$) and (b) 100 Hz ($f_{ratio} = 5$).

speed and high speed. The position estimation error during dynamic process is mainly caused by the speed delay because a low-pass filter is employed to filter out ripples in the estimated speed.

Fig. 5.14 shows steady-state responses with the rated load at 150 rpm and 1500 rpm. It is seen that the position error is small at low-speed and high-speed operation. The observer and current controller work stably when the frequency f_{ratio} is only

5. Due to low frequency ratio, the stator current is somewhat distorted at high speed. However, the estimated position is still in accordance with the actual value and the average position error is almost zero. As back-EMF is small at low speed, the observer is more sensitive to non-ideal factors, such as deadtime, noises and DC

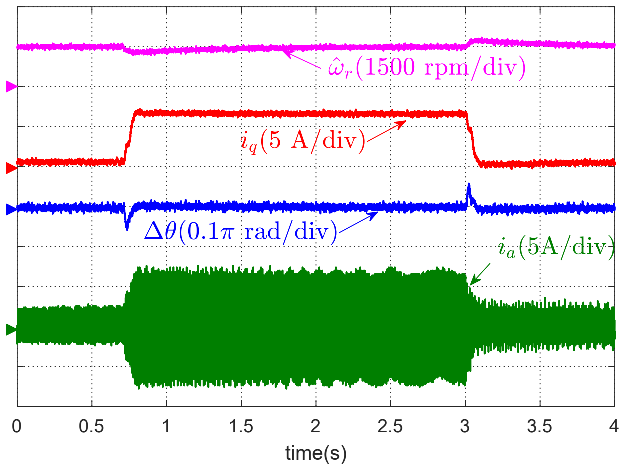

Fig. 5.15: Experimental results of responses to sudden load change at 100 Hz with 500 Hz sampling frequency.

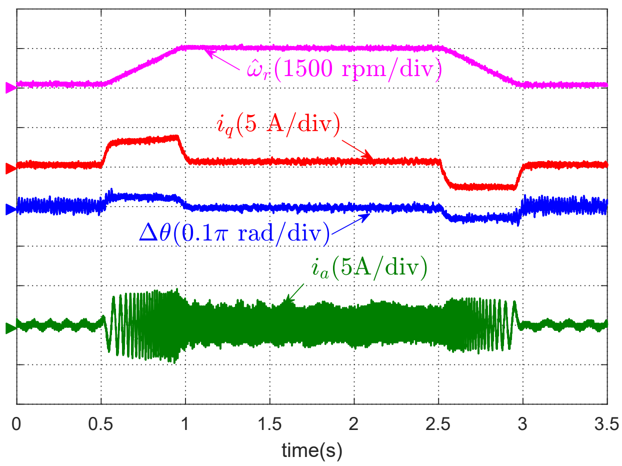

Fig. 5.16: Experimental results of responses during speed variation from 10 Hz to 100 Hz with 500 Hz sampling frequency.

bias in the measurement. As a result, the harmonic ripples in the position estimation are larger when compared with that at high speed. However, the observer is still stable under the rated load and the waveform of the stator current is sinusoidal without significant distortions. The tested results confirm that the proposed position estimator can work well under the rated load over a wide speed range and can keep good accuracy with low frequency ratio.

Fig. 5.15 shows experimental results when the rated external load is suddenly applied and then released at the rated speed. When the q-axis current changes, the estimated position would slightly deviate from its actual value. The maximum estimation error is about 9.5 degrees in this test. Although the frequency ratio is only 5, the system is stable and the average position estimation error during steady state is nearly zero.

Fig. 5.16 shows the tested responses during speed variation. Initially, the motor is rotating at 150 rpm. After a moment, the motor accelerates to 1500 rpm and then returns to 150 rpm. It can be seen that the position estimator can work stably during fast speed change (≈2900 rpm/s). At low speed operation, the observer is more sensitive to non-ideal factors of the inverter [123]. Therefore, the position errors get larger as speed decreases. Nevertheless, there is no excessive position error during fast speed variation.

5.5 Summary

In this chapter, the mathematical model of the IPMSM was modified based on which a discrete-time current controller was designed and verified by simulation and experimental tests. Compared with the prior complex-vector controller, the proposed one presents better decoupling control performance for the salient machine. However, similar to the prior method, the settling time during the dynamic process is relatively long. To further improve the transient performance, a digital predictive current controller was developed based on online disturbance adaption. Both controllers can work stably under low sampling frequency to fundamental frequency ratio without static tracking error. Simulation and experimental tests were carried out to validate the effectiveness of the proposed current controllers. Moreover, a discrete-time position observer was proposed to achieve position-sensorless operation. As the observer was directly designed based on a discrete-time domain model, the observer presents satisfactory estimation accuracy even under low frequency ratio. Simulation and experimental results validated that the proposed observer can accurately estimate the rotor position over a wide speed range. With the proposed current controller and position observer, high-performance position-sensorless control of IPMSM drive can be achieved under low frequency ratio. Therefore, the proposed methods are suitable for high-power and high-speed traction motor drives.

Chapter 6

Gearshift Control of the Dual Motor-Based Multi-speed Transmission

6.1 Introduction

Due to the increased global concern on air pollution, energy shortage and climate change, vehicle electrification picks up pace in the automobile industry recently [187]. Although great achievements have been made during past decades, the powertrain configurations, control schemes, etc. should be further improved to increase the competitiveness of an electric vehicle against convention internal combustion engine (ICE) based vehicles [187–189].

Compared to ICE, the electric motor features satisfactory controllability with fast dynamic response and good steady-state performance [190]. As a result, the vehicle can be smoothly launched from the standstill and thus equipment of a multi-speed transmission is not compulsory for a pure electric vehicle (PEV). However, it is still suggested in the existing research to employ multi-speed transmission (MST) for better driveability and overall efficiency [8–12]. With the proper MST configuration and control schemes [9], the power interruption during gearshift can be avoided, thereby, the long-term cost could be reduced without sacrificing driving performance [13]. Compared with the single-speed transmission, some additional effort is required for MST to guarantee smooth gearshift and suppress the shift jerk. Additionally, during fast acceleration process, driveline oscillations may be induced which would last for a long-time duration due to poor damping at the natural frequency. Specifically, low frequency oscillations at the frequency range of 1-10 Hz have a large impact on the driving comfort [162]. Hence, proper damping control method is necessary to reduce the sensitivity of shaft vibrations against motor torque variation during dynamic processes [191].

In conventional ICE vehicles, friction clutch, torque converter and torsional damper are usually adopted to ensure engine power is smoothly transferred to the wheel. Considering these mechanisms are relatively bulky and low efficiency, they are not recommended in a PEV transmission [12]. In this scenario, oscillations tend to occur in the driveline during gearshift and other transient processes due to lack of the ability to passively suppress torsional vibrations, resulting in significant up-down fluctuations of the vehicle jerk. To improve driving comfort, suppression of such vibrations is an important topic in the control of EVs [154, 192]. In [153], the difference between motor speed and vehicle speed is fed to a proportional-integral-derivative (PID) controller to suppress gearshift related oscillations. Satisfactory suppression of driveline vibrations is achieved but no theoretical analysis was carried out. As vehicle speed and motor speed are obtained from different control units, the network communication is required to collect speed information. However, the time delay of the network communication deteriorates control performance and thus proper delay compensation is required in practical application [152]. In [193], feed-forward torque compensation and feedback of speed error are combined to attenuate the torque demand and disturbance related vibrations respectively. The controller presented in [193] only requires motor torque and speed as the input which means the damping control algorithm can be integrated into the motor drive. In this way, network communication is not required and the complex delay compensation is thus avoided. Although fast and smooth acceleration response can be achieved, the controller is constructed based on the principle of canceling poorly damped poles which relies on accurate system model, giving rise to weak robustness against vehicle inertial variation. Considering vehicle inertial would change along with passengers and luggages, the damping controller must be able to handle the parameter mismatch. Some advanced control schemes, such as Linear-Quadratic-Gaussian (LQG) [154], H_∞ control [155], and model predictive control (MPC) [194], have also been applied to the active damping control. These optimization based controllers are attractive owing to their optimal performance in theory but they are usually complicated in the design and implementation.

In this chapter, aiming at improving the transient performance of a dual motor-based multi-speed transmission (DMMT) during and after gearshift, a discrete-time sliding mode torque observer (DSMTO) is designed and then a closed-loop torque control plus active suppression of torsional vibration is developed. The main contributions of the proposed method can be summarized as follows. 1) An extended sliding mode torque observer is designed in the discrete-time domain. As the discrete-nature of the implementation in a digital processor is directly considered in the design stage, more accurate result can be obtained in practical implementation. Due to the inherent low-pass filtering effect, the proposed DSMTO is immune against measurement noise and there is no high-frequency chattering problem as that of the conventional sliding mode observer. 2) A gearshift control method based on closed-loop torque regulation is proposed for the presented DMMT. By coordinated motor torque and speed control, fast gearshift without power interruption is achieved. 3) An active vibration damping control is designed and theoretically analyzed to suppress driveline oscillations induced by imperfect speed synchronization and the variation of shaft torque. Compared with the prior art, the proposed DSMTO and active damping control method only rely on the information of motor torque and speed. The wheel speed and unknown vehicle resistance torque, etc. are not required in the proposed controller. Therefore, the algorithm of the proposed DSMTO and active damping control can be directly integrated into the motor driver. Therefore the compensation for time delay due to network communication [152] and the exhaustive effort required on improving system robustness against unknown disturbances [31] are not required. Simulation and partial experimental results are demonstrated to verify the effectiveness of the proposed schemes.

6.2 DSMTO-based Active Damping Control

6.2.1 Sliding mode Torque Observer

Since the active damping control proposed in this chapter requires the information of the torque transmitted by the dog clutch, which is not directly available, a DSMTO will be developed in this section. In the existing literature [195, 196], the minimum value of the sliding mode gain is usually derived to guarantee stability. However, it will be shown in this section that the sliding mode gain should also have a upper limit when considering the observer is implemented in a digital processor.

Both the motion equation (3.16) and (3.17) can be rewritten into the following form

$$J_{eq}\frac{d\omega_M}{dt} = T_M - C_M\omega_M - T_D \tag{6.1}$$

where J_{eq} is the equivalent inertial connected on the motor rotor and T_D is the torque transmitted by the dog clutch. Applying the backward Euler discretization to (6.1) yields

$$\omega_M^{k+1} = \omega_M^k + \frac{T_{sc}}{J_{eq}}\left(T_M^k - C_M\omega_M^k - T_D^k\right) \tag{6.2}$$

where the superscript k means a variable at kth sampling instant and T_{sc} is the sampling period. Based on the model (6.2), an extended sliding mode torque observer is designed as

$$\hat{\omega}_M^{k+1} = \hat{\omega}_M^k + \frac{T_{sc}}{J_{eq}}\left(T_M^k - C_M\omega_M^k - \hat{T}_D^k - T_{smo}\right) \tag{6.3}$$

$$\hat{T}_D^{k+1} = \hat{T}_D^k + \lambda T_{sc}T_{smo} \tag{6.4}$$

where the hat "ˆ" denotes the estimated variable, $\lambda > 0$ is the adaption gain for the torque estimation and T_{smo} represents the sliding mode control function needs to be designed. Subtracting (6.2) from (6.3) results in

$$e_\omega^{k+1} = e_\omega^k + \frac{T_{sc}}{J_{eq}}\left(-e_T^k - T_{smo}^k\right) \tag{6.5}$$

where $e_\omega = \hat{\omega}_M - \omega_M$ is speed estimation error and $e_T = \hat{T}_D - T_D$ is torque estimation error. To derive the control function T_{smo}, the sliding surface is selected as $S = e_\omega = \hat{\omega}_M - \omega_M$ and the following reaching law [197] is employed.

$$S^{k+1} = S^k - T_{sc}(qZ(S^k) + hS^k) \tag{6.6}$$

where $q > 0$ and $h > 0$ are two reaching law parameters, and $Z(S^k)$ is a boundary switching function defined as

$$Z(S^k) = \begin{cases} Z_0 & e_\omega^k > Z_0 \\ e_\omega^k & \left|e_\omega^k\right| < Z_0 \\ -Z_0 & e_\omega^k < -Z_0 \end{cases} \tag{6.7}$$

where $Z_0 > 0$ is the boundary width. Substituting (6.6) into (6.5) yields

$$qJ_{eq}Z(S^k) + hJ_{eq}S^k = e_T^k + T_{smo}. \tag{6.8}$$

As torque estimation error is unknown, T_{smo} can be finally chosen as

$$T_{smo}^k = qJ_{eq}Z(S^k) + hJ_{eq}S^k \tag{6.9}$$

Stability Analysis

In the digital implementation, the concerned state variable is unable to precisely stay on the sliding surface, but only can move around it. To maintain stability, the state variable should always approach to the sliding surface if it is out of the boundary layer, namely

$$\left|S^{k+1}\right| < \left|S^k\right| \text{ if } \left|S^k\right| > Z_0 \tag{6.10}$$

The case when $\left|S^k\right| < Z_0$ will be studied later after solving (6.10). To satisfy condition (6.10), two cases, i.e., positive and negative values of S^k are considered.

Case I: If $S^{k+1} > 0$, inequality (6.10) can be rewritten as

$$\begin{cases} S^{k+1} - S^k < 0 \\ S^{k+1} + S^k > 0 \end{cases} \tag{6.11}$$

Considering $S^k > Z_0$, the following deduction can be obtained based on (6.5) and (6.9)

$$S^{k+1} - S^k = T_{sc}\left(-\frac{e_T^k}{J_{eq}} - qZ(S^k) - hS^k\right) < T_{sc}\left(-\frac{e_T^k}{J_{eq}} - qZ_0 - hZ_0\right) \tag{6.12}$$

When

$$(q+h)\,Z_0 > -\frac{e_T^k}{J_{eq}}, \tag{6.13}$$

$S^{k+1} - S^k < 0$ holds. From (6.5) and (6.9), $S^{k+1} + S^k$ can be expressed as

$$S^{k+1}+S^k = 2S^k+T_{sc}\left(-\frac{e_T^k}{J_{eq}} - qZ(S^k) - hS^k\right) > (2-hT_{sc}-qT_{sc})Z_0-T_{sc}\frac{e_T^k}{J_{eq}} \tag{6.14}$$

When

$$(q+h)\,Z_0 < \frac{2Z_0}{T_{sc}} - \frac{e_T^k}{J_{eq}}, \tag{6.15}$$

$S^{k+1} + S^k > 0$ holds.

Case II: If $S^k < 0$, (6.10) can be expanded as

$$S^{k+1} - S^k > 0 \tag{6.16}$$

$$S^{k+1} + S^k < 0 \tag{6.17}$$

Omitting the tedious deriving process and following the same procedure as case I, it is found that (6.16) and (6.17) are equivalent to the following two inequalities

$$(q+h)\,Z_0 > \frac{e_T^k}{J_{eq}} \tag{6.18}$$

$$(q+h)\,Z_0 < \frac{2Z_0}{T_{sc}} + \frac{e_T^k}{J_{eq}} \tag{6.19}$$

Combining (6.13), (6.15), (6.18) and (6.19), if the following inequality holds

$$\frac{\left|e_T^k\right|}{J_{eq}} < (q+h)\,Z_0 < \frac{2Z_0}{T_{sc}} - \frac{\left|e_T^k\right|}{J_{eq}}, \tag{6.20}$$

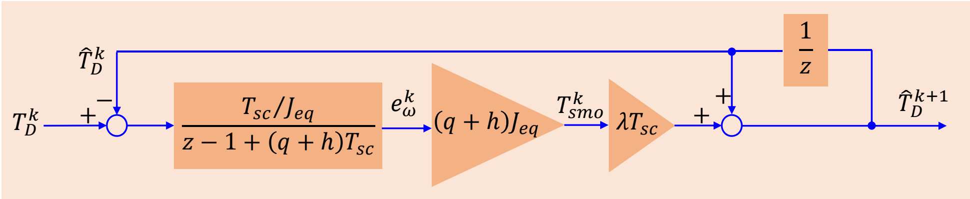

Fig. 6.1: Equivalent model of the proposed torque estimation.

then (6.10) is always satisfied. The existing literature usually derives the minimum requirement of the sliding mode gain only and the upper limit is neglected. It will be verified in Section 6.4 that the upper boundary is necessary to avoid high-frequency chattering in the torque estimation. To ensure there is a solution for (6.20), the upper limit should be larger than the minimum requirement, i.e., (6.21) must be satisfied.

$$Z_0 > \frac{\left|e_T^k\right| T_{sc}}{J_{eq}} \tag{6.21}$$

The conditions (6.20) and (6.21) are derived when $\left|S^k\right| > Z_0$. In the following text, the case when $\left|S^k\right| < Z_0$ is considered.

Based on (6.7), substituting (6.9) into (6.5), the following transfer function can be derived if $\left|S^k\right| < Z_0$

$$G_\omega(z) = \frac{e_\omega(z)}{e_T(z)} = -\frac{T_{sc}}{J_{eq}} \frac{1}{z - 1 + (q+h)T_{sc}} \tag{6.22}$$

where z is a shift operator in the discrete-time domain. The pole of the system $G_\omega(z)$ is

$$P_\omega = 1 - (q+h)T_{sc} \tag{6.23}$$

To maintain a stable speed estimation, $|p_\omega| < 1$ should be hold, i.e.,

$$0 < q + h < \frac{2}{T_{sc}} \tag{6.24}$$

From (6.4), (6.9) and (6.22), the diagram of the torque estimation loop can be derived as shown in Fig. 6.1. From the figure, the transfer function from the actual clutch torque to the estimated clutch torque can be obtained as

$$G_T(z) = \frac{\hat{T}_D}{T_D} = \frac{\lambda(q+h)T_{sc}^2}{z^2 - (2-(q+h)T_{sc})\,z + 1 + (\lambda T_{sc}-1)(q+h)T_{sc}} \tag{6.25}$$

The poles of $G_T(z)$ are

$$P_T^{1,2} = \frac{2-(q+h)T_{sc} \pm T_{sc}\sqrt{(q+h)(q+h-4\lambda)}}{2} \tag{6.26}$$

If

$$\lambda = \frac{q+h}{4} \tag{6.27}$$

a critically damped system can be obtained and thus the overshoot can be avoided in the dynamic process. It should be noted that $|P^{1,2}| < 1$ always holds with the selected λ due to the limitation of (6.24) thereby a stable torque estimation can be ensured.

Performance Analysis and Parameter Tuning

With a constant T_D, the final value of $\hat{T}_D$ can be solved from (6.25) according to the final value theorem (chapter 2-4 in [198]) as

$$\lim_{k\to\infty} \hat{T}_D^k = \lim_{z\to 1}\left((1-z^{-1})\frac{\lambda(q+h)T_{sc}^2}{z^2-(2-(q+h)T_{sc})\,z+1+(\lambda T_{sc}-1)(q+h)T_{sc}}\frac{T_D}{1-z^{-1}}\right) = T_D \tag{6.28}$$

It is clear that the estimated torque $\hat{T}_D$ from the proposed DSMTO can finally converge to its actual value without estimation error. As seen in (6.22), the system G_ω behaves like a low-pass filter if $q+h < 1/T_{sc}$ holds. On the contrary, the system is vulnerable to high-frequency noise if $q+h$ is chosen to be larger than $1/T_{sc}$. To

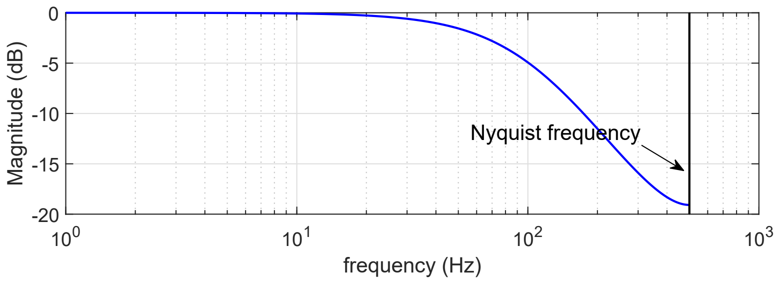

Fig. 6.2: Frequency responses of $G_T(z)$ with 1 kHz sampling frequency.

achieve fast dynamic response without high sensitivity to the measurement noise, the following critical condition is selected.

$$q + h = \frac{1}{T_{sc}} \tag{6.29}$$

From (6.27) and (6.29), the parameter λ can be determined as

$$\lambda = \frac{1}{4T_{sc}} \tag{6.30}$$

Additionally, as the estimated $\hat{T}_D$ can accurately track the actual torque T_D, the estimation error $\left|e_T^k\right|$ would be small during normal operation. In order to satisfy (6.20), the minimum value of Z_0 should be 0.5 under the prerequisite (6.29) if the impact of $\left|e_T^k\right|$ is neglected. However, to increase system robustness against the torque estimation error and reduce chattering, $Z_0 = 1$ is chosen in this study. In the reaching law (6.6), q represents constant reaching rate and h denotes proportional reaching rate. To obtain faster dynamic response, larger h is required if state variable is far away from the sliding surface whilst larger q is favorable when the state variable is close to the sliding surface. For simplicity, equal weight is given to the q and h in this study, i.e.,

$$q = h = \frac{1}{2T_{sc}} \tag{6.31}$$

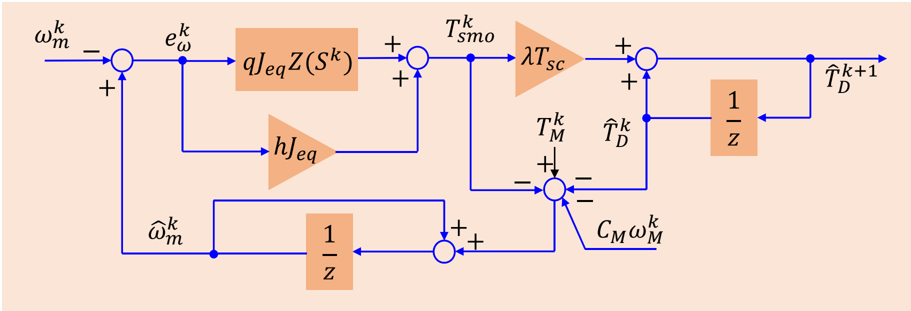

Fig. 6.3: Block diagram of the proposed DSMTO.

With the selected observer parameters, Fig. 6.2 shows frequency responses of $G_T(z)$ when the $T_{sc} = 1$ ms. It is seen that $G_T(z)$ presents the characteristic of a low-pass filter. Therefore, the high-frequency harmonics can be effectively attenuated in the estimated clutch torque. In summary, the proposed DSMTO can give an accurate estimation of the torque transmitted by the dog clutch while suppressing high-frequency harmonics. The schematic diagram of the proposed DSMTO is presented in Fig. 6.3.

Calculation of Clutch Torque

As there are two motor drives in the studied transmission, two DSMTOs can be constructed based on motion equations (3.16) and (3.17), giving two torque estimations $\hat{T}_{DM1}$ and $\hat{T}_{DM2}$ respectively. Comparing (3.16) and (3.17) with (6.1), $\hat{T}_{DM1}$ and $\hat{T}_{DM2}$ can be expressed as

$$\hat{T}_{DM1} = \hat{T}_{D1}/r_1 + \hat{T}_{D3} \tag{6.32}$$

$$\hat{T}_{DM2} = \hat{T}_{D2}/r_2 - \hat{T}_{D3} \tag{6.33}$$

As at least one of the dog clutches D1, D2 and D3 is disengaged, the clutch torque $\hat{T}_{D1}$, $\hat{T}_{D2}$ and $\hat{T}_{D3}$ can be calculated from (6.32) and (6.33) according to dog clutch

Table 6.1 : Torque estimations under different clutch states.

D1	D2	D3	$\hat{T}_{D1}$	$\hat{T}_{D2}$	$\hat{T}_{D3}$
1	1	0	$r_1\hat{T}_{DM1}$	$r_2\hat{T}_{DM2}$	0
1	0	1	$r_1\left(\hat{T}_{DM1}+\hat{T}_{DM2}\right)$	0	-$\hat{T}_{DM2}$
0	1	1	0	$r_2\left(\hat{T}_{DM1}+\hat{T}_{DM2}\right)$	$\hat{T}_{DM1}$
1	0	0	$r_1\hat{T}_{DM1}$	0	0
0	1	0	0	$r_2\hat{T}_{DM2}$	0
0	0	0	0	0	0

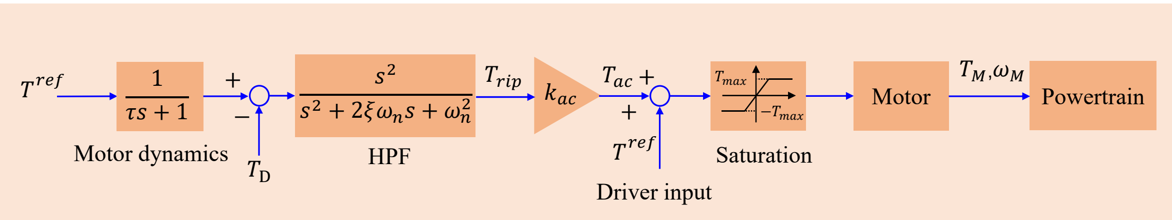

Fig. 6.4: Control diagram of the proposed active damping control.

states. For example, if dog clutches D1, D2 are engaged and D3 is disengaged, $\hat{T}_{D3} = 0$ holds in this case. Then, $\hat{T}_{D1}$ and $\hat{T}_{D2}$ can be calculated from (6.32) and (6.33) as $\hat{T}_{D1} = r_1\hat{T}_{DM1}$ and $\hat{T}_{D2} = r_2\hat{T}_{DM2}$. Similarly, $\hat{T}_{D1}$, $\hat{T}_{D2}$ and $\hat{T}_{D3}$ in other cases can be derived and they are summarized in Table 6.1.

6.2.2 Principle of the Active Damping Control

In practical situation, unknown disturbances such as ripples in the motor torque and imperfect motor speed synchronization, may cause driveline resonance. There-

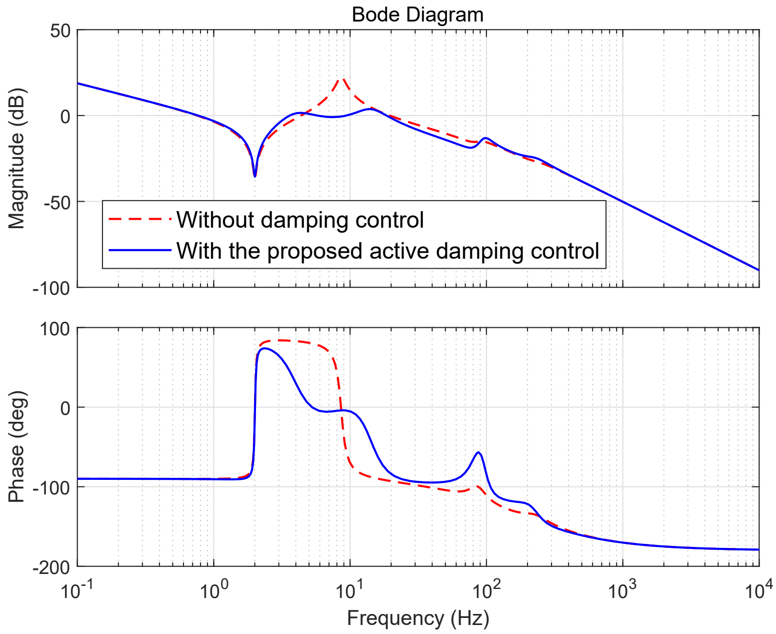

Fig. 6.5: Bode diagram of the powertrain system with the proposed active damping control.

fore, it is essential to incorporate an active damping control to suppress vibrations induced by unknown disturbances to improve driving comfort. If there are driveline oscillations, the torque transmitted by the dog clutch would also contains ripple components. Through the feedback of these ripple components, it is possible to suppress the driveline resonance during dynamic process. To avoid the interference between the damping controller and the gearshift controller, only the oscillating component should be fed to the damping controller. In this study, a second-order high pass filter (HPF) $G_{HPF}(s)$ show in (6.34) is used to extract the ripple component in the clutch torque T_D.

$$T_{rip}(s) = \underbrace{\frac{s^2}{s^2 + 2\xi\omega_n s + \omega_n^2}}_{G_{HPF}(s)} \left(\underbrace{\frac{1}{\tau s + 1}}_{\text{control delay}} T^{ref} - T_D \right) \tag{6.34}$$

where ξ is the damping ratio usually set as $\sqrt{2}/2$ for optimum dynamic performance and ω_n is the nature frequency which can be set as the lowest resonant frequency of

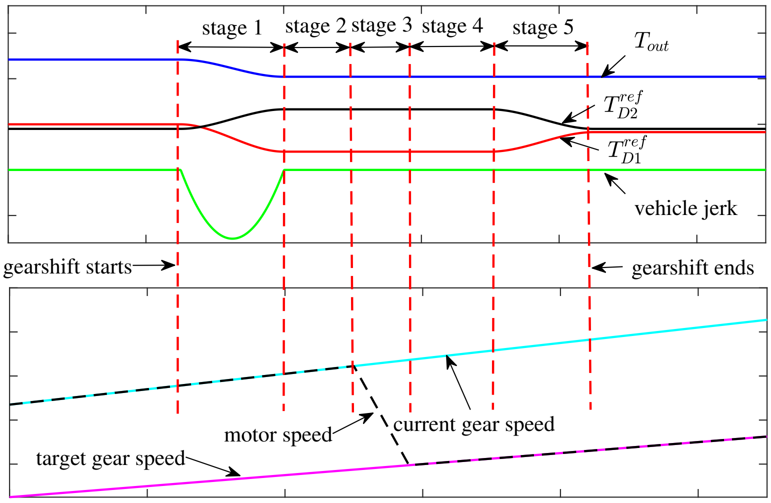

Fig. 6.6: Schematic diagram of an ideal gearshift process.

the powertrain. To compensate for the control delay of the motor drive, the delay model expressed in (3.25) is incorporated for higher accuracy. The block diagram of the proposed active damping control is demonstrated in Fig. 6.4. In the proposed method, only the proportional controller with a gain k_{ac} is utilized so that the DC drift of the integral controller and high noise-sensitivity of the derivative controller can be avoided. The frequency responses of the powertrain system with the proposed active damping control is illustrated in Fig. 6.5. Obviously, the proposed method can effectively reduce the resonant peak whilst the responses at low and high frequency range is almost unaffected. For digital implementation, $G_{HPF}(s)$ can be discretized by the Tustin method with $T_{sc} = 1$ ms and $\omega_n = 54$ rad/s as

$$G_{HPF}(z) = \frac{0.96255 - 1.9251z^{-1} + 0.96255z^{-2}}{1 - 1.9237z^{-1} + 0.9265z^{-2}} \tag{6.35}$$

6.3 Gearshift Control of DMMT

A complete gear shifting process contains five stages in the proposed control method, including 1) release load from the motor preparing for gearshift and increase the torque of the other motor simultaneously to fill up torque gap; 2) disengage the off-going dog clutch when its torque is decreased to zero; 3) synchronize motor speed to the target gear; 4) engage the on-going dog clutch for the target gear; and 5) re-balance torque between the motor M1 and M2. A schematic diagram of these stages is illustrated in Fig. 6.6. For clear explanation, changing the gear for the motor M1 is taken as an example to detail the gearshift process. Due to symmetry of M1 and M2 in the powertrain configuration, the same procedure is applied to the case when M2 changes the gear.

Stage 1: Reduce the load from the motor M1 so that the torque transmitted by the connected clutch can be eventually decreased to zero. At the same time, the output torque of M2 is increased to compensate for the torque gap. As seen from the motion equation (6.1), the second derivative of the speed (jerk) is proportional to the first derivative of the torque. To reduce vehicle jerk during gearshift, the clutch torque should be increased/decreased smoothly. In this stage, the following third-order polynomial [11] is adopted as the torque trajectory.

$$T_{D1}^{ref}(t) = \frac{2T_{D0}(t-t_0)^3}{(t_1-t_0)^3} - \frac{3T_{D0}(t-t_0)^2}{(t_1-t_0)^2} + T_{D0} \tag{6.36}$$

$$T_{out}^{ref}(t) = \frac{2(T_t-T_0)(t-t_0)^3}{(t_1-t_0)^3} - \frac{3(T_t-T_0)(t-t_0)^2}{(t_1-t_0)^2} + T_0 \tag{6.37}$$

$$T_{D2}^{ref}(t) = T_{out}^{ref}/r_f - T_{D1}^{ref} \tag{6.38}$$

where t_0 is the instant when the stage 1 starts and t_1 is the expected instant when the stage 1 ends; T_{D1}^{ref} is the torque reference for the dog clutch connected to M1; T_{D2}^{ref} is the torque reference for another clutch connected to M2; T_{out}^{ref} is the reference of output torque from the final drive; T_{D0} and T_0 are values of T_{D1}^{ref} and T_{out}^{ref} at the instant t_0 respectively; and T_t is the expected output torque after the gearshift and it is calculated based on the driver input as follows

$$T_t = \gamma \cdot r_f \cdot (r_1^{new} T_{n1} + r_2 T_{n2}) \tag{6.39}$$

where γ represents percentage of the throttle opening; r_1^{new} denotes the target gear ratio; r_2 is reduction ratio of the gear connected to the M2; and T_{n1} and T_{n2} are the rated torque of M1 and M2 respectively. From (6.37), the first and second derivative of T_{out}^{ref} can be solved as

$$\frac{dT_{out}^{ref}}{dt} = \frac{6(T_t - T_0)(t - t_0)^2}{(t_1 - t_0)^3} - \frac{6(T_t - T_0)(t - t_0)}{(t_1 - t_0)^2} \tag{6.40}$$

$$\frac{d^2T_{out}^{ref}}{dt^2} = \frac{12(T_t - T_0)(t - t_0)}{(t_1 - t_0)^3} - \frac{6(T_t - T_0)}{(t_1 - t_0)^2} \tag{6.41}$$

It can be easily calculated that $dT_{out}^{ref}/dt = 0$ holds at $t = t_0$ and $t = t_1$. Hence, the vehicle jerk is zero in theory when the stage 1 starts and ends. Solving $d^2T_{out}^{ref}/dt^2 = 0$ for time t, it can be found that the maximum dT_{out}^{ref}/dt would occur at $t = 0.5(t_0+t_1)$ and the maximum value of dT_{out}^{ref}/dt can be calculated from (6.40) as

$$\left.\frac{dT_{out}^{ref}}{dt}\right|_{max} = \frac{1.5(T_t - T_0)}{t_1 - t_0} \tag{6.42}$$

Considering vehicle speed ω_v is the product of tire radius r_w and wheel speed, the maximum vehicle jerk resulting from the variation of T_{out} can be derived from (6.42) as (6.43) if the impact of other disturbances, such as load and driveline oscillations

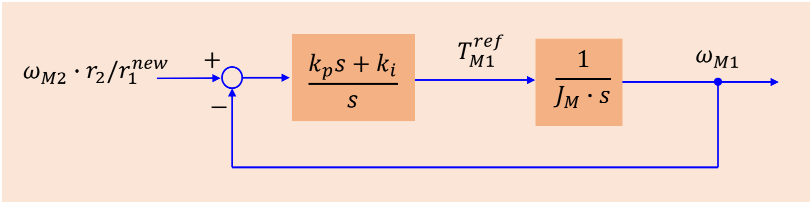

Fig. 6.7: Schematic diagram of the speed regulation during gearshift.

are neglected.

$$\left.\underbrace{\frac{d^2\omega_v}{dt^2}}_{J_k}\right|_{max} = \frac{r_w}{J_v}\frac{dT_{out}^{ref}}{dt} = \frac{r_w}{J_v}\frac{1.5\,|T_t - T_0|}{t_1 - t_0} \tag{6.43}$$

Based on (6.43), the time duration $t_1 - t_0$ can be solved from the maximum acceptable vehicle jerk J_{kmax} as

$$\Delta t = t_1 - t_0 = \frac{r_t}{J_v}\frac{1.5\,|T_t - T_0|}{J_{kmax}} \tag{6.44}$$

To avoid high vehicle jerk during gearshift, Δt expressed in (6.44) indicates the minimum time required for the stage 1.

Stage 2: Disengage dog clutch connected to motor M1 when the transmitted torque is decreased to zero. As the contact force of the dog clutch is controlled to be around zero in this stage, the dog clutch can be safely disengaged without inducing significant transient oscillations in the powertrain. *Stage* 3: Synchronize the speed of M1 to that of the target gear. After the dog clutch is disengaged and the motor M1 is disconnected from the transmission, the motor drive will be switched from the torque control mode to the speed control mode. In this stage, a PI controller is used to regulate motor speed as shown in Fig. 6.7. As mechanical time constant is much larger than the control delay of the motor drive, the torque control loop in the motor drive can be assumed to be unit when designing the speed controller [47]. Therefore, with a PI controller, the closed-loop transfer function can be obtained from Fig. 6.7 as

$$G_{sp}(s) = \frac{\omega_{M1}(s)}{\omega^{ref}(s)} = \frac{k_p/J_M \cdot s + k_i/J_M}{s^2 + k_p/J_M \cdot s + k_i/J_M} \tag{6.45}$$

where ω^{ref} is the speed reference of the target gear calculated as

$$\omega^{ref} = \frac{\omega_{M2} \cdot r_2}{r_1^{new}} \tag{6.46}$$

Setting the poles of $G_{sp}(s)$ as that of the second-order Butterworth-type filter, the PI gains can be designed as

$$k_p = \sqrt{2} J_M \omega_c \tag{6.47}$$

$$k_i = J_M \omega_c^2 \tag{6.48}$$

where ω_c is the cut-off frequency. Higher ω_c leads to faster dynamic responses but also higher noise-sensitivity. Based on the trade-off between dynamic and steady-state performance, ω_c is chosen as 80 in this study.

Stage 4: Engage dog clutch. As the motor speed has been synchronized to the target gear in the stage 3 and the contact force is controlled to be around zero, the dog clutch can be safely engaged in this stage.

Stage 5: Re-balance the torque between M1 and M2. Once the target gear is engaged, the torque transmitted by two clutches should be recovered to its normal value. In this stage, the output torque of M1 is gradually increased while the torque of M2 is simultaneously decreased so that the output torque of the transmission is kept constant as seen in Fig. 6.6. The same as the stage 1, the third-order polynomial is adopted as the torque trajectory for T_{D1}^{ref}. Since the initial value of

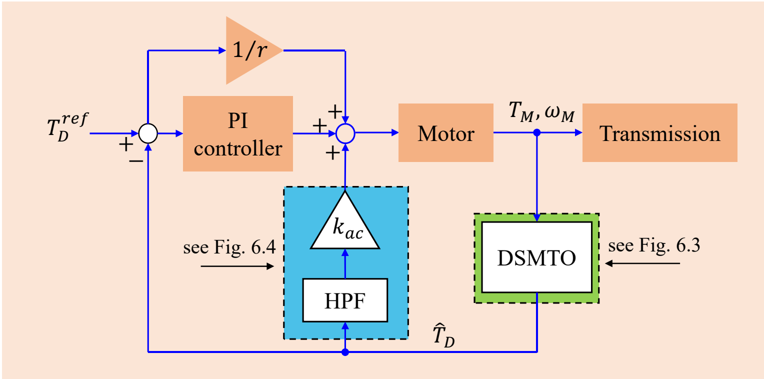

Fig. 6.8: Control diagram of the proposed gearshift controller.

T_{D1} in this stage is zero, $T_{D1}^{ref}(t)$ can be computed as

$$T_{D1}^{ref}(t) = \frac{2T_{dt}(t-t_0)^3}{(t_1-t_0)^3} - \frac{3T_{dt}(t-t_0)^2}{(t_1-t_0)^2} \tag{6.49}$$

where $T_{dt} = \gamma \cdot r_1 \cdot T_{n1}$ is the target torque transmitted by the dog clutch D1. To keep the output torque of the transmission at its target value T_t, T_{D2}^{ref} is calculated as

$$T_{D2}^{ref} = T_t/r_f - T_{D1}^{ref} \tag{6.50}$$

From the above gearshift process, it is found that the clutch torque should be controlled to follow their reference. A closed-loop clutch torque control is thus necessary to achieve the desired performance. Additionally, the previously introduced active damping control should be integrated so that the driveline vibrations induced by the torque variation and imperfect speed synchronization can be suppressed. Based on the proposed DSMTO, the whole control diagram is shown in Fig. 6.8. From the figure, it is seen that the clutch torque control includes a feedforward part to increase dynamic response and a feedback PI controller to enhance system robustness against disturbances. The active damping control shown in Fig. 6.4 is also

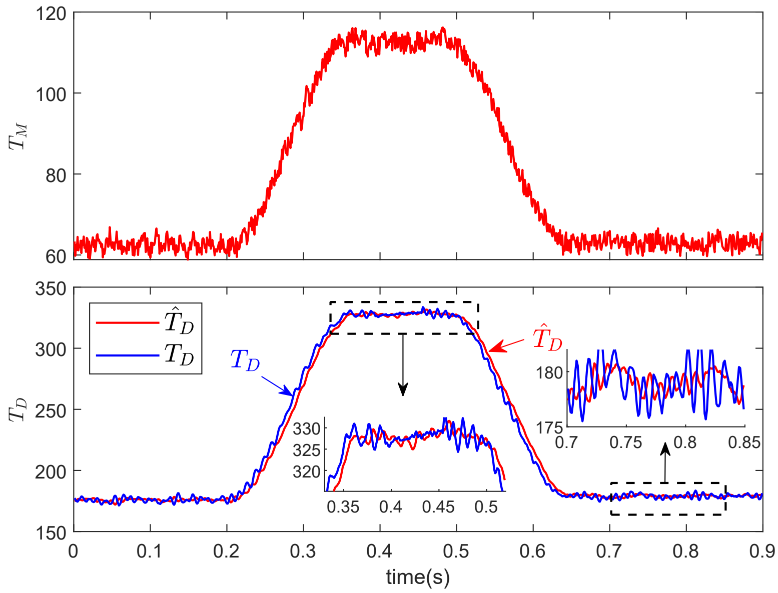

Fig. 6.9: Simulated responses of the motor torque, actual clutch torque and estimated clutch torque during gearshift.

incorporated in order to suppress driveline resonance.

6.4 Simulation and Experimental results

In all simulation and experimental tests, the sampling frequency is set as 1 kHz for the DSMTO and gearshift controller. In practical application, the motor drive is usually fed by a inverter whose output contains high frequency harmonics. To make the simulation closer to the reality, random noise is deliberately added in the motor output torque and speed measurement in all simulation tests.

6.4.1 Verification of DSMTO

As the gearshift controller and active damping controller are designed based on the proposed DSMTO, it is necessary to verify its effectiveness first. Fig. 6.9 shows simulation results of the estimated clutch torque during a gearshift process. It is seen that torque trajectories are third-order polynomial during transient process as defined in Section 6.3. Although there are significant high-frequency ripples in the motor torque, the estimated clutch torque $\hat{T}_D$ is relatively smooth without obvious chattering and ripple components. During dynamic process, there is minor delay in the torque estimation but the average value of $\hat{T}_D$ well matches with its actual one during steady state.

In prior methods, a large enough sliding mode gain is usually suggested to ensure stability of the observer [195, 196]. However, as described in Section 6.2.1, there is also a upper constraint in digital implementation to ensure the concerned state

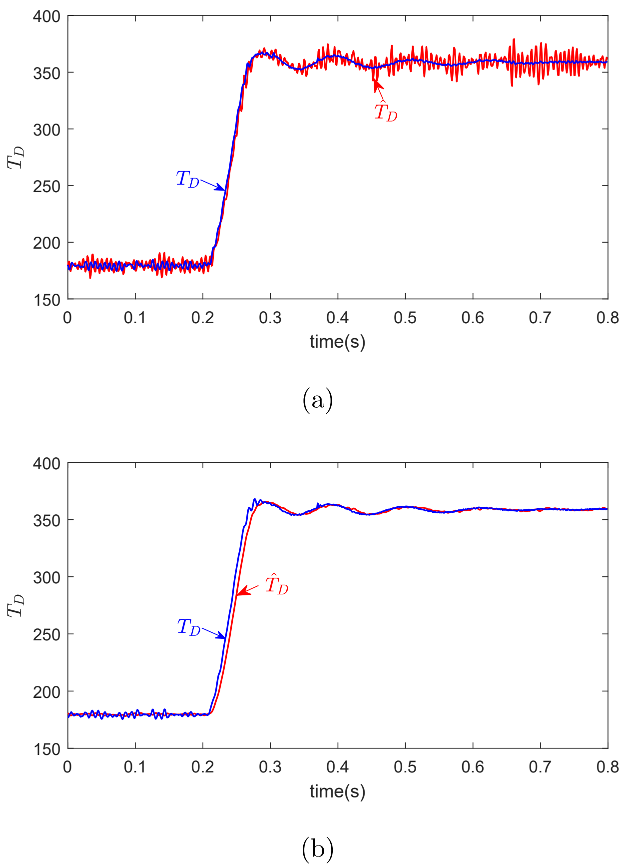

Fig. 6.10: Simulated results of the estimated clutch torque with (a) sliding mode gains larger than the upper condition (6.20) and (b) sliding mode gains designed in this study.

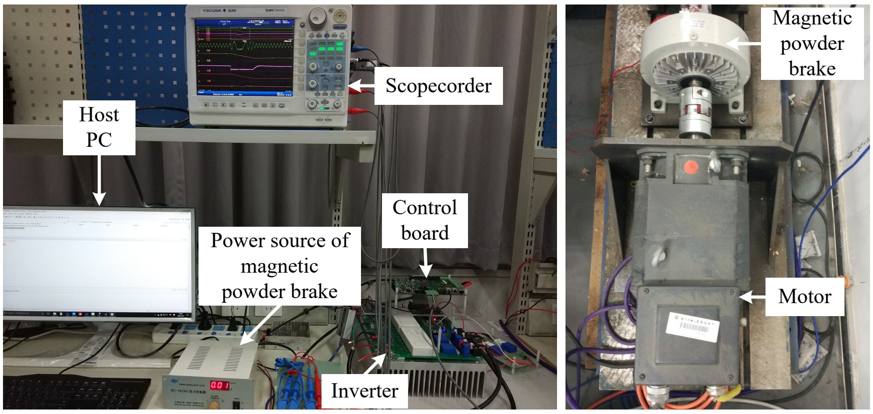

Fig. 6.11: Experimental setup for testing DSMTO.

variable always move toward the boundary layer. If it is violated, significant chattering phenomenon would occur. Fig. 6.10 shows responses of the estimated clutch torque when the sliding mode gain is larger than the upper limit derived in this chapter. For comparison, the waveform of $\hat{T}_D$ with observer parameters designed in Section 6.2.1 is also illustrated. Additionally, to justify the proposed DSMTO can effectively track the low-frequency oscillations in the driveline, the active damping controller is disabled in this test. It is clear that the DSMTO with well designed parameters presents much smaller ripples. The estimated $\hat{T}_D$ can well follow the torque vibrations induced by gearshift. On the contrary, there are significant harmonic components when observer parameters are not properly selected according to the conditions derived in this chapter.

To further verify the effectiveness of the proposed DSMTO, it is tested on a down-scaled test-rig as shown in Fig. 6.11, which includes an induction motor and a magnetic powder brake used to emulate the load applied from the clutch to the motor. Fig. 6.12 shows experimental results when the 14 Nm load is suddenly

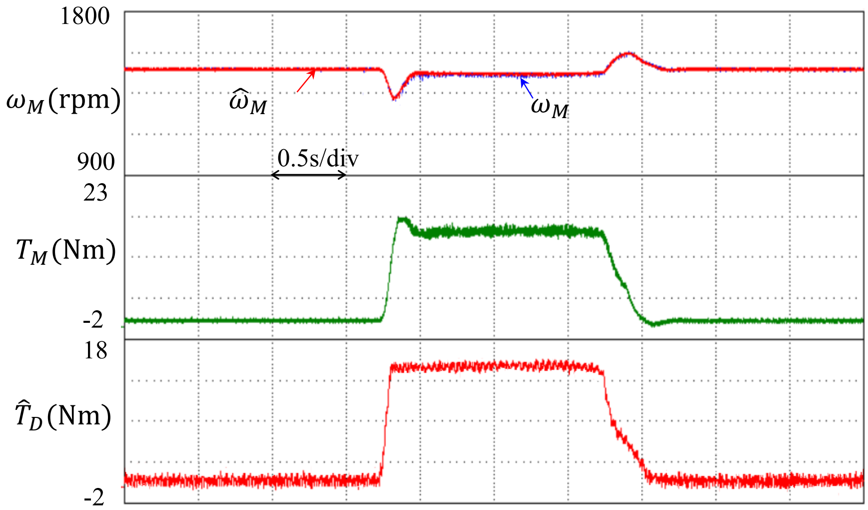

Fig. 6.12: Experimental tests of DSMTO when the load torque is suddenly applied and released.

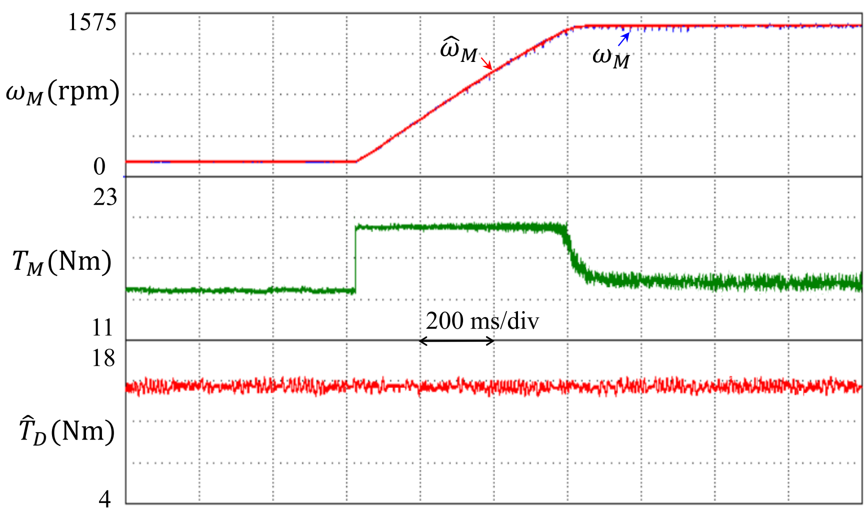

Fig. 6.13: Experimental results of torque estimation with varied motor speed.

applied and then released by the powder brake. In the figure, the motor speed is controlled at 1500 rpm by the PI controller shown in Fig. 6.7. When the load is suddenly applied and released, the motor torque changes accordingly to counter the impact of the load on speed tracking. During transient process, the motor speed slightly deviates from the reference but recovers quickly. The estimated load torque $\hat{T}_D$ can smoothly converge to its actual value after the load is applied and released. Although noise and ripples exist in the measured speed and motor torque, the estimated speed $\hat{\omega}_M$ keeps consistent with the actual speed ω_M and there is no chattering in both $\hat{\omega}_M$ and $\hat{T}_D$. Apart from the test under load change, performance under speed variation is also examined. As seen from Fig. 6.13, the motor is initially running at 150 rpm and then accelerates to 1500 rpm while 14 Nm load is always applied by the powder brake. It is seen that the waveform of the estimated speed $\hat{\omega}_M$ almost coincides with the actual speed ω_M during both dynamic and steady state. This indirectly validate the correctness of the estimated load torque. Moreover, the average value of the estimated torque $\hat{T}_D$ is not affected by the varied speed, indicating the decoupled speed estimation and load torque estimation is well achieved. As the ratio of inverter switching frequency over the fundamental voltage frequency decreases with larger motor speed, the output torque T_M contains more harmonics when ω_M increases [164]. However, the estimated torque $\hat{T}_D$ is kept smooth without significant high-frequency ripples because of filtering effect of the DSMTO.

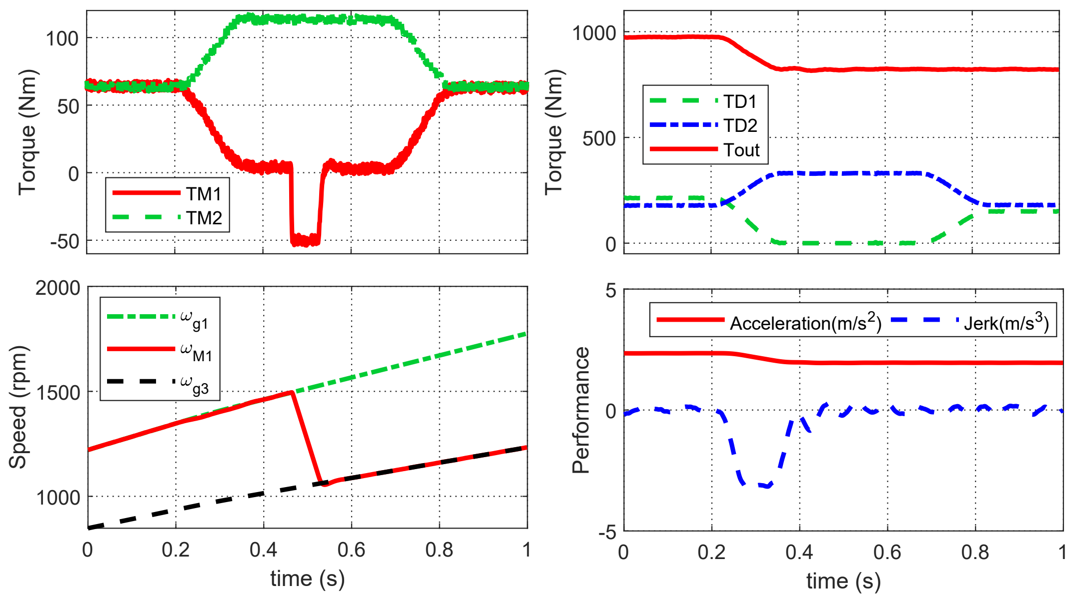

Fig. 6.14: Simulation results of power-on upshift when M1 changes gear from G1 to G3.

6.4.2 Verification of Gearshift Control

To verify the effectiveness of the proposed control scheme, simulations were carried out in the environment of Matlab/Simulink. To justify that the developed control scheme can be easily integrated into the motor controller, the control algorithm illustrated in Fig. 6.8 was implemented on a digital signal processor TI TMS320F28335-based control board shown in Fig. 6.11. The program code of the control algorithm was auto generated by the MATLAB/Embedded Coder toolbox and then it was downloaded into the processor. In practical test, it only takes 8.79 μs to execute the whole control algorithm, including DSMTO, active damping control and clutch torque control. Considering the execution time is much smaller than the 1 ms sampling time required here, the result indicates the online computation burden of the proposed method is small and suitable for implementation on an embedded microcontroller.

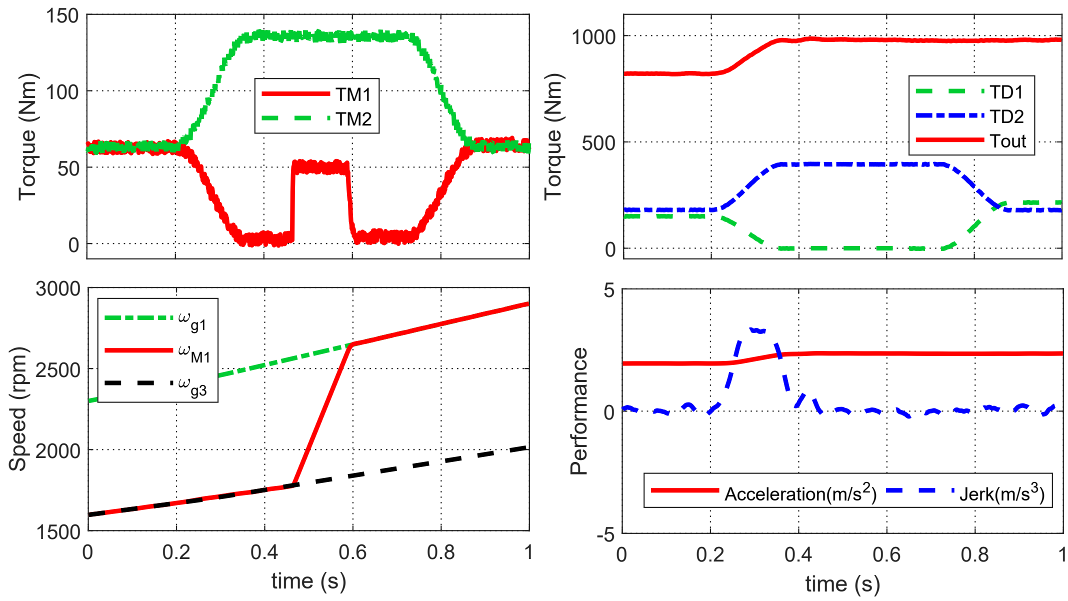

Fig. 6.15: Simulation results of power-on downshift when M1 changes gear from G3 to G1.

Fig. 6.14 shows simulated responses when the power-on upshift command of shifting the motor M1 from the gear G1 to G3 is applied at 0.2 s. In the test, M1 and M2 are initially connected to the gear G1 and G2 respectively. To complete gearshift, the clutch D1 should be disengaged first from G1 and then engaged with G3. When the gearshift begins, the torque of M1 gradually decreases following the predefined third-order polynomial while the torque of M2 rises to compensate for power reduction from M1. Generally, an electric motor has excellent short-time overload ability. Hence, it is not a problem for M2 to increase the power even over its rated value temporarily. Meanwhile, the output torque T_{out} smoothly decreases to its target value in this stage. After the clutch torque T_{D1} is regulated to around zero, the clutch D1 can be disengaged and then the speed of M1 is controlled to match the speed of gear G3. It should be noted that the motor torque is saturated to $\pm$ 50 Nm during the process of speed synchronization to reduce overshoot/undershoot. After that, D1 is engaged with G3 and the output torques of M1 and M2 are recovered. With the proposed gearshift control, the whole shifting process takes around 0.65 s with the maximum vehicle jerk less than 4 m/s^3. In addition to the upshift test, the results of the opposite downshift which shifts M1 from G3 to G1 while keeping M2 connected to G2 are demonstrated in Fig. 6.15. Similar to the upshift result, downshift can also be finished in a short time with small vehicle jerk and the induced driveline oscillation can be controlled to decay quickly. To more clearly validate the effectiveness of the proposed gearshift control, Fig. 6.16 compares responses of the following four cases when the same shift command as that in Fig. 6.14 is applied: 1) without both closed-loop clutch torque control and active damping control; 2) with only closed-loop clutch torque control; 3) with only active damping control; and 4) with both closed-loop torque control and active damping control. In all the presented results, the five stages of gearshift similar to that in Fig. 6.6 can be clearly identified. From Figs. 6.16a and 6.16c, it is seen that there would be high oscillations in the output torque T_{out} and large oscillations in the vehicle jerk after the disengagement/engagement of the clutch if the proposed closed-loop clutch torque control is not implemented. Additionally, if the active damping controller is disabled, as show in Figs. 6.16a and 6.16b, the induced driveline vibrations would last for a long time due to poor damping of the system. By comparison, when the clutch torque control and active damping control are both enabled, there is significantly less oscillations in the vehicle jerk and the induced vibrations decay quickly. These comparative results confirm that both closed-loop clutch torque control and active damping control are essential to achieve high quality gearshift.

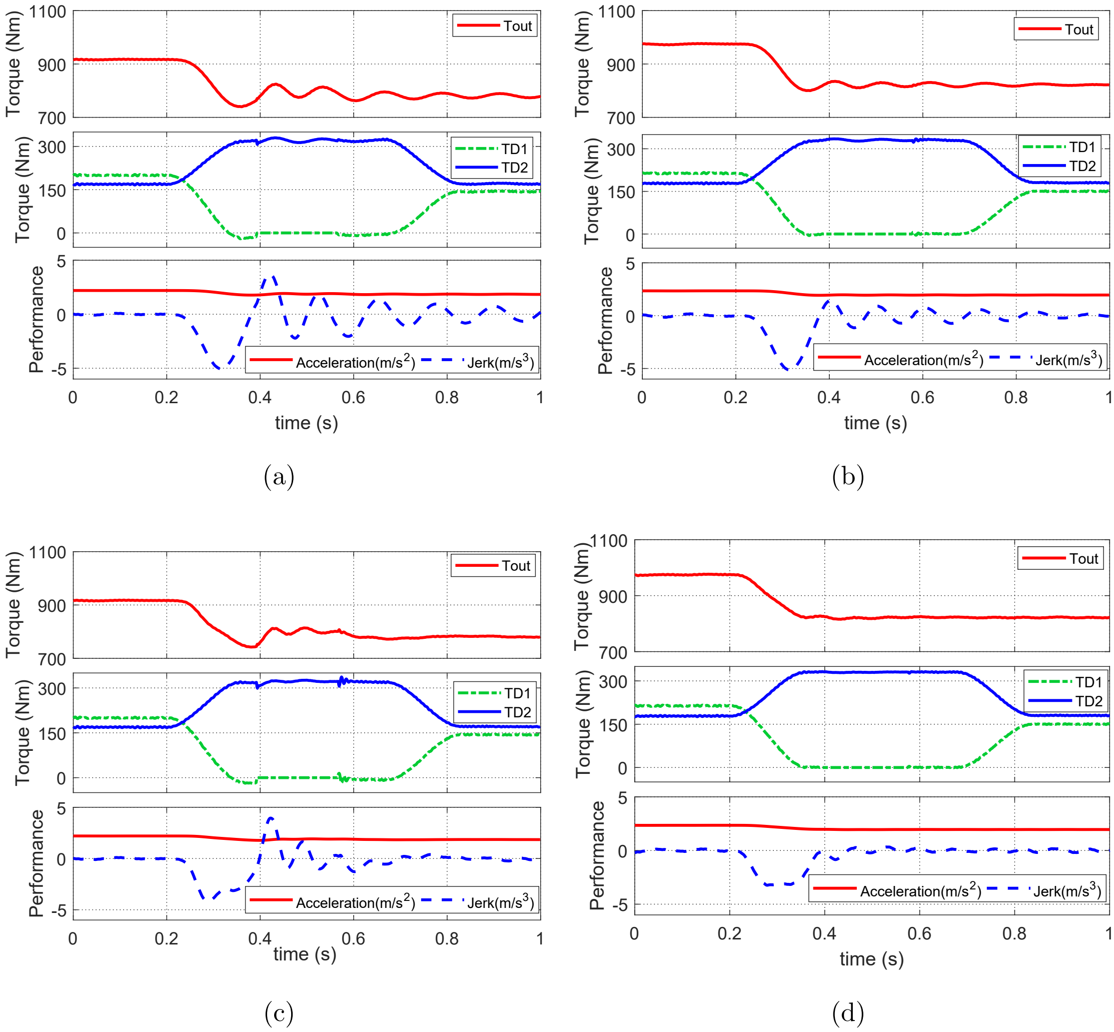

Fig. 6.16: Comparative results of power-on upshift. (a) without both closed-loop clutch torque control and active damping control; (b) with closed-loop clutch torque control but without active damping control; (c) with active damping control but without closed-loop clutch torque control; (d) with both closed-loop clutch torque control and active damping control.

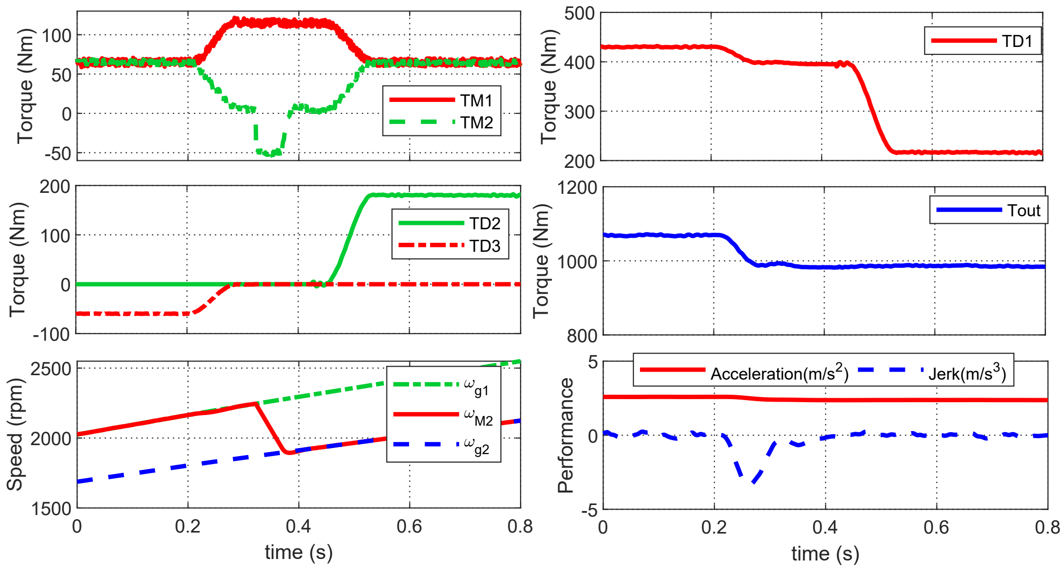

Fig. 6.17: Simulated responses when M1 and M2 shift from simultaneous working condition to the separate working condition.

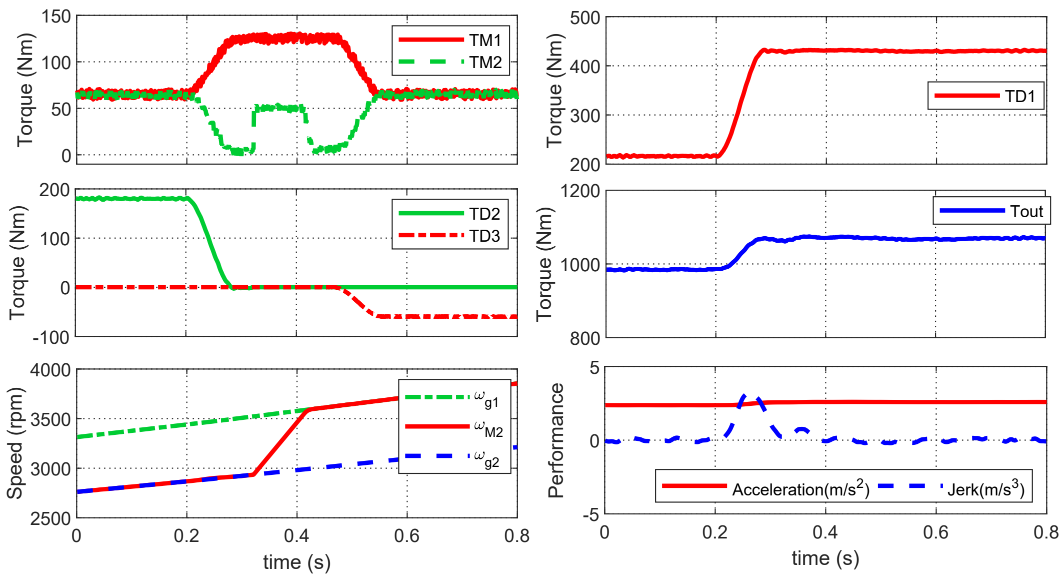

Fig. 6.18: Simulated responses when M1 and M2 shift from separate working condition to the simultaneous working condition.

Fig. 6.17 illustrates the case when M1 and M2 shift from the simultaneous working condition to the separate working condition. At the beginning, both M1 and M2 are connected to the gear G1. From 0.2 s, M2 begins to shift to G2. To complete gearshift, all three clutches D1, D2 and D3 are operated. At the first step, the output torque of M2 is reduced, meanwhile, the torque of M1 is increased so that the torque transmitted by D3 can be finally decreased to zero without causing torque hole in the output. Then, D3 is disengaged and the speed of M2 is regulated to track the speed of G2 at the second and third steps respectively. After the speed synchronization is completed, D2 is engaged to connect M2 with the gear G2 in the fourth step. At the last step, the torque of M2 is increased to re-balance the output power of M1 and M2. With the proposed gearshift control, the vehicle jerk during shifting process is small with very short duration of oscillations, indicating satisfactory shift smoothness and driving comfort are achieved. The opposite operation, i.e., shifting the M1 and M2 from the separate working condition to the simultaneous working condition is shown in Fig. 6.18. Similar to that in Fig. 6.17, smooth and fast gearshift is achieved by coordinated motor speed and torque control.

6.5 Summary

In this chapter, the closed-loop clutch torque control plus active vibration damping was proposed to achieve smooth and fast gearshift for a dual motor-based multi-speed transmission. As the torque transmitted by the dog clutch is not directly available to provide feedback, an extended discrete-time sliding mode torque observer was designed and verified by simulation and experimental tests. The results validated that the proposed torque observer can estimate the clutch torque accurately with satisfactory immunity against high-frequency harmonics. The whole control algorithm is simple and computationally light for integration into the motor drive controller, which is helpful to avoid complex compensation for the network communication delay. The test under different shifting conditions confirmed the effectiveness of the proposed method. The presented results showed that the closed-loop clutch torque control can help to reduce up-down fluctuations in the output torque during disengagement/engagement of the dog clutch, whilst active damping control can significantly reduce the duration of low-frequency torsional vibrations in the transmission.

Chapter 7

Conclusions and Future Works

7.1 Conclusions

Integrating the multi-speed transmission into the pure electric vehicle is regarded as a viable scheme to improve the powertrain efficiency and driveability. This thesis focus on the control of a dual input clutchless multi-speed transmission. Specifically, some high performance control methods were investigated for the control of motor drives and gear-shifting. The main work and contributions of this thesis can be summarized as follows:

- A novel feedback gain matrix was proposed for the adaptive full-order observer, which can ensure the estimated speed always converge to its actual value. Therefore, it can be applied to start a free-running motor without a speed sensor in practical application. For most speed-sensorless control schemes, the motor is assumed to be started from standstill. However, for applications with large shaft inertia, it is time consuming to wait a free-running motor to stop. Thus, it would be beneficial for a rotating motor to resume to normal operation after a power interruption. With the the proposed feedback gain matrix based-full order observer, it was verified by simulation and experimental tests that the induction motor can be smoothly and safely started at the free-running state.

- A parameter tuning method was proposed for the conventional discrete-time complex-vector current controller. Although the prior discrete-time complex-vector current controller shows satisfactory steady-state performance and can work stably under low frequency ratio, its dynamic response is not that fast. Therefore, a disturbance estimation based-digital predictive current controller was further proposed in the stationary reference frame for the IM drive. Simulation and experimental results confirm the superiority of the proposed digital predictive current controller in term of dynamic performance.

- A method of integrating the hybrid synchronous PWM schemes into the closed-loop current control was introduced. Considering the existing methods of smooth transition between different synchronous PWM schemes are either complex or not suitable for low frequency ratio, a novel method by compensating the phase angle of the voltage command is deduced in detail through analyzing the flux trajectories of different synchronous PWM schemes. In this way, the design of the current controller and PWM schemes are decoupled. Additionally, the varying sampling rate with online correction scheme was proposed to maintain symmetry of the output voltage pulses from the inverter. Experimental tests were carried out to validate the effectiveness of the proposed method.

- The PMSM model is modified so that the design principle of the discrete-time current controller for the nonsalient machine can be applied to the controller design for the salient PMSM. Based on the modified PMSM model, a discrete-time complex-vector current controller and a digital predictive current controller were developed in the synchronous reference frame. Simulation and experimental results confirmed their good performance even under low frequency ratio.

- To ensure satisfactory position estimation accuracy with low frequency ratio, a digital position estimator was developed for the PMSM drive. To reduce the computational burden, the back-EMF term related coefficient is simplified without sacrificing the precision. Due to the inherent filtering capacity, no additional filters or phase locked loop is required to suppress high-frequency harmonics. Simulation and experimental results validated that the proposed position estimator can accurately estimate the rotor position over a wide speed range under different load conditions.

- A detailed mathematical model of the DMMT was developed. It was shown that the powertrain damping at some specific frequencies is relatively small which would result in torsional vibrations when the motor torque varies. To suppress such vibrations, an active damping control scheme was proposed based on the feedback of ripple components of the clutch torque. It was shown that the proposed active damping control method could effectively suppress the shaft vibrations induced by the unknown disturbances and motor torque variation. Unlike some of the prior methods, the developed active damping control scheme does not require the wheel speed. Therefore, the complex compensation for the commutation delay is avoided. Additionally, only a proportional gain is required to tune in the proposed method. Hence, no effort is required to deal with issues of anti-windup and noise attenuation for the integral controller and derivative controller respectively, indicating that the proposed active damping control is easy to be debugged in practical implementation.

- Considering the measurement of the shaft torque is usually not feasible in practical application, a discrete-time sliding-mode torque observer (DSMTO) was designed to facilitate smooth and fast gearshift. In the existing literature, the minimum value of the sliding-mode gain is usually derived to guarantee the stability of the observer. However, it was shown in this thesis that the sliding-mode gain should also have a upper limit when considering the observer is implemented in a digital processor. Due to the inherent low-pass filtering effect, the proposed DSMTO is immune against measurement noise and there is no high-frequency chattering problem as that of the conventional sliding mode observer. Simulation and experimental tests were performed to validate the proposed DSMTO can accurately estimate the clutch torque at different speed and load conditions.

- A gearshift control method based on the closed-loop torque regulation was proposed for the DMMT. By coordinated motor torque and speed control, fast gearshift without power interruption was achieved. The shifting procedure, shifting duration, and shifting controller were developed to achieve fast and smooth gearshift. With the proposed shifting control scheme and the active damping controller, the vehicle jerk can be controlled within the satisfactory level and the induced driveline oscillations decay quickly. In the practical test on a modern digital signal processor, it only takes 8.79 μs to execute the whole control algorithm, indicating that the online computation burden of the proposed gearshift control is very light and suitable for implementation on an embedded microcontroller.

7.2 Future Work

The future tasks that can be further investigated based on the research work in this thesis are suggested as follows:

1. The proposed feedback gain matrix of the adaptive full order observer results in poor damping at high-speed operation. It would be better to modify the speed adaption law to guarantee the speed convergence when estimating the initial speed of a free-running IM.

2. The proposed digital predictive current controller presents zero steady-state tracking error with motor parameter mismatches. However, the dynamic performance especially during fast transient process would be deteriorated if motor parameters deviate significantly from the their values. Hence, a proper online parameter adaption scheme to make the controller more robust against parameter errors.

3. The synchronous PWM schemes employed in this thesis are space vector modulation based methods. The other modulation techniques such as selective harmonic elimination PWM (SHEPWM) and current harmonic minimum PWM (CHMPWM) can be applied and tested based on the proposed transition strategy.

4. With the synchronous PWM methods, the inverter can be operated at a relatively lower switching frequency, higher harmonics. Hence, the system level research should be carried out to determine the best modulation method among different PWM schemes to achieve globally minimized power loss.

5. As the modeled based position estimator for PMSM drives can not reliably work at very low speed, the signal-injection-based schemes should be employed during low speed operation. Moreover, the strategy that can start a free-running PMSM without a position sensor should be investigated.

6. The control of both IM and PMSM drives is investigated in this thesis. IM features simplicity, low cost but lower efficiency especially in low speed range. PMSM is superior in terms of power density and efficiency but its cost is relatively higher and some rare-earth material is required in PMSM. For the studied DMMT, it is possible to employ both IM and PMSM. However, further research is still required to determine the types of two motors based on the trade-off among efficiency, reliability, cost, power density, etc.

7. The proposed active damping controller relies on the estimated shaft torque. The damping controller can also be constructed based on the extraction of motor speed ripples, which would be more suitable for fixed-ratio transmission based electric vehicle because of the simplicity and robustness.

Appendix A

See Table A.1.

Table A.1 : Powertrain parameters.

Symbol	Description	Inertial (kg m^2)	Symbol	Damping (Nm-s/rad)
J_{M1}	Motor 1	0.07	$C_{M1,2}$	0.0015
J_{M2}	Motor 2	0.07	$C_{D1,2,3}$	80
J_{G1}	Gear 1	0.0008	C_1	80
J_{p1}	Pinion 1	0.0051	C_2	60
J_{G2}	Gear 2	0.0009	Symbol	Stiffness (Nm/rad)
J_{p2}	Pinion 2	0.0051	$k_{D1,2,3}$	2×10^5
J_{FD}	Final drive	0.005	k_1	2×10^5
J_{FD1}	Final drive 1	0.076	k_2	2.25×10^4
J_h	Half shaft + Wheel hub	0.68	-	-
J_v	Vehicle	124	-	-

Bibliography

[1] S. Kwak, U. C. Moon, and J. C. Park, "Predictive-control-based direct power control with an adaptive parameter identification technique for improved afe performance," *IEEE Trans. Power Electron.*, vol. 29, no. 11, pp. 6178–6187, Nov 2014.

[2] Z. Zhang, H. Xu, M. Xue, Z. Chen, T. Sun, R. Kennel, and C. M. Hackl, "Predictive control with novel virtual-flux estimation for back-to-back power converters," *IEEE Trans. Ind. Electron.*, vol. 62, no. 5, pp. 2823–2834, May 2015.

[3] Z. Zhu and D. Howe, "Electrical machines and drives for electric, hybrid, and fuel cell vehicles," *Proc. IEEE*, vol. 95, no. 4, pp. 746–765, 2007.

[4] S. J. Rind, Y. Ren, Y. Hu, J. Wang, and L. Jiang, "Configurations and control of traction motors for electric vehicles: A review," *Chinese Journal of Electrical Engineering*, vol. 3, no. 3, pp. 1–17, December 2017.

[5] H. Kim, M. Degner, J. Guerrero, F. Briz, and R. Lorenz, "Discrete-time current regulator design for ac machine drives," *IEEE Trans. Ind. Appl.*, vol. 46, no. 4, pp. 1425 –1435, july-aug. 2010.

[6] A. Altomare, A. Guagnano, F. Cupertino, and D. Naso, "Discrete-time control

of high-speed salient machines," *IEEE Trans. Ind. Appl.*, vol. 52, no. 1, pp. 293–301, Jan 2016.

[7] L. Eriksson and L. Nielsen, *Modeling and control of engines and drivelines.* John Wiley & Sons, 2014.

[8] M. Roozegar and J. Angeles, "The optimal gear-shifting for a multi-speed transmission system for electric vehicles," *Mech. Mach. Theory*, vol. 116, pp. 1 – 13, 2017.

[9] S. Fang, J. Song, H. Song, Y. Tai, F. Li, and T. S. Nguyen, "Design and control of a novel two-speed uninterrupted mechanical transmission for electric vehicles," *Mech. Syst. Sig. Process.*, vol. 75, pp. 473 – 493, 2016.

[10] P. Walker, B. Zhu, and N. Zhang, "Powertrain dynamics and control of a two speed dual clutch transmission for electric vehicles," *Mech. Syst. Sig. Process.*, vol. 85, pp. 1 – 15, 2017.

[11] B. Gao, Q. Liang, Y. Xiang, L. Guo, and H. Chen, "Gear ratio optimization and shift control of 2-speed i-amt in electric vehicle," *Mech. Syst. Sig. Process.*, vol. 50-51, pp. 615 – 631, 2015.

[12] C.-Y. Tseng and C.-H. Yu, "Advanced shifting control of synchronizer mechanisms for clutchless automatic manual transmission in an electric vehicle," *Mech. Mach. Theory*, vol. 84, pp. 37 – 56, 2015.

[13] J. Ruan, P. Walker, and N. Zhang, "A comparative study energy consumption

and costs of battery electric vehicle transmissions," *Appl. Energy*, vol. 165, pp. 119 – 134, 2016.

[14] X. Zhou, P. Walker, N. Zhang, B. Zhu, and J. Ruan, "Numerical and experimental investigation of drag torque in a two-speed dual clutch transmission," *Mech. Mach. Theory*, vol. 79, pp. 46 – 63, 2014.

[15] M. Roozegar and J. Angeles, "A two-phase control algorithm for gear-shifting in a novel multi-speed transmission for electric vehicles," *Mech. Syst. Sig. Process.*, vol. 104, pp. 145 – 154, 2018.

[16] Y. B. Bang and M. Yoon, "3-speed transmission using dual motors and one-way clutches," *IEEE/ASME Trans. Mechatronics*, vol. 21, no. 1, pp. 412–418, Feb 2016.

[17] J. Liang, H. Yang, J. Wu, N. Zhang, and P. D. Walker, "Shifting and power sharing control of a novel dual input clutchless transmission for electric vehicles," *Mech. Syst. Sig. Process.*, vol. 104, pp. 725 – 743, 2018.

[18] A. Sorniotti, T. Holdstock, M. Everitt, M. Fracchia, F. Viotto, C. Cavallino, and S. Bertolotto, "A novel clutchless multiple-speed transmission for electric axles," *International Journal of Powertrains*, vol. 2, no. 2-3, pp. 103–131, 2013.

[19] E. Dehghan-Azad, S. Gadoue, D. Atkinson, H. Slater, P. Barrass, and F. Blaabjerg, "Sensorless control of im for limp-home mode ev applications," *IEEE Trans. Power Electron.*, vol. 32, no. 9, pp. 7140–7150, Sep. 2017.

[20] G. Wu, X. Zhang, and Z. Dong, "Impacts of two-speed gearbox on electric

vehicle's fuel economy and performance," in *SAE Technical Paper*. SAE International, 04 2013.

[21] F. D. Nicola, A. Sorniotti, T. Holdstock, F. Viotto, and S. Bertolotto, "Optimization of a multiple-speed transmission for downsizing the motor of a fully electric vehicle," *SAE Int. J. Alt. Power.*, vol. 1, pp. 134–143, 04 2012.

[22] K. Zhao, Y. Liu, X. Huang, R. Yang, and J. Wei, "Uninterrupted shift transmission and its shift characteristics," *IEEE/ASME Transactions on Mechatronics*, vol. 19, no. 1, pp. 374–383, Feb 2014.

[23] M. S. R. Mousavi, A. Pakniyat, T. Wang, and B. Boulet, "Seamless dual brake transmission for electric vehicles: Design, control and experiment," *Mech. Mach. Theory*, vol. 94, pp. 96–118, 2015.

[24] M. A. Kluger and D. M. Long, "An overview of current automatic, manual and continuously variable transmission efficiencies and their projected future improvements," in *SAE Technical Paper*. SAE International, 03 1999.

[25] X. Zhou, P. D. Walker, and N. Zhang, "A numerical study of the impact of wet clutch drag torque on the performance of two-speed electric vehicles," *International Journal of Vehicle Performance*, vol. 2, no. 2, pp. 178–204, 2016.

[26] J. Greiner and M. Grumbach, "Automatic transmission systems beyond 2020 - challenges and competition," in *SAE Technical Paper*. SAE International, 04 2013.

[27] Q. Liang, N. Tang, B. Gao, and H. Chen, "The seamless gear shifting con-

trol for pure electric vehicle with 2-speed inverse-amt," {*IFAC*} *Proceedings Volumes*, vol. 46, no. 21, pp. 507 – 511, 2013, 7th {IFAC} Symposium on Advances in Automotive Control.

[28] I. Boldea, L. N. Tutelea, L. Parsa, and D. Dorrell, "Automotive electric propulsion systems with reduced or no permanent magnets: An overview," *IEEE Trans. Ind. Electron.*, vol. 61, no. 10, pp. 5696–5711, Oct 2014.

[29] P. D. Walker and N. Zhang, "Modelling of dual clutch transmission equipped powertrains for shift transient simulations," *Mech. Mach. Theory*, vol. 60, pp. 47–59, 2013.

[30] X. Tang, W. Yang, X. Hu, and D. Zhang, "A novel simplified model for torsional vibration analysis of a series-parallel hybrid electric vehicle," *Mech. Syst. Sig. Process.*, vol. 85, pp. 329 – 338, 2017.

[31] X. Zhu, F. Meng, H. Zhang, and Y. Cui, "Robust driveshaft torque observer design for stepped ratio transmission in electric vehicles," *Neurocomputing*, vol. 164, pp. 262 – 271, 2015.

[32] M. Pettersson and L. Nielsen, "Gear shifting by engine control," *IEEE Trans. Control Syst. Technol.*, vol. 8, no. 3, pp. 495–507, May 2000.

[33] A. Haj-Fraj and F. Pfeiffer, "Optimal control of gear shift operations in automatic transmissions," *J. Franklin Inst.*, vol. 338, no. 2-3, pp. 371 – 390, 2001, dynamics and Control of Structural and Mechanical Systems.

[34] Z. Yang, F. Shang, I. P. Brown, and M. Krishnamurthy, "Comparative study

of interior permanent magnet, induction, and switched reluctance motor drives for ev and hev applications," *IEEE Trans. Transport. Electrific.*, vol. 1, no. 3, pp. 245–254, Oct 2015.

[35] C. C. Chan, A. Bouscayrol, and K. Chen, "Electric, hybrid, and fuel-cell vehicles: Architectures and modeling," *IEEE Trans. Veh. Technol.*, vol. 59, no. 2, pp. 589–598, Feb 2010.

[36] V. T. Buyukdegirmenci, A. M. Bazzi, and P. T. Krein, "Evaluation of induction and permanent-magnet synchronous machines using drive-cycle energy and loss minimization in traction applications," *IEEE Trans. Ind. Appl.*, vol. 50, no. 1, pp. 395–403, Jan 2014.

[37] J. de Santiago, H. Bernhoff, B. Ekergård, S. Eriksson, S. Ferhatovic, R. Waters, and M. Leijon, "Electrical motor drivelines in commercial all-electric vehicles: A review," *IEEE Trans. Veh. Technol.*, vol. 61, no. 2, pp. 475–484, Feb 2012.

[38] M. Zeraoulia, M. E. H. Benbouzid, and D. Diallo, "Electric motor drive selection issues for hev propulsion systems: A comparative study," *IEEE Trans. Veh. Technol.*, vol. 55, no. 6, pp. 1756–1764, Nov 2006.

[39] M. Yildirim, M. Polat, and H. Kurum, "A survey on comparison of electric motor types and drives used for electric vehicles," in *Power Electronics and Motion Control Conference and Exposition (PEMC), 2014 16th International*, Sept 2014, pp. 218–223.

[40] K. Kiyota, H. Sugimoto, and A. Chiba, "Comparing electric motors: An anal-

ysis using four standard driving schedules," *IEEE Ind. Appl. Mag.*, vol. 20, no. 4, pp. 12–20, July 2014.

[41] J. O. Fiedler, K. A. Kasper, and R. W. D. Doncker, "Calculation of the acoustic noise spectrum of srm using modal superposition," *IEEE Trans. Ind. Electron.*, vol. 57, no. 9, pp. 2939–2945, Sept 2010.

[42] M. Takiguchi, H. Sugimoto, N. Kurihara, and A. Chiba, "Acoustic noise and vibration reduction of srm by elimination of third harmonic component in sum of radial forces," *IEEE Trans. Energy Convers.*, vol. 30, no. 3, pp. 883–891, Sept 2015.

[43] F. L. M. dos Santos, J. Anthonis, F. Naclerio, J. J. C. Gyselinck, H. V. der Auweraer, and L. C. S. Góes, "Multiphysics nvh modeling: Simulation of a switched reluctance motor for an electric vehicle," *IEEE Trans. Ind. Electron.*, vol. 61, no. 1, pp. 469–476, Jan 2014.

[44] A. T. Alexandridis, G. C. Konstantopoulos, and Q. C. Zhong, "Advanced integrated modeling and analysis for adjustable speed drives of induction motors operating with minimum losses," *IEEE Trans. Energy Convers.*, vol. 30, no. 3, pp. 1237–1246, Sept 2015.

[45] T. Sun and J. Wang, "Extension of virtual-signal-injection-based mtpa control for interior permanent-magnet synchronous machine drives into the field-weakening region," *IEEE Trans. Ind. Electron.*, vol. 62, no. 11, pp. 6809–6817, Nov 2015.

[46] W. Rippel, "Induction Versus DC Brushless Motors," https://www.tesla.com/blog/induction-versus-dc-brushless-motors, 2007.

[47] S. Sul, *Control of electric machine drive systems.* Wiley-IEEE Press, 2011, vol. 88.

[48] T. Sun, J. Wang, and X. Chen, "Maximum torque per ampere (mtpa) control for interior permanent magnet synchronous machine drives based on virtual signal injection," *IEEE Trans. Power Electron.*, vol. 30, no. 9, pp. 5036–5045, Sept 2015.

[49] Y. Wang, X. Wen, and F. Zhao, "A proposed control strategy of pmsm for deep field-weakening and square-wave mode," in *Electrical Machines and Systems (ICEMS), 2012 15th International Conference on*, Oct 2012, pp. 1–6.

[50] T. Finken and K. Hameyer, "Design of electric motors for hybrid-and electric-vehicle applications," in *Int. Conf. Electrical Machines Syst*, 2009.

[51] D. Casadei, F. Profumo, G. Serra, and A. Tani, "FOC and DTC: two viable schemes for induction motors torque control," *IEEE Trans. Power Electron.*, vol. 17, no. 5, pp. 779–787, Sep. 2002.

[52] Y. Zhang, J. Zhu, Z. Zhao, W. Xu, and D. Dorrell, "An improved direct torque control for three-level inverter-fed induction motor sensorless drive," *IEEE Trans. Power Electron.*, vol. 27, no. 3, pp. 1502 –1513, march 2012.

[53] X. Zhang and G. Foo, "A constant switching frequency based direct torque

control method for interior permanent magnet synchronous motor drives," *IEEE/ASME Trans. Mechatronics*, vol. PP, no. 99, pp. 1–1, 2015.

[54] Y. Zhang, H. Yang, and B. Xia, "Model predictive torque control of induction motor drives with reduced torque ripple," *IET Electr. Power Appl.*, vol. 9, no. 9, pp. 595–604, 2015.

[55] T. Geyer, G. Papafotiou, and M. Morari, "Model predictive direct torque control ;part i: Concept, algorithm, and analysis," *IEEE Trans. Ind. Electron.*, vol. 56, no. 6, pp. 1894 –1905, june 2009.

[56] K. Belda and D. Vosmik, "Explicit generalized predictive control of speed and position of pmsm drives," *IEEE Trans. Ind. Electron.*, vol. PP, no. 99, pp. 1–1, 2016.

[57] H.-T. Moon, H.-S. Kim, and M.-J. Youn, "A discrete-time predictive current control for pmsm," *IEEE Trans. Power Electron.*, vol. 18, no. 1, pp. 464–472, Jan 2003.

[58] H. Miranda, P. Cortes, J. Yuz, and J. Rodriguez, "Predictive torque control of induction machines based on state-space models," *IEEE Trans. Ind. Electron.*, vol. 56, no. 6, pp. 1916 –1924, june 2009.

[59] J. Rodriguez, R. Kennel, J. Espinoza, M. Trincado, C. Silva, and C. Rojas, "High-performance control strategies for electrical drives: An experimental assessment," *IEEE Trans. Ind. Electron.*, vol. 59, no. 2, pp. 812 –820, feb. 2012.

[60] Y. Zhang, B. Xia, and H. Yang, "Performance evaluation of an improved model predictive control with field oriented control as a benchmark," *IET Electr. Power Appl.*, vol. 11, no. 5, pp. 677–687, 2017.

[61] T. Geyer, "Computationally efficient model predictive direct torque control," *IEEE Trans. Power Electron.*, vol. 26, no. 10, pp. 2804 –2816, oct. 2011.

[62] F. Niu, B. Wang, A. S. Babel, K. Li, and E. G. Strangas, "Comparative evaluation of direct torque control strategies for permanent magnet synchronous machines," *IEEE Trans. Power Electron.*, vol. 31, no. 2, pp. 1408–1424, Feb 2016.

[63] B.-H. Bae and S.-K. Sul, "A compensation method for time delay of full-digital synchronous frame current regulator of PWM AC drives," *IEEE Trans. Ind. Appl.*, vol. 39, no. 3, pp. 802–810, 2003.

[64] J. Holtz, J. Quan, J. Pontt, J. Rodriguez, P. Newman, and H. Miranda, "Design of fast and robust current regulators for high-power drives based on complex state variables," *IEEE Trans. Ind. Appl.*, vol. 40, no. 5, pp. 1388 – 1397, sept.-oct. 2004.

[65] N. Hoffmann, F. W. Fuchs, M. P. Kazmierkowski, and D. Schröder, "Digital current control in a rotating reference frame - part i: System modeling and the discrete time-domain current controller with improved decoupling capabilities," *IEEE Trans. Power Electron.*, vol. 31, no. 7, pp. 5290–5305, July 2016.

[66] I. Boldea, *The induction machines design handbook.* CRC press, 2009.

[67] J.-S. Yim, S.-K. Sul, B.-H. Bae, N. Patel, and S. Hiti, "Modified current control schemes for high-performance permanent-magnet ac drives with low sampling to operating frequency ratio," *IEEE Trans. Ind. Appl.*, vol. 45, no. 2, pp. 763 –771, march-april 2009.

[68] Y. Zhang and J. Zhu, "Direct torque control of permanent magnet synchronous motor with reduced torque ripple and commutation frequency," *IEEE Trans. Power Electron.*, vol. 26, no. 1, pp. 235 –248, jan. 2011.

[69] ——, "A novel duty cycle control strategy to reduce both torque and flux ripples for dtc of permanent magnet synchronous motor drives with switching frequency reduction," *IEEE Trans. Power Electron.*, vol. 26, no. 10, pp. 3055 –3067, oct. 2011.

[70] A. A. Ahmed, B. K. Koh, and Y. I. Lee, "A comparison of finite control set and continuous control set model predictive control schemes for speed control of induction motors," *IEEE Trans. Ind. Informat.*, vol. 14, no. 4, pp. 1334–1346, April 2018.

[71] S. Mariethoz, A. Domahidi, and M. Morari, "High-bandwidth explicit model predictive control of electrical drives," *IEEE Trans. Ind. Appl.*, vol. 48, no. 6, pp. 1980–1992, 2012.

[72] S. A. Davari, D. A. Khaburi, F. Wang, and R. M. Kennel, "Using full order and reduced order observers for robust sensorless predictive torque control of

induction motors," *IEEE Trans. Power Electron.*, vol. 27, no. 7, pp. 3424–3433, July 2012.

[73] M. Habibullah and D. D. C. Lu, "A speed-sensorless fs-ptc of induction motors using extended kalman filters," *IEEE Trans. Ind. Electron.*, vol. 62, no. 11, pp. 6765–6778, Nov 2015.

[74] T. Geyer and D. Quevedo, "Multistep finite control set model predictive control for power electronics," *IEEE Trans. Power Electron.*, vol. 29, no. 12, pp. 6836–6846, Dec 2014.

[75] Y. Zhang and H. Yang, "Model-predictive flux control of induction motor drives with switching instant optimization," *IEEE Trans. Energy Convers.*, vol. 30, no. 3, pp. 1113–1122, Sept 2015.

[76] C. Rojas, J. Rodriguez, F. Villarroel, J. Espinoza, C. Silva, and M. Trincado, "Predictive torque and flux control without weighting factors," *IEEE Trans. Ind. Electron.*, vol. 60, no. 2, pp. 681 –690, feb. 2013.

[77] Y. Zhang and H. Yang, "Model predictive torque control of induction motor drives with optimal duty cycle control," *IEEE Trans. Power Electron.*, vol. 29, no. 12, pp. 6593–6603, 2014.

[78] X. Zhang and B. Hou, "Double vectors model predictive torque control without weighting factor based on voltage tracking error," *IEEE Trans. Power Electron.*, vol. 33, no. 3, pp. 2368–2380, March 2018.

[79] Y. Zhang and H. Yang, "Generalized two-vector-based model-predictive torque

control of induction motor drives," *IEEE Trans. Power Electron.*, vol. 30, no. 7, pp. 3818–3829, July 2015.

[80] S. Kwak and S. k. Mun, "Model predictive control methods to reduce common-mode voltage for three-phase voltage source inverters," *IEEE Trans. Power Electron.*, vol. 30, no. 9, pp. 5019–5035, Sept 2015.

[81] P. Karamanakos, P. Stolze, R. Kennel, S. Manias, and H. du Toit Mouton, "Variable switching point predictive torque control of induction machines," *IEEE Journal of Emerging and Selected Topics in Power Electronics*, vol. 2, no. 2, pp. 285–295, 2014.

[82] M. Norambuena, J. Rodriguez, Z. Zhang, F. Wang, C. Garcia, and R. Kennel, "A very simple strategy for high-quality performance of ac machines using model predictive control," *IEEE Trans. Power Electron.*, vol. 34, no. 1, pp. 794–800, Jan 2019.

[83] F. Wang, Z. Chen, P. Stolze, J. F. Stumper, J. Rodríguez, and R. Kennel, "Encoderless finite-state predictive torque control for induction machine with a compensated mras," *IEEE Trans. Ind. Informat.*, vol. 10, no. 2, pp. 1097–1106, May 2014.

[84] D. Marcetic, I. Krcmar, M. Gecic, and P. Matic, "Discrete rotor flux and speed estimators for high-speed shaft-sensorless im drives," *IEEE Trans. Ind. Electron.*, vol. 61, no. 6, pp. 3099–3108, June 2014.

[85] I. M. Alsofyani and N. R. N. Idris, "Simple flux regulation for improving

state estimation at very low and zero speed of a speed sensorless direct torque control of an induction motor," *IEEE Trans. Power Electron.*, vol. 31, no. 4, pp. 3027–3035, April 2016.

[86] W. Sun, Y. Yu, G. Wang, B. Li, and D. Xu, "Design method of adaptive full order observer with or without estimated flux error in speed estimation algorithm," *IEEE Trans. Power Electron.*, vol. PP, no. 99, pp. 1–1, 2015.

[87] Z. Xin, R. Zhao, F. Blaabjerg, L. Zhang, and P. C. Loh, "An improved flux observer for field-oriented control of induction motors based on dual second-order generalized integrator frequency-locked loop," *IEEE Journal of Emerging and Selected Topics in Power Electronics*, vol. 5, no. 1, pp. 513–525, March 2017.

[88] B. Wang, Y. Zhao, Y. Yu, G. Wang, D. Xu, and Z. Dong, "Speed-sensorless induction machine control in the field-weakening region using discrete speed-adaptive full-order observer," *IEEE Trans. Power Electron.*, vol. 31, no. 8, pp. 5759–5773, Aug 2016.

[89] B. Chen, W. Yao, F. Chen, and Z. Lu, "Parameter sensitivity in sensorless induction motor drives with the adaptive full-order observer," *IEEE Trans. Ind. Electron.*, vol. 62, no. 7, pp. 4307–4318, July 2015.

[90] Z. Zhang, R. Tang, B. Bai, and D. Xie, "Novel direct torque control based on space vector modulation with adaptive stator flux observer for induction motors," *IEEE Trans. Magn.*, vol. 46, no. 8, pp. 3133–3136, 2010.

[91] C. Lascu and G. Andreescu, "Sliding-mode observer and improved integrator

with dc-offset compensation for flux estimation in sensorless-controlled induction motors," *IEEE Trans. Ind. Electron.*, vol. 53, no. 3, pp. 785–794, 2006.

[92] K. Kondo, "Pmsm and im rotational sensorless technologies specialized for railway vehicles traction," in *2014 IEEE 5th International Symposium on Sensorless Control for Electrical Drives*, May 2014, pp. 1–7.

[93] L. Harnefors and M. Hinkkanen, "Stabilization methods for sensorless induction motor drives–a survey," *IEEE Journal of Emerging and Selected Topics in Power Electronics*, vol. 2, no. 2, pp. 132–142, June 2014.

[94] W. Sun, J. Gao, Y. Yu, G. Wang, and D. Xu, "Robustness improvement of speed estimation in speed-sensorless induction motor drives," *IEEE Trans. Ind. Appl.*, vol. 52, no. 3, pp. 2525–2536, May 2016.

[95] M. Zaky, "Stability analysis of speed and stator resistance estimators for sensorless induction motor drives," *IEEE Trans. Ind. Electron.*, vol. 59, no. 2, pp. 858 –870, feb. 2012.

[96] L. Harnefors and M. Hinkkanen, "Complete stability of reduced-order and full-order observers for sensorless im drives," *IEEE Trans. Ind. Electron.*, vol. 55, no. 3, pp. 1319–1329, March 2008.

[97] S. Suwankawin and S. Sangwongwanich, "Design strategy of an adaptive full-order observer for speed-sensorless induction-motor drives-tracking performance and stabilization," *IEEE Trans. Ind. Electron.*, vol. 53, no. 1, pp. 96–119, 2005.

[98] B. Chen, T. Wang, W. Yao, K. Lee, and Z. Lu, “Speed convergence rate-based feedback gains design of adaptive full-order observer in sensorless induction motor drives,” *IET Electr. Power Appl.*, vol. 8, no. 1, pp. 13–22, 2014.

[99] L.-J. Diao, D. nan Sun, K. Dong, L.-T. Zhao, and Z.-G. Liu, “Optimized design of discrete traction induction motor model at low-switching frequency,” *IEEE Trans. Power Electron.*, vol. 28, no. 10, pp. 4803–4810, 2013.

[100] H. Iura, K. Ide, T. Hanamoto, and Z. Chen, “An estimation method of rotational direction and speed for free-running ac machines without speed and voltage sensor,” *IEEE Trans. Ind. Appl.*, vol. 47, no. 1, pp. 153–160, Jan 2011.

[101] S. J. Jeong, Y. M. Park, and G. J. Han, “An estimation method of rotation speed for minimizing speed variation on restarting of induction motor,” in *Power Electronics and ECCE Asia (ICPE ECCE), 2011 IEEE 8th International Conference on*, May 2011, pp. 697–704.

[102] F. Giri, *AC electric motors control: Advanced design techniques and applications*. John Wiley & Sons, 2013.

[103] G. Yuan, X. Hou, C. Zheng, Z. Li, Y. Yin, and R. Liang, “Restarting with speed for ipmsm based on hybrid synchronized pwm control schemes for rail train traction system,” in *2017 20th International Conference on Electrical Machines and Systems (ICEMS)*, Aug 2017, pp. 1–5.

[104] G. Wang, Z. Li, G. Zhang, Y. Yu, and D. Xu, “Quadrature PLL-based high-order sliding-mode observer for IPMSM sensorless control with online mtpa

control strategy," *IEEE Trans. Energy Convers.*, vol. 28, no. 1, pp. 214–224, 2013.

[105] S.-Y. Jung, J. Hong, and K. Nam, "Current minimizing torque control of the ipmsm using ferrari's method," *IEEE Trans. Power Electron.*, vol. 28, no. 12, pp. 5603–5617, Dec 2013.

[106] Y. Zhao, W. Qiao, and L. Wu, "An adaptive quasi-sliding-mode rotor position observer-based sensorless control for interior permanent magnet synchronous machines," *IEEE Trans. Power Electron.*, vol. 28, no. 12, pp. 5618–5629, Dec 2013.

[107] M. Preindl and S. Bolognani, "Model predictive direct torque control with finite control set for pmsm drive systems, part 1: Maximum torque per ampere operation," *IEEE Trans. Ind. Informat.*, vol. 9, no. 4, pp. 1912–1921, 2013.

[108] ——, "Model predictive direct speed control with finite control set of pmsm drive systems," *IEEE Trans. Power Electron.*, vol. 28, no. 2, pp. 1007 –1015, feb. 2013.

[109] T. Türker, U. Buyukkeles, and A. F. Bakan, "A robust predictive current controller for pmsm drives," *IEEE Trans. Ind. Electron.*, vol. 63, no. 6, pp. 3906–3914, June 2016.

[110] M. Siami, D. A. Khaburi, A. Abbaszadeh, and J. Rodríguez, "Robustness improvement of predictive current control using prediction error correction

for permanent-magnet synchronous machines," *IEEE Trans. Ind. Electron.*, vol. 63, no. 6, pp. 3458–3466, June 2016.

[111] X. Zhang, B. Hou, and Y. Mei, "Deadbeat predictive current control of permanent-magnet synchronous motors with stator current and disturbance observer," *IEEE Trans. Power Electron.*, vol. 32, no. 5, pp. 3818–3834, May 2017.

[112] H. Yang, Y. Zhang, J. Liang, B. Xia, P. D. Walker, and N. Zhang, "Deadbeat control based on a multipurpose disturbance observer for permanent magnet synchronous motors," *IET Electr. Power Appl.*, vol. 12, no. 5, pp. 708–716, 2018.

[113] M. Preindl and E. Schaltz, "Sensorless model predictive direct current control using novel second-order pll observer for pmsm drive systems," *IEEE Trans. Ind. Electron.*, vol. 58, no. 9, pp. 4087–4095, Sept 2011.

[114] H. Yang, Y. Zhang, J. Liang, J. Gao, P. D. Walker, and N. Zhang, "Sliding-mode observer based voltage-sensorless model predictive power control of pwm rectifier under unbalanced grid conditions," *IEEE Trans. Ind. Electron.*, vol. 65, no. 7, pp. 5550–5560, July 2018.

[115] S. K. Tseng, T. H. Liu, and J. L. Chen, "Implementation of a sensorless interior permanent magnet synchronous drive based on current deviations of pulse-width modulation switching," *IET Electr. Power Appl.*, vol. 9, no. 2, pp. 95–106, 2015.

[116] S. y. Kuai, S. Zhao, F. p. Heng, and X. Cui, "Position sensorless technology of switched reluctance motor drives including mutual inductance," *IET Electr. Power Appl.*, vol. 11, no. 6, pp. 1085–1094, 2017.

[117] S. K. Kommuri, M. Defoort, H. R. Karimi, and K. C. Veluvolu, "A robust observer-based sensor fault-tolerant control for pmsm in electric vehicles," *IEEE Trans. Ind. Electron.*, vol. 63, no. 12, pp. 7671–7681, Dec 2016.

[118] Y.-D. Yoon, S.-K. Sul, S. Morimoto, and K. Ide, "High-bandwidth sensorless algorithm for ac machines based on square-wave-type voltage injection," *IEEE Trans. Ind. Appl.*, vol. 47, no. 3, pp. 1361–1370, 2011.

[119] O. A. Mohammed, A. A. Khan, A. M. El-Tallawy, A. Nejadpak, and M. J. Roberts, "A wavelet filtering scheme for noise and vibration reduction in high-frequency signal injection-based sensorless control of pmsm at low speed," *IEEE Trans. Energy Convers.*, vol. 27, no. 2, pp. 250–260, June 2012.

[120] D. Kim, Y. Kwon, S. Sul, J. Kim, and R. Yu, "Suppression of injection voltage disturbance for high frequency square-wave injection sensorless drive with regulation of induced high frequency current ripple," *IEEE Trans. Ind. Appl.*, vol. PP, no. 99, pp. 1–1, 2015.

[121] N.-C. Park and S.-H. Kim, "Simple sensorless algorithm for interior permanent magnet synchronous motors based on high-frequency voltage injection method," *IET Electr. Power Appl.*, vol. 8, no. 2, pp. 68–75, February 2014.

[122] J. Liu and Z. Zhu, "Sensorless control strategy by square-waveform high-

frequency pulsating signal injection into stationary reference frame," *IEEE Journal of Emerging and Selected Topics in Power Electronics*, vol. 2, no. 2, pp. 171–180, June 2014.

[123] G. Zhang, G. Wang, D. Xu, and N. Zhao, "Adaline-network-based pll for position sensorless interior permanent magnet synchronous motor drives," *IEEE Trans. Power Electron.*, vol. 31, no. 2, pp. 1450–1460, Feb 2016.

[124] O. Wallmark and L. Harnefors, "Sensorless control of salient pmsm drives in the transition region," *IEEE Trans. Ind. Electron.*, vol. 53, no. 4, pp. 1179–1187, June 2006.

[125] S. Po-ngam and S. Sangwongwanich, "Stability and dynamic performance improvement of adaptive full-order observers for sensorless pmsm drive," *IEEE Trans. Power Electron.*, vol. 27, no. 2, pp. 588–600, Feb 2012.

[126] V. Smidl and Z. Peroutka, "Advantages of square-root extended kalman filter for sensorless control of ac drives," *IEEE Trans. Ind. Electron.*, vol. 59, no. 11, pp. 4189–4196, Nov 2012.

[127] Z. Qiao, T. Shi, Y. Wang, Y. Yan, C. Xia, and X. He, "New sliding-mode observer for position sensorless control of permanent-magnet synchronous motor," *IEEE Trans. Ind. Electron.*, vol. 60, no. 2, pp. 710–719, Feb 2013.

[128] M. Comanescu, "Design and implementation of a highly robust sensorless sliding mode observer for the flux magnitude of the induction motor," *IEEE Trans. Energy Convers.*, vol. 31, no. 2, pp. 649–657, June 2016.

[129] H. Kim, J. Son, and J. Lee, “A high-speed sliding-mode observer for the sensorless speed control of a pmsm,” *IEEE Trans. Ind. Electron.*, vol. 58, no. 9, pp. 4069–4077, Sept 2011.

[130] G. Wang, H. Zhan, G. Zhang, X. Gui, and D. Xu, “Adaptive compensation method of position estimation harmonic error for emf-based observer in sensorless ipmsm drives,” *IEEE Trans. Power Electron.*, vol. 29, no. 6, pp. 3055–3064, June 2014.

[131] X. Zhang, L. Sun, K. Zhao, and L. Sun, “Nonlinear speed control for pmsm system using sliding-mode control and disturbance compensation techniques,” *IEEE Trans. Power Electron.*, vol. 28, no. 3, pp. 1358–1365, March 2013.

[132] D.-M. Park and K.-H. Kim, “Parameter-independent online compensation scheme for dead time and inverter nonlinearity in ipmsm drive through waveform analysis,” *IEEE Trans. Ind. Electron.*, vol. 61, no. 2, pp. 701–707, 2014.

[133] G. Wang, T. Li, G. Zhang, X. Gui, and D. Xu, “Position estimation error reduction using recursive-least-square adaptive filter for model-based sensorless interior permanent-magnet synchronous motor drives,” *IEEE Trans. Ind. Electron.*, vol. 61, no. 9, pp. 5115–5125, 2014.

[134] X. Song, J. Fang, B. Han, and S. Zheng, “Adaptive compensation method for high-speed surface pmsm sensorless drives of emf-based position estimation error,” *IEEE Trans. Power Electron.*, vol. 31, no. 2, pp. 1438–1449, Feb 2016.

[135] G. Wang, L. Ding, Z. Li, J. Xu, G. Zhang, H. Zhan, R. Ni, and D. Xu, “En-

hanced position observer using second-order generalized integrator for sensorless interior permanent magnet synchronous motor drives," *IEEE Trans. Energy Convers.*, vol. 29, no. 2, pp. 486–495, June 2014.

[136] H. Yang, Y. Zhang, and N. Zhang, "Two high performance position estimation schemes based on sliding-mode observer for sensorless spmsm drives," in *2016 IEEE 8th International Power Electronics and Motion Control Conference (IPEMC-ECCE Asia)*, May 2016, pp. 3663–3669.

[137] J. Holtz and N. Oikonomou, "Fast dynamic control of medium voltage drives operating at very low switching frequency—an overview," *IEEE Trans. Ind. Electron.*, vol. 55, no. 3, pp. 1005–1013, 2008.

[138] S. K. Sahoo and T. Bhattacharya, "Rotor flux-oriented control of induction motor with synchronized sinusoidal pwm for traction application," *IEEE Trans. Power Electron.*, vol. 31, no. 6, pp. 4429–4439, June 2016.

[139] G. Narayanan and V. T. Ranganathan, "Synchronised pwm strategies based on space vector approach. i. principles of waveform generation," *Proc. Inst. Elect. Eng.*, vol. 146, no. 3, pp. 267–275, May 1999.

[140] Y. Zhang, D. Xu, C. Yan, and S. Zou, "Hybrid pwm scheme for the grid inverter," *IEEE Journal of Emerging and Selected Topics in Power Electronics*, vol. 3, no. 4, pp. 1151–1159, Dec 2015.

[141] Y. Zhang, Z. Zhao, and J. Zhu, "A hybrid pwm applied to high-power three-

level inverter-fed induction-motor drives," *IEEE Trans. Ind. Electron.*, vol. 58, no. 8, pp. 3409–3420, Aug 2011.

[142] A. Mehrizi-Sani and S. Filizadeh, "An optimized space vector modulation sequence for improved harmonic performance," *IEEE Trans. Ind. Electron.*, vol. 56, no. 8, pp. 2894–2903, Aug 2009.

[143] V. S. S. P. K. Hari and G. Narayanan, "Space-vector-based hybrid pwm technique to reduce peak-to-peak torque ripple in induction motor drives," *IEEE Trans. Ind. Appl.*, vol. 52, no. 2, pp. 1489–1499, March 2016.

[144] G. Narayanan and V. T. Ranganathan, "Two novel synchronized bus-clamping pwm strategies based on space vector approach for high power drives," *IEEE Trans. Power Electron.*, vol. 17, no. 1, pp. 84–93, Jan 2002.

[145] ——, "Synchronised pwm strategies based on space vector approach. ii. performance assessment and application to v/f drives," *Proc. Inst. Elect. Eng.*, vol. 146, no. 3, pp. 276–281, May 1999.

[146] J. Holtz and B. Beyer, "Fast current trajectory tracking control based on synchronous optimal pulsewidth modulation," *IEEE Trans. Ind. Appl.*, vol. 31, no. 5, pp. 1110–1120, 1995.

[147] Y. Wang, X. Wen, X. Guo, F. Zhao, and W. Cong, "Vector control of induction motor based on selective harmonic elimination pwm in medium voltage high power propulsion system," in *Electric Information and Control Engineering (ICEICE), 2011 International Conference on*, April 2011, pp. 6351–6354.

[148] K. Yang, Z. Yuan, R. Yuan, W. Yu, J. Yuan, and J. Wang, "A groebner bases theory-based method for selective harmonic elimination," *IEEE Transactions on Power Electronics*, vol. 30, no. 12, pp. 6581–6592, Dec 2015.

[149] R. Rathore, J. Holtz, and T. Boller, "Generalized optimal pulsewidth modulation of multilevel inverters for low-switching-frequency control of medium-voltage high-power industrial AC drives," *IEEE Trans. Ind. Electron.*, vol. 60, no. 10, pp. 4215–4224, 2013.

[150] T. Geyer, N. Oikonomou, G. Papafotiou, and F. Kieferndorf, "Model predictive pulse pattern control," *IEEE Trans. Ind. Appl.*, vol. 48, no. 2, pp. 663–676, 2012.

[151] X. Zhu, H. Zhang, J. Xi, J. Wang, and Z. Fang, "Robust speed synchronization control for clutchless automated manual transmission systems in electric vehicles," *Proceedings of the Institution of Mechanical Engineers, Part D: Journal of Automobile Engineering*, vol. 229, no. 4, pp. 424–436, 2015.

[152] J. Zhang, Y. Li, C. Lv, J. Gou, and Y. Yuan, "Time-varying delays compensation algorithm for powertrain active damping of an electrified vehicle equipped with an axle motor during regenerative braking," *Mech. Syst. Sig. Process.*, vol. 87, pp. 45 – 63, 2017, signal Processing and Control challenges for Smart Vehicles.

[153] P. D. Walker and N. Zhang, "Active damping of transient vibration in dual clutch transmission equipped powertrains: A comparison of conventional and hybrid electric vehicles," *Mech. Mach. Theory*, vol. 77, pp. 1 – 12, 2014.

[154] X. Zhang, H. Liu, and C. yinqi, "Active damping of torsional vibration on the powertrain of power-split vehicle," *Energy Procedia*, vol. 105, pp. 2898 – 2903, 2017, 8th International Conference on Applied Energy, ICAE2016, 8-11 October 2016, Beijing, China.

[155] X. Shao, F. Naghdy, and H. Du, "Reliable fuzzy H_∞ control for active suspension of in-wheel motor driven electric vehicles with dynamic damping," *Mech. Syst. Sig. Process.*, vol. 87, pp. 365 – 383, 2017.

[156] J. J. Oh and S. B. Choi, "Real-time estimation of transmitted torque on each clutch for ground vehicles with dual clutch transmission," *IEEE/ASME Trans. Mechatronics*, vol. 20, no. 1, pp. 24–36, Feb 2015.

[157] S. Rhode, S. Hong, J. K. Hedrick, and F. Gauterin, "Vehicle tractive force prediction with robust and windup-stable kalman filters," *Control Eng. Pract.*, vol. 46, pp. 37 – 50, 2016.

[158] J. Wu, P. D. Walker, J. Ruan, and N. Zhang, "Target torque estimation for gearshift in dual clutch transmission with uncertain parameters," *Appl. Math. Modell.*, vol. 51, no. Supplement C, pp. 1 – 20, 2017.

[159] J. Holtz, "The representation of ac machine dynamics by complex signal flow graphs," *IEEE Trans. Ind. Electron.*, vol. 42, no. 3, pp. 263 –271, jun 1995.

[160] Y. Zhao, Z. Zhang, W. Qiao, and L. Wu, "An extended flux model-based rotor position estimator for sensorless control of salient-pole permanent-magnet

synchronous machines," *IEEE Trans. Power Electron.*, vol. 30, no. 8, pp. 4412–4422, Aug 2015.

[161] Y. Inoue, Y. Kawaguchi, S. Morimoto, and M. Sanada, "Performance improvement of sensorless ipmsm drives in a low-speed region using online parameter identification," *IEEE Trans. Ind. Appl.*, vol. 47, no. 2, pp. 798–804, March 2011.

[162] K. Bovee and G. Rizzoni, "Model-based torque shaping for smooth acceleration response in hybrid electric vehicles," *IFAC-PapersOnLine*, vol. 49, no. 11, pp. 525 – 532, 2016.

[163] J. C. Alacoque, *DIRECT EIGEN CONTROL FOR INDUCTION MACHINES AND SYNCHRONOUS MOTORS.* Wiley-IEEE Press, 2015, vol. 88.

[164] H. Yang, Y. Zhang, G. Yuan, P. D. Walker, and N. Zhang, "Hybrid synchronized pwm schemes for closed-loop current control of high-power motor drives," *IEEE Trans. Ind. Electron.*, vol. 64, no. 9, pp. 6920–6929, Sept 2017.

[165] H. Yang, Y. Zhang, P. D. Walker, N. Zhang, and B. Xia, "A method to start rotating induction motor based on speed sensorless model-predictive control," *IEEE Trans. Energy Convers.*, vol. 32, no. 1, pp. 359–368, March 2017.

[166] H. Yang, Y. Zhang, J. Liang, N. Zhang, and P. Walker, "Robust digital current control based on adaptive disturbance estimation for pmsm drives with low

pulse ratio," in *2018 21st International Conference on Electrical Machines and Systems (ICEMS)*, Oct 2018, pp. 1252–1257.

[167] H. Yang, Y. Zhang, P. D. Walker, J. Liang, N. Zhang, and B. Xia, "Speed sensorless model predictive current control with ability to start a free running induction motor," *IET Electr. Power Appl.*, vol. 11, no. 5, pp. 893–901, 2017.

[168] Y. Wang, X. Wen, X. Guo, F. Zhao, and W.Cong, "The smooth transition research of different pwm modulations for vector control of induction motor in medium voltage high power," in *Electrical Machines and Systems (ICEMS), 2011 International Conference on*, Aug 2011, pp. 1–5.

[169] S. C. Chapra and R. P. Canale, *Numerical methods for engineers*, 6th ed. McGraw-Hill Higher Education, 2010.

[170] J. Maes and J. Melkebeek, "Speed-sensorless direct torque control of induction motors using an adaptive flux observer," *IEEE Trans. Ind. Appl.*, vol. 36, no. 3, pp. 778–785, 2000.

[171] P. Cortes, J. Rodriguez, C. Silva, and A. Flores, "Delay compensation in model predictive current control of a three-phase inverter," *IEEE Trans. Ind. Electron.*, vol. 59, no. 2, pp. 1323–1325, 2012.

[172] K.-K. Huh and R. Lorenz, "Discrete-time domain modeling and design for ac machine current regulation," in *Industry Applications Conference, 2007. 42nd IAS Annual Meeting. Conference Record of the 2007 IEEE*, sept. 2007, pp. 2066 –2073.

[173] A. Yepes, A. Vidal, F. Freijedo, J. Malvar, O. Lopez, and J. Doval-Gandoy, “A simple tuning method aimed at optimal settling time and overshoot for synchronous pi current control in electric machines,” in *Energy Conversion Congress and Exposition (ECCE), 2013 IEEE*, 2013, pp. 1465–1472.

[174] Y. Zhang, B. Xia, Y. Bai, and H. Yang, “A novel design method of ac motor current regulator in discrete-time domain,” *Journal of Electrical Engineering*, vol. 12, no. 3, pp. 24–32, 2017, (in Chinese).

[175] S. C. Yang and G. R. Chen, “High speed position sensorless drive of permanent magnet machine using discrete-time emf estimation,” *IEEE Trans. Ind. Electron.*, vol. 64, no. 6, pp. 4444 – 4453, 2017.

[176] G. Narayanan and V. T. Ranganathan, “Extension of operation of space vector pwm strategies with low switching frequencies using different overmodulation algorithms,” *IEEE Trans. Power Electron.*, vol. 17, no. 5, pp. 788–798, Sep 2002.

[177] J. Holtz and N. Oikonomou, “Synchronous optimal pulsewidth modulation and stator flux trajectory control for medium-voltage drives,” *IEEE Trans. Ind. Appl.*, vol. 43, no. 2, pp. 600–608, 2007.

[178] H. Kubota and K. Matsuse, “Speed sensorless field-oriented control of induction motor with rotor resistance adaptation,” *IEEE Trans. Ind. Appl.*, vol. 30, no. 5, pp. 1219–1224, Sep 1994.

[179] Y. Wang, S. Tobayashi, and R. D. Lorenz, “A low-switching-frequency flux

observer and torque model of deadbeat direct torque and flux control on induction machine drives," *IEEE Trans. Ind. Appl.*, vol. 51, no. 3, pp. 2255–2267, May 2015.

[180] W. Wang, J. Zhang, and M. Cheng, "A dual-level hysteresis current control for one five-leg vsi to control two pmsms," *IEEE Trans. Power Electron.*, vol. 32, no. 1, pp. 804–814, Jan 2017.

[181] J. Lara, J. Xu, and A. Chandra, "A novel algorithm based on polynomial approximations for an efficient error compensation of magnetic analog encoders in pmsms for evs," *IEEE Trans. Ind. Electron.*, vol. 63, no. 6, pp. 3377–3388, June 2016.

[182] S. C. Yang and G. R. Chen, "High-speed position-sensorless drive of permanent-magnet machine using discrete-time emf estimation," *IEEE Trans. Ind. Electron.*, vol. 64, no. 6, pp. 4444–4453, June 2017.

[183] Y. seok Jeong and S.-K. Sul, "Analysis and design of a decoupling current controller for ac machines: a unified transfer-matrix approach," in *Fourtieth IAS Annual Meeting. Conference Record of the 2005 Industry Applications Conference, 2005.*, vol. 1, Oct 2005, pp. 751–758 Vol. 1.

[184] T. Bernardes, V. Foletto Montagner, H. Grundling, and H. Pinheiro, "Discrete-time sliding mode observer for sensorless vector control of permanent magnet synchronous machine," *IEEE Trans. Ind. Electron.*, vol. 61, no. 4, pp. 1679–1691, April 2014.

[185] Y.-S. Han, J.-S. Choi, and Y.-S. Kim, “Sensorless pmsm drive with a sliding mode control based adaptive speed and stator resistance estimator,” *IEEE Trans. Magn.*, vol. 36, no. 5, pp. 3588–3591, Sep 2000.

[186] G. Zhang, G. Wang, D. G. Xu, and Y. Yu, “Discrete-time low-frequency-ratio synchronous-frame full-order observer for position sensorless ipmsm drives,” *IEEE Journal of Emerging and Selected Topics in Power Electronics*, vol. 5, no. 2, pp. 870–879, Jun. 2017.

[187] M. S. Kumar and S. T. Revankar, “Development scheme and key technology of an electric vehicle: An overview,” *Renewable Sustainable Energy Rev.*, vol. 70, pp. 1266 – 1285, 2017.

[188] Z. Lei, D. Sun, Y. Liu, D. Qin, Y. Zhang, Y. Yang, and L. Chen, “Analysis and coordinated control of mode transition and shifting for a full hybrid electric vehicle based on dual clutch transmissions,” *Mech. Mach. Theory*, vol. 114, pp. 125 – 140, 2017.

[189] W. Mo, P. D. Walker, Y. Fang, J. Wu, J. Ruan, and N. Zhang, “A novel shift control concept for multi-speed electric vehicles,” *Mech. Syst. Sig. Process.*, vol. 112, pp. 171 – 193, 2018.

[190] K. Chau, *Electric vehicle machines and drives: design, analysis and application.* John Wiley & Sons, 2015.

[191] H. Kawamura, K. Ito, T. Karikomi, and T. Kume, “Highly-responsive acceler-

ation control for the nissan leaf electric vehicle," SAE Technical Paper, Tech. Rep., 2011.

[192] F. U. Syed, M. L. Kuang, and H. Ying, "Active damping wheel-torque control system to reduce driveline oscillations in a power-split hybrid electric vehicle," *IEEE Trans. Veh. Technol.*, vol. 58, no. 9, pp. 4769–4785, Nov 2009.

[193] T. Karikomi, K. Itou, T. Okubo, and S. Fujimoto, "Development of the shaking vibration control for electric vehicles," in *2006 SICE-ICASE International Joint Conference*, Oct 2006, pp. 2434–2439.

[194] C. Wang, M. Yang, W. Zheng, J. Long, and D. Xu, "Vibration suppression with shaft torque limitation using explicit mpc-pi switching control in elastic drive systems," *IEEE Trans. Ind. Electron.*, vol. 62, no. 11, pp. 6855–6867, Nov 2015.

[195] X. Wang, L. Li, and C. Yang, "Hierarchical control of dry clutch for engine-start process in a parallel hybrid electric vehicle," *IEEE Trans. Transport. Electrific.*, vol. 2, no. 2, pp. 231–243, June 2016.

[196] R. Masmoudi and J. Hedrick, "Estimation of vehicle shaft torque using nonlinear observers," *J Dyn Syst Meas Contr*, vol. 114, no. 3, pp. 394–400, 1992.

[197] W. Gao, Y. Wang, and A. Homaifa, "Discrete-time variable structure control systems," *IEEE Trans. Ind. Electron.*, vol. 42, no. 2, pp. 117–122, Apr 1995.

[198] K. Ogata, *Discrete-time control systems.* Prentice Hall Englewood Cliffs, NJ, 1995, vol. 2.